Free Carrier Absorption and Effective Masses in Zinc Antimonide-Cadmium Antimonide Alloys

by

ALAN WALFRED CARLSON

CENTER FOR SPACE RESEARCH

and

ENERGY CONVERSION AND SEMICONDUCTOR LABORATORY

DEPARTMENT OF ELECTRICAL ENGINEERING

MASSACHUSETTS INSTITUTE OF TECHNOLOGY

CAMBRIDGE 39, MASSACHUSETTS

SCIENTIFIC REPORT NO. 3

on

CONTRACT: NASA Grant NsG 496 (part)

M.I.T. Task: 76153

May, 1967

FREE CARRIER ABSORPTION AND EFFECTIVE MASSES IN ZINC ANTIMONIDE-CADMIUM ANTIMONIDE ALLOYS

by

ALAN WALFRED CARLSON

CENTER FOR SPACE RESEARCH

and

ENERGY CONVERSION AND SEMICONDUCTOR LABORATORY

Department of Electrical Engineering
MASSACHUSETTS INSTITUTE OF TECHNOLOGY
Cambridge 39, Massachusetts

SCIENTIFIC REPORT NO. 3

on

CONTRACT: NASA Grant NsG 496 (part)
M.I.T. Task: 76153

May, 1967

FREE CARRIER ABSORPTION AND EFFECTIVE MASSES IN ZINC ANTIMONIDE-CADMIUM ANTIMONIDE ALLOYS

by

ALAN WALFRED CARLSON

This report is identical to a thesis submitted to the Department of Electrical Engineering, M.I.T., May, 1967, in partial fulfillment of the requirements for the degree of Doctor of Philosophy.

ABSTRACT

Electrical and optical measurements have been made on p-type, single crystal ZnSb, CdSb, and $Cd_xZn_{1-x}Sb$ alloys. For each crystal axis of orthorhombic ZnSb and CdSb, the refractive index, optical absorption, electrical conductivity, and Hall coefficient have been measured. Free carrier absorption has been identified as the dominant absorption mechanism in the wavelength range of 7 to 15 μ. The high frequency conductivity, observed as free carrier absorption, and the low frequency conductivity have been used to uncouple the effective masses and relaxation times. For ZnSb and CdSb the effective mass tensor and relaxation time tensor are calculated from the experimental data. An anisotropic relaxation time is observed for both materials. The optical absorption, electrical conductivity, and Hall coefficient have been measured for the a and b axes of eight alloy samples. Free carrier absorption was observed in the alloys and used with the electrical data to obtain the effective masses, m_a^* and m_b^*, across the entire alloy composition range. The relaxation time parameters for the a and b axes are also obtained across the composition range.

ACKNOWLEDGEMENT

The author is deeply grateful to Professor Arthur C. Smith for his supervision and guidance of this research. He is also indebted to the thesis readers, Professors Richard B. Adler and Robert H. Rediker, for their technical advice. He would also like to thank Dr. Paul Shaver and Dr. John Blair for their help in initiating this work.

Special thanks is due Mr. William Brennan for his many hours of time spent on sample preparation. The author would also like to thank Mr. Robert Mills and Mr. William Pitkin for their assistance in the x-ray work and crystal growth, respectively. The author is grateful for the assistance of Mr. Peter Kelleher and the Materials Science Center Machine Shop in fabricating the equipment used.

Thanks are due also to the members of the Energy Conversion and Semiconductor Laboratory for the many helpful discussions which occurred in the course of this work.

For the production of the final manuscript, thanks are due to Mrs. Rita Albee for her typing skills and to Mr. John Mara for his drafting skills.

The author would like to thank his wife Sandra for her unfailing encouragement and support.

Finally, the author would like to thank the National

Aeronautics and Space Administration for its financial support. This research was carried out under contract NASA Grant NsG 496 (part). The author held a NASA Traineeship for part of the time in which this research was done.

TABLE OF CONTENTS

List of Figures

List of Tables

CHAPTER I. INTRODUCTION

The objective of this work is to study the valence band effective masses and relaxation times in ZnSb, CdSb, and $Cd_xZn_{1-x}Sb$. There is no determination of these parameters in the present literature. The method used to obtain the effective masses and relaxation times of these orthorhombic semiconductors is as follows. The low frequency and high frequency electrical conductivity tensors are measured. The high frequency electrical conductivity is observed as free carrier absorption. Then this data and Hall coefficient data are used to uncouple the relaxation time and effective mass parameters and to obtain them individually. In this way, the various anisotropies in the effective mass and relaxation time can be observed directly. In the following paragraphs a review of the literature on ZnSb, CdSb, and $Cd_xZn_{1-x}Sb$ is given.

K. Almin[1] was the first to determine the crystal structure of ZnSb and CdSb. Both are orthorhombic and have the space group D_{2h}^{15}, in the Schoenflies notation. There are 16 atoms per unit cell for each material. For ZnSb the unit cell dimensions are a = 6.218 A^o, b = 7.741 A^o, and c = 8.115 A^o. For CdSb the unit cell dimensions are a = 6.471 A^o, b = 8.253 A^o, and c = 8.526 A^o.

The phase diagrams of the Zn-Sb system and the Cd-Sb system are given by M. Hansen.[2] V. Frei and B. Velicky[3] and V. Khartsiev[4] have discussed the energy band symmetry in k-space from group theoretical considerations.

For ZnSb, R. Eisner, et al,[5] have developed a way to grow large ZnSb single crystals. M. Zavetova[6] has studied the absorption edge and determined that ZnSb has an indirect gap of 0.50 ev. at 300°K. H. Komiya, et al,[7] have studied the optical absorption and the refractive indices as a function of wavelength. M. Kot and I. Kretsu[8] have studied the transport properties of ZnSb on oriented single crystal samples but without identifying the axes. P. Shaver and J. Blair[9] have measured the electrical conductivity, Hall coefficient, magnetoresistance, thermoelectric power, and thermal conductivity. They used single crystal samples and identified the measured axes.

For CdSb, M. Zavetova[10] has determined the refractive indices at the absorption edge. J. Tauc and A. Abraham[11] have studied the reflection spectra for the three independent directions of polarization and for photon energies above the absorbtion edge. For this spectral region they have computed the real and imaginary parts of the dielectric constant. F. Ermanis and E. Miller[12] have determined that CdSb has an indirect energy gap of 0.45 ev. at 300°K.

I. K. Andronik, et al,[13] have studied the transport properties of CdSb at low temperatures to determine the energy levels of impurities. L. Stourac[14] has studied the dependence of the Hall constant of p-type CdSb on magnetic field. V. Frei, et al,[15] have studied the magnetoresistance of p-type CdSb. T. Kawasaki and T. Tanaka[16] have studied the anisotropic electrical conductivity and Hall effect in CdSb. I. Andronik and M. Kot have studied the transport properties of CdSb. In an early paper,[17] they used single crystal oriented samples but did not identify the axes. In a later paper,[18] they used single crystal samples and did identify the axes along which measurements were made.

ZnSb and CdSb form a substitutional alloy $Cd_xZn_{1-x}Sb$ over the entire composition range. K. Toman[19] has determined the lattice parameters versus composition for the alloy system. M. Miksovsky, et al,[20] have determined the equilibrium diagram for the ZnSb-CdSb pseudobinary system. Yu. Keloglu and A. Fedorko[21] have also determined the diagram of the ZnSb-CdSb pseudobinary system and done additional thermal and x-ray analysis. E. Justi, et al,[22] have measured the transport properties of polycrystalline samples. Ya. Ugai and E. Averbakh[23] have measured the transport properties of single crystal samples as a function of temperature. However, they did not identify the axes along which any of the measurements were made.

L. Stourac, et al,[24] have measured the anisotropic absorption edge and transport properties of single crystal alloy samples of two compositions.

The above mentioned work constitutes almost all the work on single crystal ZnSb, CdSb, and $Cd_xZn_{1-x}Sb$ reported in the literature. For CdSb there has been additional work done on the effect of various dopants and on the anisotropic thermal conductivity. This work was not cited above since it is of little relevance to the work reported here.

There is one piece of work not cited above which should be discussed. M. Stevenson[25] has observed cyclotron resonance in both ZnSb and CdSb. The material used was p-type but the resonance was observed only when the sample was illuminated. With a filter which excluded photons with energy greater than 0.2 ev. the resonance was not seen. This radiation is sufficient to excite holes from the known acceptor levels in the material. Thus it is quite certain that Stevenson was observing an electron resonance rather than a hole resonance. He was not able to determine the sign of the resonance with circularly polarized radiation. Stevenson reasoned that he did not see the hole resonance because either the hole relaxation time was too short or the resonance was beyond the frequency range of his equipment.

Thus the hole effective masses are unknown for both ZnSb

and CdSb. Although several authors claim to have determined the effective masses from transport properties, they have really determined the relaxation time to effective mass ratios. The effective masses cannot be uncoupled from the relaxation time by low frequency transport measurements alone. The goal of this work became to determine the valence band effective masses.

Initially, it was proposed to use the Faraday effect to determine the effective masses. However, subsequent calculations, discussed in Appendix I, showed this to be impractical. The orthorhombic symmetry of these materials makes their properties very anisotropic. The anisotropy of the dielectric constant overwhelms the effect of a dc magnetic field on the propagation of electromagnetic radiation in the crystal. Instead of producing a sizable Faraday rotation such as occurs in cubic semiconductors, the magnetic field will produce only an undetectable rotation in ZnSb or CdSb.

It was decided to use a technique which would utilize the low symmetry to determine the effective masses rather than use more conventional techniques, suited to cubic materials. The low symmetry often prevents the use of more conventional techniques. The scheme that was used to determine the effective masses will be discussed here. Essentially, the electrical conductivity and its high frequency analog, free carrier

absorption, are used to uncouple the relaxation time from the effective masses.

In the crystal axis coordinate system the electrical conductivity is a diagonal tensor for ZnSb, CdSb, and their alloys of the form

$$\sigma = \begin{pmatrix} \sigma_a & 0 & 0 \\ 0 & \sigma_b & 0 \\ 0 & 0 & \sigma_c \end{pmatrix} . \qquad (1.1)$$

From magnetoresistance measurements on ZnSb[9] and CdSb,[15] the axes of the ellipsoidal constant energy surfaces of the valence band are known to lie along the crystal axes directions in k-space. Then from conventional transport theory, the individual components of the electrical conductivity for p-type material may be written as

$$\sigma_i = \frac{pe^2 < \tau_i >}{m_i^*} . \qquad (1.2)$$

In Eq. (1.2) p is the hole concentration, e is the electronic charge, $< \tau_i >$ is a suitable average of the relaxation time for the i^{th} direction, and m_i^* is the effective mass for the i^{th} direction.

If it can be observed and measured, the free carrier absorption, discussed in Appendix 2, will be of the form

$$\alpha = \begin{pmatrix} \alpha_a & 0 & 0 \\ 0 & \alpha_b & 0 \\ 0 & 0 & \alpha_c \end{pmatrix} \tag{1.3}$$

in the crystal axes coordinate system. Each component α_i of α will be given by

$$\alpha_i = \frac{pe^2\lambda^2}{(2\pi)^2 n_i c^3 \varepsilon_o m_i^*} \left\langle \frac{1}{\tau_i} \right\rangle \quad . \tag{1.4}$$

In Eq. (1.4) λ is the wavelength of the radiation in free space, c is the speed of light in free space, and ε_o is the electrical permittivity of free space. Also n_i is the i^{th} component of the refractive index tensor and $< 1/\tau_i >$ is a suitable average of the reciprocal relaxation time for the i^{th} direction.

From the literature the Hall coefficient and thermoelectric power of ZnSb and CdSb are observed to be isotropic for p-type material in the extrinsic region.[9,18] This determines the most general form of the relaxation time tensor to be

$$\tau = \begin{pmatrix} A_a & 0 & 0 \\ 0 & A_b & 0 \\ 0 & 0 & A_c \end{pmatrix} E^{-s}. \tag{1.5}$$

In Eq. (1.5), the A_i's are the relaxation time coefficients,

E is the hole energy, and s is a constant which determines the energy dependence of the relaxation time. The parameter s can be determined from data on the conductivity versus temperature in the extrinsic range.

The scheme used for determining the effective masses is as follows. The absorption coefficient for radiation polarized along each axis was measured and checked for the presence of free carrier absorption. The electrical conductivity and Hall coefficient was measured for the same material. The data from free carrier absorption, electrical conductivity, and Hall effect was then used with Eqs. (1.2), (1.4) and (1.5) to determine the effective masses, the m_i^*'s, and the relaxation time coefficients, the A_i's.

Chapter II describes the procedures used to grow ZnSb, CdSb, and $Cd_xZn_{1-x}Sb$. All single crystal material was grown in a horizontal zone furnace. The preparation of the optical and electrical samples is also described in this chapter.

Chapter III describes the measurement techniques used in this work. The refractive indices, needed to determine absorption data from transmission data, were obtained by the use of two interference phenomena. The optical absorption coefficients were obtained from experimental data of transmission versus wavelength. The spectral region of 3 to 15 microns in wavelength was utilized. The electrical measurements were made at

a frequency of 25 to 30 cps to avoid thermoelectric effects.

In Chapter IV, the experimental data for ZnSb and CdSb is presented. The resulting hole effective masses are for ZnSb $m_a^*/m_o = 0.55 \pm 0.06$, $m_b^*/m_o = 1.23 \pm 0.12$, and $m_c^*/m_o = 0.34 \pm 0.03$. For CdSb the values are $m_a^*/m_o = 1.26 \pm 0.13$, $m_b^*/m_o = 0.69 \pm 0.07$, and $m_c^*/m_o = 0.44 \pm 0.04$. An anisotropic relaxation time was observed in both materials. The ratio of the relaxation coefficients $A_a : A_b : A_c$ is 1.0 : 1.4 : 1.0 for ZnSb and 3.3 : 2.5 : 1.0 for CdSb. The data for both materials supports a model which has a single, non-degenerate extremum in the valence band.

In Chapter V the experimental data from alloy samples is presented and then discussed. Free carrier absorption, electrical conductivity, and Hall coefficient were measured for the a and b axes of the alloys across the entire composition range. The scattering in the alloy system, discussed in Appendix 3, is such that the same scheme may be used to extract the m_i^*'s and A_i's as was used for ZnSb and CdSb. The data for m_a^*/m_o versus composition shows only a slight deviation from a linear variation. The data for m_b^*/m_o shows a substantial increase with x and then a sharp decrease near x = 1 for $Cd_xZn_{1-x}Sb$. The relaxation time is found to be anisotropic only for low alloy concentrations near ZnSb or CdSb. An isotropic relaxation time is observed over the midrange of

alloy composition. There is not enough data available to make a model to account for the variation of effective masses with composition. Several highly oversimplified models are discussed to lend plausibility to the observed variations.

Finally, Chapter VI contains a summary and suggestions for future work.

REFERENCES

1. K. Almin, Acta Chemica Scandinavica, 2, 400 (1948).

2. M. Hansen, Constitution of Binary Alloys, McGraw Hill, N. Y. (1958).

3. V. Frei and B. Velicky, Czech. J. Phys., B15, 43, (1965).

4. V. Khartsiev, Soviet Physics-Solid State, 4, 721 (1962).

5. R. Eisner, R. Mazelsky, and W. Tiller, Journ. Applied Physics, 32, 1833 (1961).

6. M. Zavetova, Physica Status Solidi, 5, K19 (1964).

7. H. Komiya, K. Masumoto, and H. Fan, Phys. Rev., 133, A1679 (1964).

8. M. V. Kot and I. V. Kretsu, Fiz. Tverdogo Tela, 2, 1250 (1960).

9. P. Shaver and J. Blair, Phys. Rev., 141, 649 (1966).

10. M. Zavetova, Czech J. Physics, 14, 271 (1964).

11. J. Tauc and A. Abraham, Czech J. Physics, 15, 731 (1965).

12. F. Ermanis and E. Miller, Journ. Electrochem. Soc., 108, 1048 (1961).

13. I. K. Andronik, M. V. Kot, and O. V. Emel'yaneko, Soviet Physics-Solid State, 3, 1853 (1962).

14. L. Stourac, Czech J. Physics, B15, 140 (1965).

15. V. Frei, M. Matyas, B. Velicky, M. Zavetova, and J. Skacha, Proc. Int. Conf. on Physics of Semiconductors at Exeter (1962), p. 766.

16. T. Kawasaki and T. Tanaka, Japan J. Phys., 2, 516 (1963).

17. I. K. Andronik and M. V. Kot, Fiz. Tverdogo Tela, 2, 1128 (1960).

18. I. K. Andronik and M. V. Kot, Izv. Akad. Nauk. SSSR Ser. Fiz., 28, 1028 (1964).

19. K. Toman, Phys. and Chem. of Solids, 11, 342 (1959).

20. M. Miksovsky, K. Smirous, K. Toman, Proc. of the Int. Conf. on Semiconductor Physics, Prague (1960), p. 1087.

21. Ya. Keloglu and A. Fedorko, Russian Journ. of Inorganic Chem., 9, 1036 (1964).

22. E. Justi, E. Lang and G. Schneider, Advanced Energy Conversion, 4, 15 (1963).

23. Ya. Ugai and E. Averbakh, Izv. Akad. Nauk. SSSR Ser. Fiz., 28, 1044 (1964).

24. L. Stourac, J. Tauc and M. Zavetova, Proc. of the Int. Conf. on Semiconductor Physics, Prague (1960), p. 1091.

25. M. Stevenson, Proc. of the Int. Conf. on Semiconductor Physics, Prague (1960), p. 1083.

CHAPTER II. MATERIAL AND SAMPLE PREPARATION

2.1 Growth of ZnSb

The first step in any material study involves the acquisition of single crystal material for preparing samples. As neither ZnSb nor CdSb is presently of economic importance, single crystal material is not commercially available. Thus all of the material that was used had to be grown in the laboratory.

ZnSb has a melting point of 546° C and neither Zn nor Sb has an excessive vapor pressure at temperatures slightly above this. Thus the growth of single crystal material should not be too difficult. The major difficulty arises in the complex phase diagram of the Zn-Sb system[1] shown in Figure 2.1. In the phase diagram, Zn_4Sb_3 can exist in two modifications indicated by β and γ. Also Zn_3Sb_2 can exist in three modifications ε, ζ, and η. In both cases the modifications differ in their microstructure.[1]

If a stoichiometric melt of ZnSb is cooled, an incongruent melting point prevents the formation of ZnSb. This is best illustrated on Figure 2.2 where a portion of the Zn-Sb phase diagram, Figure 2.1, has been enlarged. Point L_1 in Figure 2.2 represents molten stoichiometric ZnSb. As the temperature is decreased, the melt moves along the line L_1A until point A is reached. At this point solid material Zn_4Sb_3 and excess Sb in

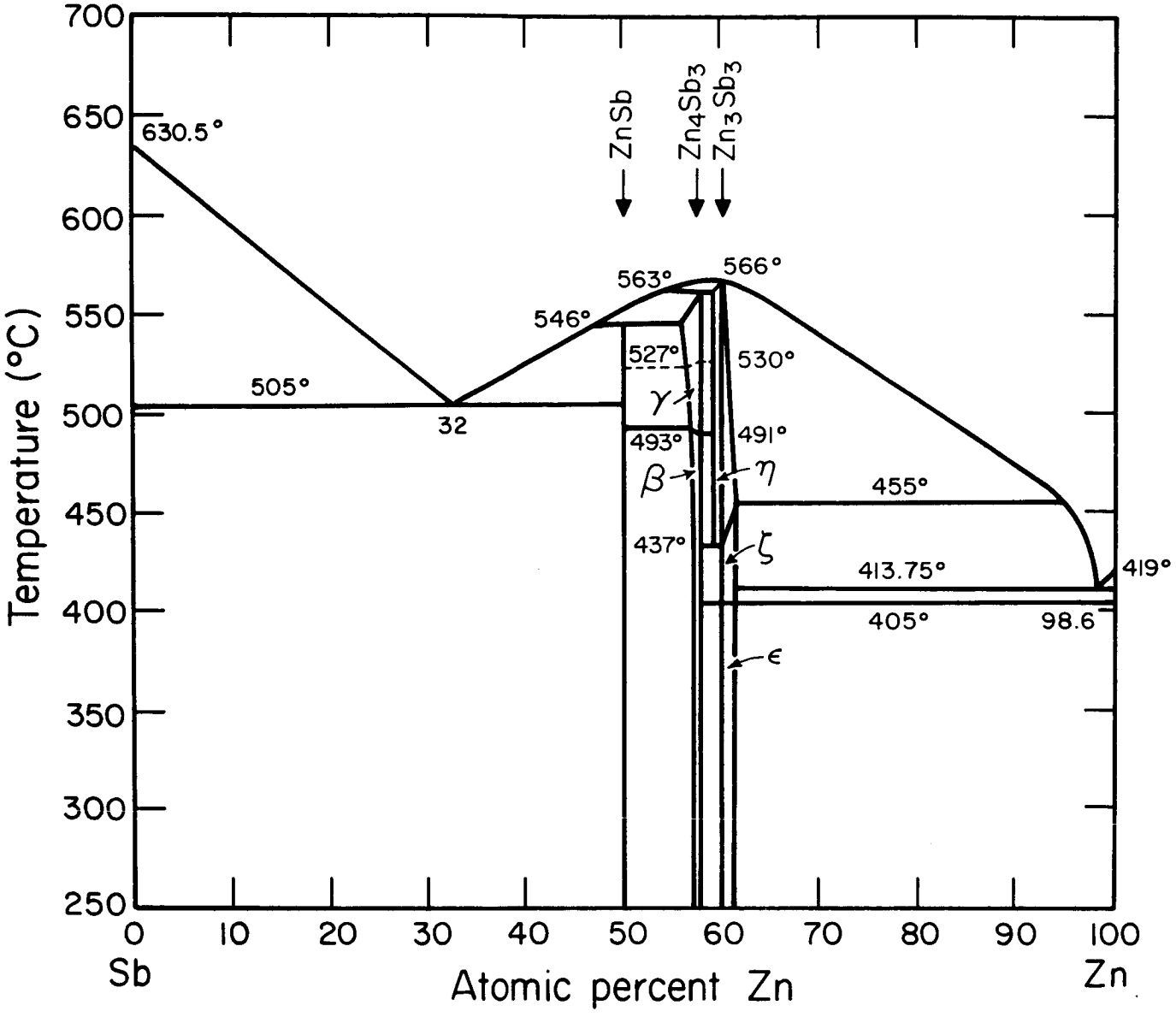

Figure 2.1. Phase diagram of the Zn-Sb system from Hansen.[1]

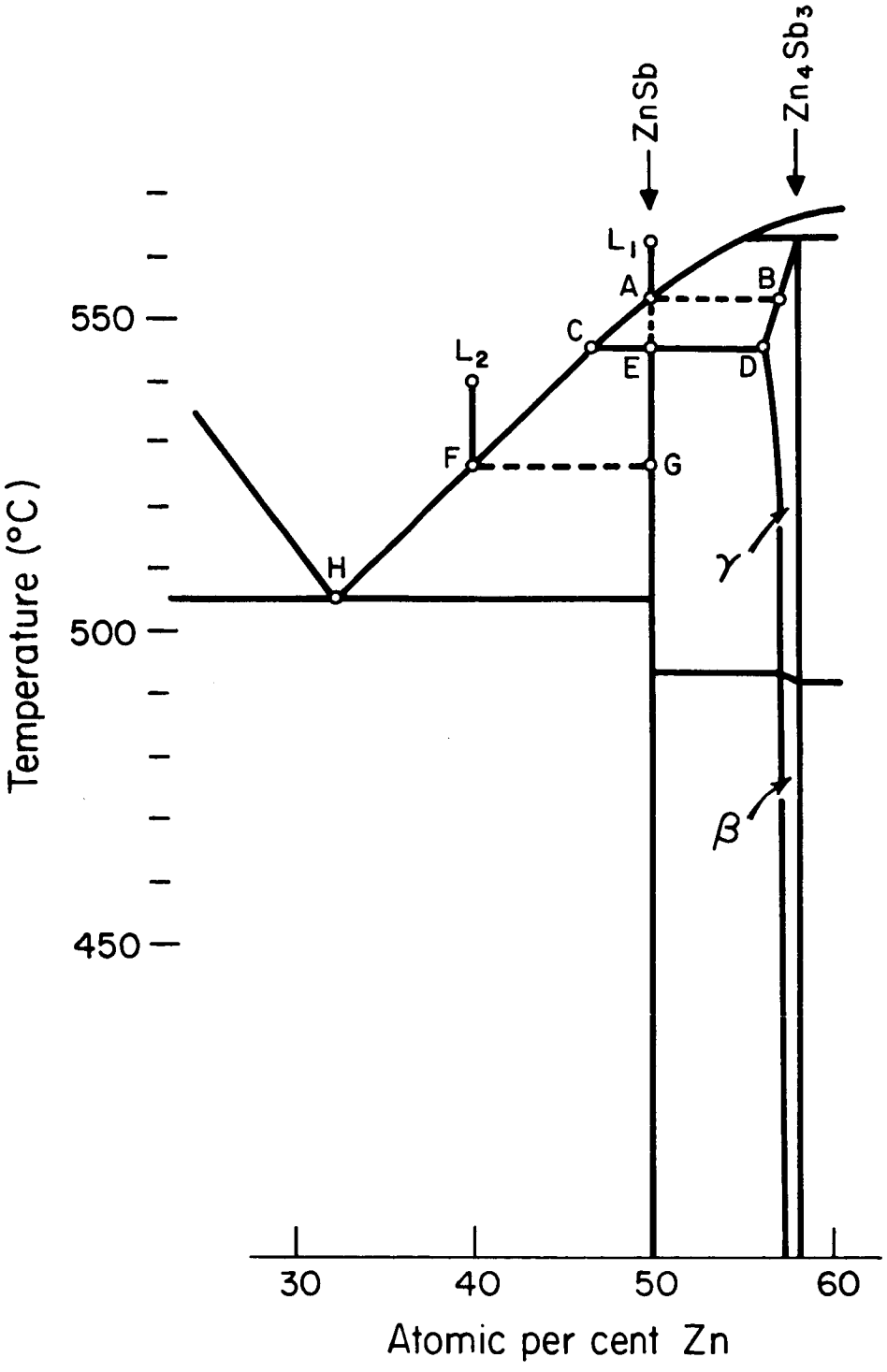

Figure 2.2. Portion of Zn-Sb system phase diagram from Hansen.[1]

a microstructure represented by γ starts to form. This solid material is represented by point B. As the material is cooled further, more solid material forms and the melt moves along the line CA until point C is reached. At point E, the solid material which has frozen out reacts with the melt to form ZnSb. That is, at 546° C, the melt will have composition C and the solid will have composition D. Both will react to form ZnSb represented by point E. Needless to say this is not a satisfactory reaction for forming single crystal material.

A more satisfactory method of forming ZnSb is obtained by using an Sb rich melt to avoid the horizontal peritectic in the phase diagram. This technique can also be illustrated on Figure 2.2. Point L_2 represents a melt containing 40 atomic per cent Zn and 60 atomic per cent Sb. As the melt is cooled, nothing happens until point F is reached. At F, solid ZnSb represented by point G starts to form. This form of freezing out ZnSb directly can be utilized in single crystal growth. The solid material thus formed can be removed from interaction with the melt and cooled without any further phase changes.

The method used for growing ZnSb was developed by P. Shaver at this laboratory. It has been described in detail elsewhere[2] and will be only outlined here.

First, two charges for use in the growth process must be

formed. One is a stoichiometric charge of ZnSb weighing approximately 50 grams and the other is a zone leveling charge containing 60 atomic per cent Sb and 40 atomic per cent Zn and weighing approximately 10 grams. The determined amounts of 99.999 % pure Sb and 99.999 % pure Zn are weighed to within 0.1 milligram for each charge. The material for each charge is then inserted in a quartz ampoule of 13 mm inside diameter and sealed off at a pressure of 10^{-5} mmHg. Next each ampoule is placed in a furnace which is rocking mechanically. Here the material is heated to a temperature of 700^{o} C to melt and react the elements. Each ampoule is removed while hot and quenched in water to freeze the charge material in an approximately horizontal position.

The charges are removed from their ampoules and are assembled with a piece of single crystal ZnSb in a 15 mm inside diameter Vycor tube. The inside wall of the tube is carbonized by incomplete combustion of acetone prior to insertion of the charges. The charge containing excess Sb is placed between the single crystal seed and the larger stoichiometric charge. The tube is sealed containing Argon gas, incandescent lamp grade, at atmospheric pressure.

The assembled growth charge in its Vycor ampoule is placed in a horizontal zone furnace designed by P. Shaver and sketched

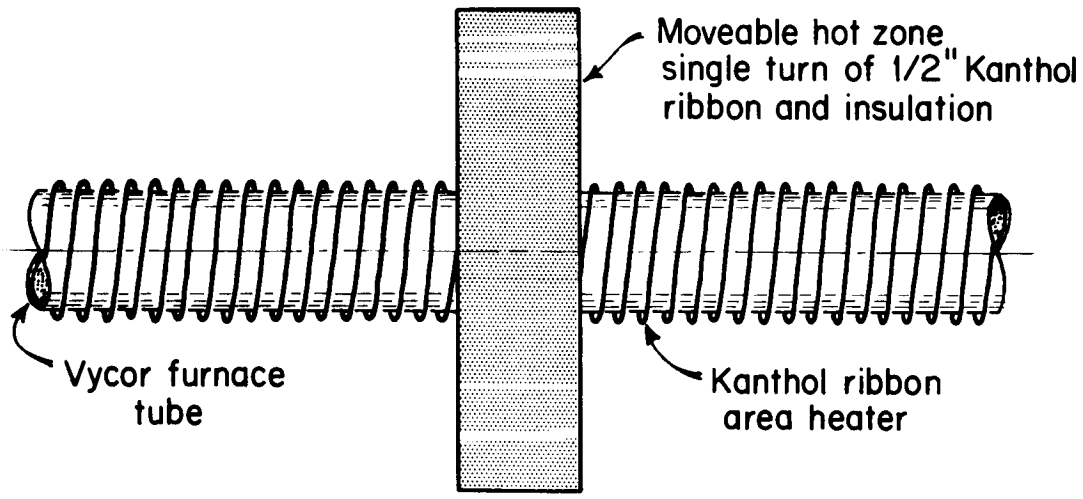

Figure 2.3. Horizontal zone furnace configuration used in single crystal growth.

in Figure 2.3. The furnace consists of an 18 mm inside diameter Vycor tube about 75 cm in length. A Kanthal ribbon heating element is wound uniformly around the outside of the furnace tube. This composes the area heater designed to maintain a uniform temperature over the length of the tube. A hot zone consisting of a single turn of one-half inch Kanthal ribbon is mounted around the tube and can be moved along the tube via a feed screw. The charge is located in the furnace tube so that the zone heater is around the excess Sb charge. Then the furnace is brought up to operating temperatures of 415° C for the area heater and 580°C for the zone heater. This heating process is done gradually over a period of two hours to avoid subjecting the single crystal seed to a severe thermal shock.

The actual growth process consists of melting back into the seed and then allowing the molten material to freeze at the single crystal-melt interface. This is accomplished by moving the hot zone towards the seed at a speed of .030 inch per hour until a portion of the seed is molten. Then the direction of travel of the zone is reversed and the zone is allowed to proceed the length of the charge. The rate of travel is maintained at .030 inch per hour to allow the excess Sb to diffuse away from the growth interface. The seed crystal will

induce single crystal growth in the rest of the ingot if the technique works properly.

Upon completion of the growth process, the furnace is slowly cooled and the ampoule is removed and opened. Sandblasting the lower surface of the ingot reveals the crystal quality. The anisotropic thermal expansion causes easily visible cracking if the material is not a single crystal. Sometimes low angle boundaries are present and can be detected as slight differences in reflectivity between regions of the sandblasted material.

The resulting single crystal ingots are typically about 12 cm long and have an almost semicircular cross section 15 mm in diameter. Laue x-ray photographs taken with Cu or Mo radiation show the diffraction spots to be quite sharp and without structure on the better ingots. This is indicative of good crystal quality and the absence of strained regions.

No dopants were added to the material. The initial seeds were obtained from P. Shaver and had traces of Cu, an acceptor, doping present. Hall measurements show the resulting crystals to be p-type with carrier density typically of the order of 3×10^{16} cm^{-3}. There is no information available as to the presence or absence of excess Sb in the crystals. Wet chemical analysis is not sensitive enough to detect this. There is some

evidence which shows that deviations from stoichiometry act as dopants to the material. This is furnished by the phenomenon of irreversible changes in carrier concentration that is caused by heating undoped material and has been investigated by Shaver.[2]

2.2 Growth of CdSb

CdSb is not presently available commercially and thus single crystal material must be grown in the laboratory. This material is similar to ZnSb in that both have comparable melting points and for both the vapor pressure of the constituents is not excessive near the melting point. One look at the phase diagram of the Cd-Sb system shown in Figure 2.4 shows the essential difference in the crystal growth problem from ZnSb. While ZnSb formed via a horizontal peritectic, CdSb can form directly from a stoichiometric melt. However, the formation is slightly complicated by the presence of a metastable system shown by broken lines in the phase diagram.

If a stoichiometric mixture of CdSb is heated well above 456° C, the melting point of CdSb, and allowed to cool, the liquid will not solidify again at 456° C. Instead the liquid will supercool to the metastable Cd_3Sb_2 portion of the phase diagram where Cd_3Sb_2 and excess Sb will result. On further cooling, at temperatures between about 250 and 350° C the metastable system transforms into the stable one. In this

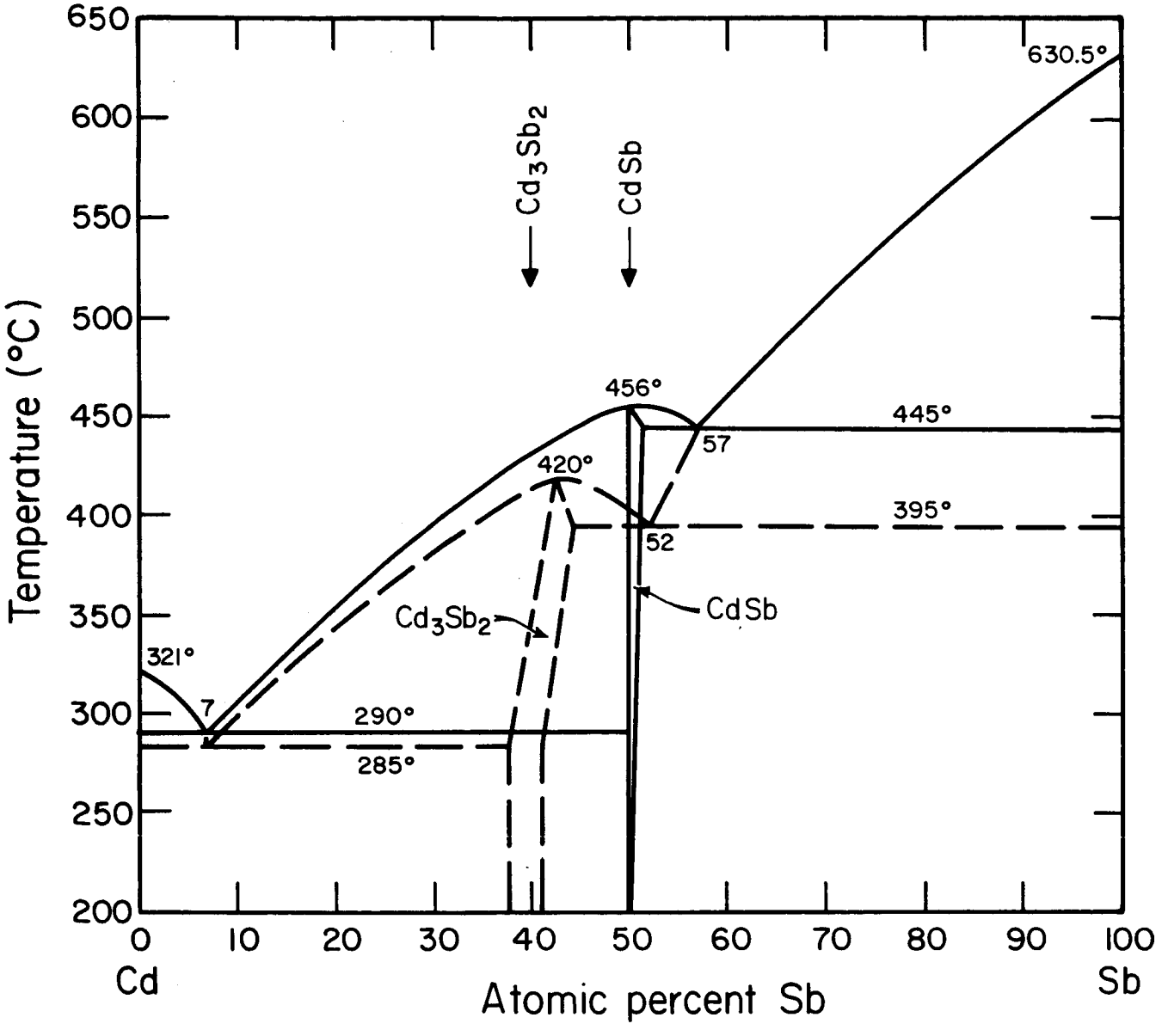

Figure 2.4. Phase diagram of the Cd-Sb system from Hansen.[3]

transformation solid Cd_3Sb_2 and Sb turns into CdSb exothermally. This type of reaction is not conducive to single crystal formation.

If at 456° C the CdSb phase is nucleated, the liquid does not supercool but will form stable CdSb directly. Thus single crystal material can be grown from a stoichiometric melt if a CdSb seed is available. Ermanis and Miller[4] have found that if the melt is not heated over 15° C above the melting point of CdSb, the stable phase will be nucleated upon cooling. This technique was used to obtain the initial single crystals which then could be used as seeds.

The ZnSb furnace and controllers were also used to grow CdSb. The molten Cd reacted with quartz so that it was necessary to carbonize the walls of the reaction ampoules as well as the walls of the growth ampoules. The first crystal of CdSb was grown by placing a reacted stoichiometric charge into the growth ampoule by itself. The zone temperature on the furnace was adjusted to 461° C and the area temperature to 320° C. The hot zone was then allowed to traverse the entire length of the charge. On opening the tube, the material was found to have formed a single crystal. Once a source of seed crystals was thus obtained, subsequent crystals were grown by assembling a

single crystal seed and a stoichiometric charge in a growth ampoule and then melting back into the seed to initiate single crystal growth. It was not necessary to use a zone leveling charge containing excess Sb as was used for ZnSb.

The resulting crystals were similar in size and appearance to the ZnSb crystals. As before, sandblasting the lower surface revealed the crystal quality. Later Hall measurements revealed that the carrier concentration was about 3×10^{16} cm^{-3} and all crystals as grown, undoped are p-type. Two attempts were made at growing single crystals without seeds and both were successful. Six attempts at growing single crystals by melting back onto seeds were made. Of the six, three were successful. The other three did not initiate single crystal growth at the seed-melt interface and were polycrystalline.

2.3 Growth of $Cd_xZn_{1-x}Sb$ Alloys

The growth of single crystal regions of $Cd_xZn_{1-x}Sb$ alloys is complicated by the incongruent melting point of ZnSb at low Cd concentrations and by the formation of metastable Cd_3Sb_2 at low Zn concentrations. These problems can be overcome by using a zone leveling charge containing excess Sb when x is close to 0 and by initiating stable growth by means of single crystal seeds for all values of x. The liquidus-solidus lines for the pseudobinary system CdSb-ZnSb have been determined from thermal

analysis by Keloglu and Fedorko[5] and by Ermanis, Miller, and Cadoff[6] and are shown in Figure 2.5.

The same horizontal zone furnace was used to grow these crystals also. In order to span the entire composition range, the main growth charges of $Cd_xZn_{1-x}Sb$ were made with x ranging from 0.1 to 0.9 in 0.1 increments. For x in the range $0 \leqslant x \ll 0.30$, it was necessary to use a zone leveling charge. Table 2.1 shows the composition of zone leveling charge, area temperature, and hot zone temperature that were used for a given main charge composition. When a single crystal seed having the desired composition was not available, one was used which differed by not more than 10% in composition. In this way a large lattice mismatch is avoided when nucleating single crystal growth. By these techniques single crystal alloy ingots were grown from melts spanning the entire composition range.

The large splitting of the solidus-liquidus lines shown in Figure 2.5 affects crystal composition in the following way. If a melt of a given composition alloy is cooled, the composition alloy which freezes out is not that of the melt but rather that of the point on the solidus line corresponding to the minimum liquid temperature of the melt composition. For example if on Figure 2.5 a melt at composition A is cooled the solid

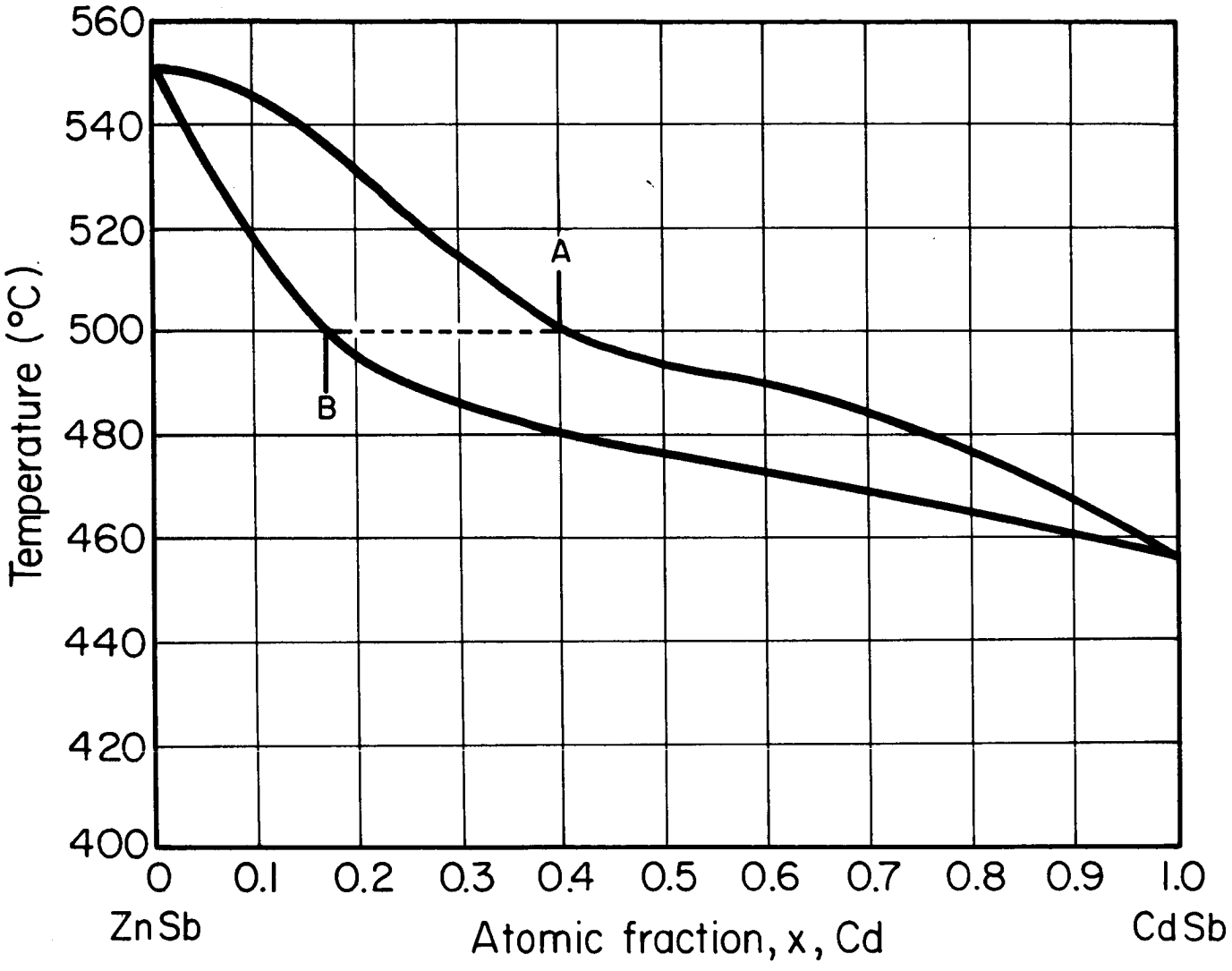

Figure 2.5. Melting range for the stable pseudobinary system $Cd_xZn_{1-x}Sb$ from Ermanis, Miller and Cadoff.[6]

Main Charge Composition	Zone-leveling Charge Composition	Area Temp. °C	Hot Zone Temperature °C
ZbSb	$Zn_{1.0}Sb_{1.2}$	415	580
$Cd_{0.1}Zn_{0.9}Sb$	$Cd_{0.1}An_{0.9}Sb_{1.15}$	410	570
$Cd_{0.2}Zn_{0.8}Sb$	$Cd_{0.2}Zn_{0.8}Sb_{1.10}$	400	560
$Cd_{0.3}Zn_{0.7}Sb$	$Cd_{0.3}Zn_{0.7}Sb_{1.05}$	390	550
$Cd_{0.4}Zn_{0.6}Sb$	none	380	540
$Cd_{0.5}Zn_{0.5}Sb$	none	370	530
$Cd_{0.6}Zn_{0.4}Sb$	none	360	520
$Cd_{0.7}Zn_{0.3}Sb$	none	350	510
$Cd_{0.8}Zn_{0.2}Sb$	none	340	500
$Cd_{0.9}Zn_{0.1}Sb$	none	330	490
CdSb	none	320	480

Table 2.1. Charge composition and furnace temperatures used in crystal growth.

material which freezes out will be of composition B. In $Cd_xZn_{1-x}Sb$ alloys, this acts to make the solid material richer in Zn than the melt. As the melt is depleted of its Zn content, its composition changes and in turn changes the resulting solid composition. Thus a very slight grading in composition is obtained over the length of the ingot. The region near the seed is richer in Zn than the region near the other end of the ingot. Over the distance of 1 cm, no change in lattice constant could be detected due to this grading. Therefore over 1 cm, the grading in composition was less than 0.01 in x. Over larger distances, 2 or 3 cm, a change in lattice constant of 0.01 A^o was detected. This indicated changes in x by 0.02 over 2 or 3 cm. For this reason all measurements on a given composition alloy were made on samples taken from an ingot section no longer than 1 cm.

When the growth process was carried out properly and seeding was accomplished successfully, the single crystal ingots appeared to be of good quality by both visual and x-ray examination. The frequency of the appearance of low angle grain boundaries was higher for alloy ingots than for the end compounds ZnSb and CdSb. At one point a twin developed in an ingot and being undetected at the time was perpetuated through several ingots which used seeds from the original twinned crystal.

The twin was later detected by Laue x-ray photographs of an oriented slice. One half of the area of the twinned slice was perpendicular to the c axis while the other half was 7^{o} away from the c axis. After this discovery all alloy regions were checked for the presence of twins by x-ray means before they were cut into measurement samples. Through the attempted growth of about forty alloy ingots, good quality single crystal material was obtained over the entire composition range. About 50% of the growth attempts resulted in usable material. The major causes of failure were polycrystalline growth initiated at seed interface and complete melting of seed during the meltback process due to improper furnace temperatures. No evidence of long range ordering in the alloy crystals was ever observed in the many x-ray measurements made on the material.

2.4 Preparation of Optical Samples

The orthorhombic symmetry of ZnSb, CdSb, and their alloys leads to anisotropic optical and transport properties. Measuring these properties requires accurately oriented samples. As discussed in Appendix 2, by having the electric vector of the incident radiation parallel to a crystollographic axis, the optical properties of that crystal direction alone are observed.

Thus as a first step in preparing optical samples it is necessary to orient the starting material. Regions of single

crystal ingots were mounted on a goniometer in order to locate the principal axes by means of Laue back reflection photographs with x-rays. For most of the work a Cu x-ray tube and Polaroid film were used to obtain intense spots in a minimum amount of time. For better resolution, as occasion demanded it, a Mo tube and conventional x-ray film were used with a correspondingly longer exposure time. The initial photographs of each ingot were searched for points which looked like the intersection of two mirror planes. All likely spots were brought in to the center of the film in subsequent exposures and examined to see if they had the required symmetry. When the correct point was identified and brought in to the center of the film, the resulting picture of dots formed two perpendicular mirror planes intersecting at the center of the film. When in this position the film plane is perpendicular to one principal axis and parallel to a plane containing the other two principal axes.

At this point it is necessary to identify the principal axis that was found. For this purpose a section of the material was sliced off to yield a plane face perpendicular to the axis. The material was then aligned in the sample holder of a Norelco diffractometer so that the cut face was parallel to the reference plane of the instrument. That is, when the x-ray source beam and the Gieger tube detector were 180^{o} apart the collimated

x-ray beam would just pass over the sample parallel to the cut face. Then the instrument was used to scan the angular range in which the diffraction peaks of the principal axes were known to lie. In the D_{2h}^{15} space group to which the crystals belong the diffraction peaks having Miller indices (h00), (0k0), and (00ℓ) are systematically absent for h, k, or ℓ odd.[7] Thus the refraction peaks obtained were (200), (400), (600), etc., or their equivalent for the other axes. From the angular location of the observed peaks and using tables for a Cu tube, the spacing of the planes causing the diffraction peaks could be obtained. In turn the lattice parameter of the principal axis perpendicular to the face then could be calculated. The observed peaks were extremely strong so that the x-ray tube had to be operated at the lowest power possible to keep the peaks from driving the diffractometer output recorder off scale.

Comparison of the resulting lattice parameter with tables for those of the ZnSb-CdSb alloy system[5] yielded the identification of the axis as a, b, or c. In cases where there was any doubt because of composition uncertainty, a second axis was found and identified in the same manner before axis labels were assigned to the material. In all cases a second principal axis was found and identified so that the location of all three major axes in the crystal were known. For all of the grown

material the c axis was found to be the closest principal axis to the ingot growth axis. The seeds were not oriented since a close fit to the growth tube curvature was more important than orientation for initiating growth.

The material was then mounted on a goniometer and oriented slices perpendicular to a known principal axis were cut from the ingot. Initially the slices were cut by using a Felker diamond saw. As the material is both soft and brittle, the breakage rate was alarmingly high. A Servomet spark gap cutter was also employed to cut material,but it also was not completely satisfactory. The cutting speed was both slow and unpredictable depending on the condition of the tungsten wire blade. A new blade cut extremely slowly if at all. Then the cutting rate would speed up as the blade aged, but by this time the blade would have eroded enough to cause irregular cuts before eventually breaking. The most satisfactory method used was to cut the slices off with a string saw. The string saw was built in this laboratory from sketches of an original model designed by J. B. Gunn of IBM Laboratories.[8] In cutting, a loop of Nichrome wire bearing a slurry of 600 grit SiC and oil is drawn over the sample. This method gave extremely high yields of properly cut slices with a surface finish comparable to that obtained by lapping.

In order to polish and lap the samples to a high degree of flatness, a special jig was made from stainless steel stock. The jig had a large outside diameter of 3" but its lower surface was relieved so that only the outer 1/2" of the jig touched the polishing wheel. The jig had a 1" diameter plunger which was keyed to prevent the plunger from rotating relative to the rest of the jig. With the plunger in place the lower surface of both were ground to a flatness better than .001" per inch in the Material Science Center Machine Shop.

Thick optical samples, typically 2 mm, for the determination of absorption coefficients were made from initially 3 or 4 mm thick slices of material in the following way. The slice was mounted firmly on the jig plunger using glycol phthalate mount cement. The slice mounted on the jig was then wet lapped on No. 600 wet or dry paper placed on a granite flat to remove the surface damage caused by slicing. The granite flat was 8" x 12" and was flat to .005" over 12 inches. The slice face was then polished with Linde A powder on a velvet covered polishing wheel followed by Linde B powder on a velvet wheel until a suitable scratch-free polished surface was obtained. The slice was then removed from the jig, turned over, and remounted. The second surface was lapped until the desired thickness was obtained and polished in the same manner. The

slice was then removed from the jig, washed in acetone and methyl alcohol, and measured for thickness using a machinist's dial gauge with a 2 micron minimum division. The polished slice was then mounted with Apiezon wax, thinned with trichloroethylene, on a flat washer having a circular aperture of maximum diameter that the sample could completely cover. This washer served as a convenient optical mount for the sample.

Extremely thin optical samples for use in determining the refractive indices were obtained in the following way. A slice initially about 2 mm thick was mounted on the jig and then lapped and polished on one side as previously described. Next, the slice was dismounted and measured for thickness. The slice was mounted again on the jig with the polished side towards the jig. Great care was taken to assure firm contact and flatness at the jig-sample interface. The amount of material to be removed was calculated from the present thickness of the sample and the desired thickness of the sample allowing 10 microns for the final polishing. The material was then lapped to the desired thickness measured by a dial gauge set from the face of the sample to the opposite end of the plunger. After lapping the face was polished and the slice was carefully removed and placed on a mounting washer. The thickness was not measured until the optical measurements were made because the samples

often cleaved while being measured for thickness. The material has easy cleavage planes perpendicular to the a and c axes.

The thin samples thus obtained were between 28 and 40 microns in thickness. The better samples had only a 2 micron taper in thickness over 1 cm while the worst had 9 or 10. The requirement on surface flatness and paralellism is high to obtain interference effects in transmission. The degree to which the requirement is met can be easily determined by the quality of the interference fringes obtained in the optical measurements. The yield of suitable samples using this technique was about one in three. It was found that a taper of more than about 10% of the sample's thickness over 1 cm did not yield any fringes.

After the samples had been mounted on their final mounts for measuring, they were x-rayed again to determine the direction of the principal axes in the sample plane. The directions of these axes along with their identity were marked on the outer edge of the mounting washers. This enabled the samples to be aligned easily with the polarizers during the subsequent optical measurements.

2.5 Preparation of Hall Effect and Conductivity Samples

For the purpose of conductivity and Hall effect measurements, rectangular parallelepiped shaped samples having six electrical contacts are required. For ease in interpreting the measurements, the principal axes of the material should be parallel to the sample edges. Usually several samples having their longest edge parallel to a crystallographic axis are required for measurements pertaining to the axis.

The oriented samples are obtained in the following way. Slices are cut as previously described perpendicular to a known crystallographic axis with the string saw or spark gap cutter. The slices are then mounted on graphite blocks if the string saw is to be used or brass blocks if the spark cutter is to be used. The blocks in turn are mounted on a goniometer and a Laue photograph is taken of the sample. From the resulting Laue pattern the direction of the principal axes in the slice are marked on the slice and mounting block. The axes are identified by the relation of the slice being used to the remainder of the ingot for which the axes are known. The samples are cut parallel to the desired axis on the saw or spark cutter, dismounted from the cutting block, washed in acetone, and sandblasted to remove foreign surface material.

Contacts and leads are then placed on the samples. Pb-Sn

solder applied with a rosin flux makes very nice ohmic contacts to ZnSb, CdSb, and their alloys. The contacts are made with an extremely small soldering iron to minimize contact diameter. Figure 2.6 shows the contact configuration used and also shows typical sample dimensions. Copper wire of 3 mil diameter is used for the leads. The sample dimensions are obtained by viewing the samples in a Unitron metallographic microscope having two degrees of movement controlled by barrel micrometers with .0001" divisions. This method was found to be more satisfactory than measuring the samples with a hand held micrometer.

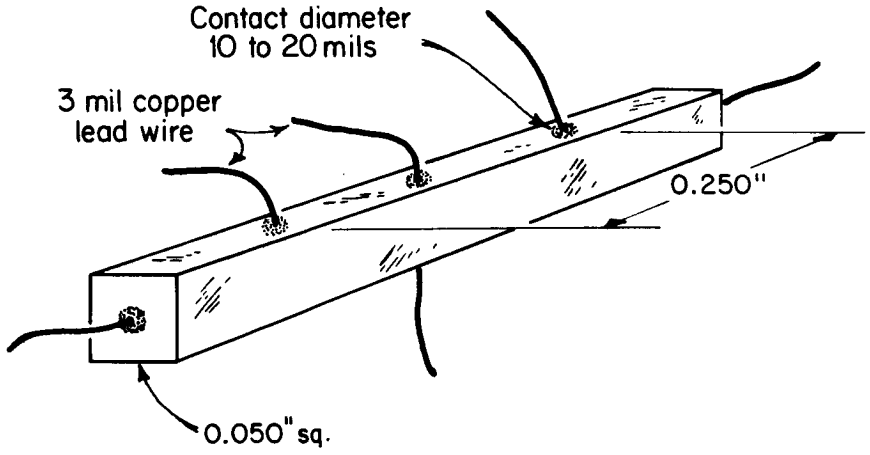

Figure 2.6. Hall effect and conductivity sample showing contact configuration and typical dimensions.

REFERENCES

1. M. Hansen, Constitution of Binary Alloys, p. 1184, McGraw Hill Inc., New York, N.Y., 1958.

2. P. Shaver, "Thermal and Electronic Transport Properties of Zinc Antimonide", M.I.T., Sc.D. Thesis, April, 1965.

3. M. Hansen, Constitution of Binary Alloys, P. 438, McGraw Hill Inc., New York, N.Y., 1958.

4. F. Ermanis and E. Miller, Journ. of Electrochem. Soc., 108, 1048 (1961).

5. Yu. P. Keloglu and A. S. Fedorko, Russian Journ. of Inorganic Chem., 9, 103 (1964).

6. F. Ermanis, E. Miller, and I. Cadoff, "Materials for Thermoelectric Generators", AD264375, U.S. Dept. of Commerce.

7. K. E. Almin, Acta Chemica Scandinavia, 2, 400 (1948).

8. String saw built by Materials Science Center machinist from sketches supplied by J. B. Gunn of IBM Watson Laboratories, Yorktown, N.Y.

CHAPTER III. EXPERIMENTAL PROCEDURES

3.1 Determination of Sample Composition

For the analysis of experimental data on the alloy samples $Cd_xZn_{1-x}Sb$, it is necessary to know the sample composition. Four methods were used for determining sample composition, namely density measurements, x-ray fluorescence, wet chemical analysis, and lattice parameter measurements. The latter two, wet chemical analysis and lattice parameter measurements, proved to be the most useful. However, the lattice parameter measurements are easier to make, faster, and non-destructive compared to wet chemical analysis and were used for sample composition in most of the work.

With equipment for precision density measurements belonging to the Laboratory for Insulation Research the densities of ZnSb and CdSb single crystal samples were measured. The method used was to measure the buoyancy of the sample in dibromyl propane which has a density of approximately 1.968 grams/cm^3. For ZnSb the density 6.337 grams/cm^3 was obtained as compared to the theoretical value of 6.36 grams/cm^3 obtained from the unit cell dimensions. The major part of the discrepancy was due to insufficient outgassing of the sample. The immersed sample was removed from the vacuum pump before all boiling had ceased. For CdSb the density 6.823 gram/cm^3 was obtained

compared to the theoretical value of 6.83 gram/cm^3. Here the discrepancy was due to small voids and irregularities on the upper surface of the sample. Because of the poor quality of the top surface of the grown ingots and the relatively large sections required for an accurate density measurement, it was decided to seek other means of determining sample composition.

X-ray fluorescence was used in an attempt to obtain sample composition. In this method the sample is bombarded by high energy x-rays to stimulate x-ray fluorescence in the sample. The radiation given off by the sample is analyzed in an x-ray spectrometer utilizing a LiF crystal and a geiger tube detector. The angular position of emission lines characteristic of the elements are listed in tables. Then from the position of the line the emitting element can be identified and from the intensity of the line the quantity of the element present is inferred. Initially, polycrystalline alloy samples of known composition were prepared and reacted in an attempt at calibration of the process. The resulting x-ray line intensities were hardly dependent on sample composition in both powder and solid forms. Zinc atoms can absorb the fluorescence given off by cadmium and antimony atoms. This effect coupled with a very low x-ray penetration depth made the fluorescence more sensitive to local structure than to bulk sample composition. Then the fluorescence

of single crystal samples in both single crystal and powdered form was measured and compared with sample composition as obtained by wet chemical analysis. From these measurements it was concluded that x-ray fluorescence could be used to determine sample composition only to $\pm$ 10%.

The wet chemical analysis was done by the Analytical Chemical Laboratory at the Material Science Center. They encountered considerable difficulty in completely separating the cadmium and zinc from the antimony. The analyses was always destructive to about a gram of sample material. By this method sample composition could be determined to within $\pm$ 1%.

The variation of lattice constants with composition have been determined experimentally by Keloglu and Fedorko[1] and by Toman[2] and is shown in Figure 3.1. A slight deviation from a linear variation is observed which the authors maintain is an indication of long range ordering. However, the range over which there is a deviation from linearity in Reference 1 is substantially less than the range in Reference 2. Both observe a deviation in the midrange of composition from $0.3 < x < 0.7$. Considering the large split in the solidus-liquidus line as discussed in 2.3 and that they used reacted samples of known initial composition, it is quite possible that their actual

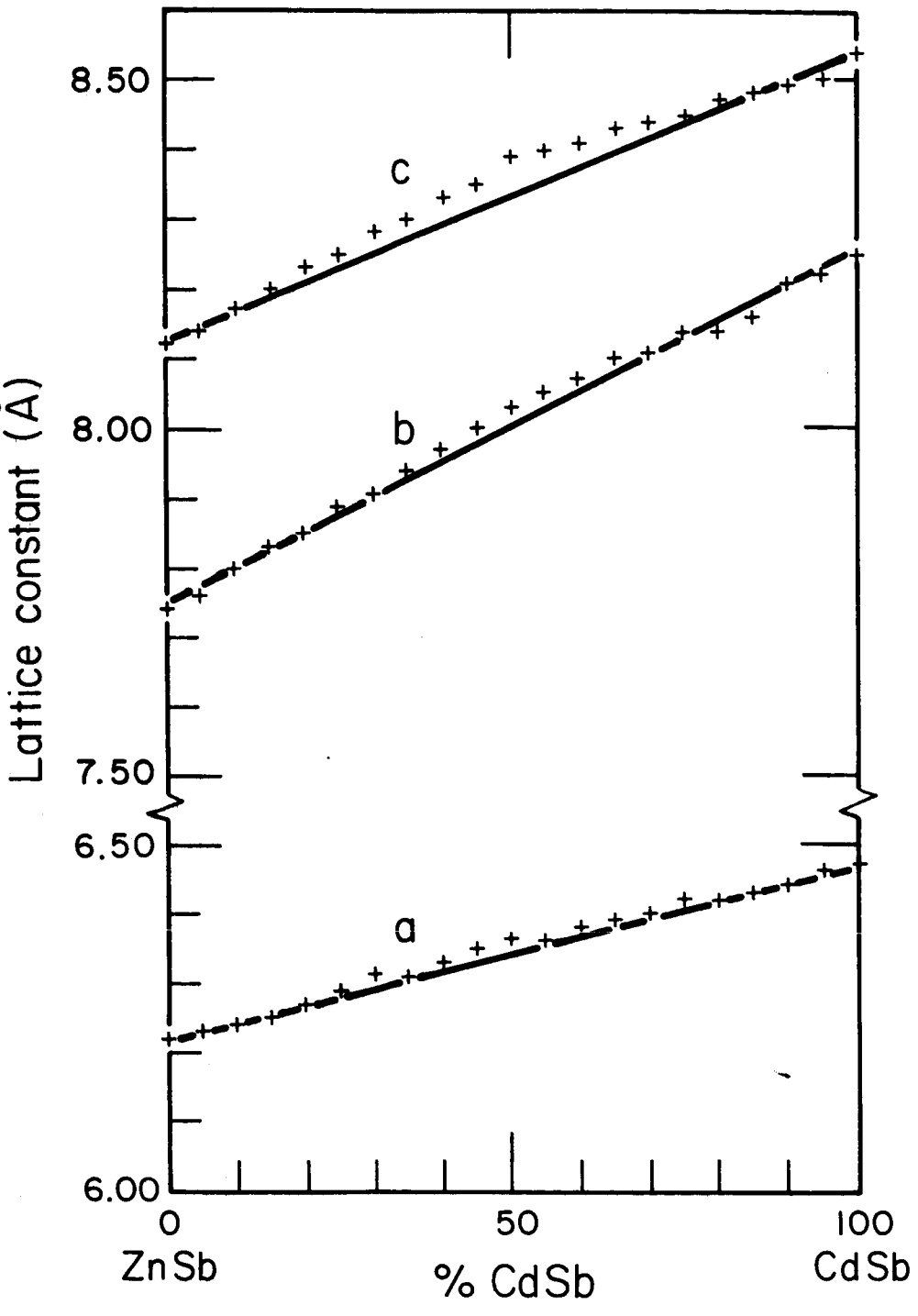

Figure 3.1. Lattice constant versus alloy composition from Keloglu and Fedorko.[1]

compositions are in error in this range. Even a 2% error in sample composition would make their experimental curves essentially straight lines.

Experimentally, the lattice constants were determined from single crystal samples with a Norelco diffractometer by the method described in 2.4. Usually the peaks having Miller indices (004), (006), and (008) or their counterparts for the other axes were scanned at a speed of 1/4 degree per minute. The machine error was less than 0.0035 degrees and peaks on the recorder chart could be located to within 0.01 degree. This angular error when converted to error in the computed lattice constant gives a 0.001 A^{o} error in lattice constant. This assumes that the crystal is oriented and aligned in the spectrometer perfectly. In practice, errors in orientation of the sample can be held to less than a degree. The observed diffractometer peaks are extremely large only when the sample is perfectly aligned. Thus the size of the peaks is indicative of the orientation accuracy. In many cases when the entire angular range was scanned for evidence of long range ordering, miscellaneous strong peaks appeared. Calculations showed the peaks to be from β radiation of the Cu x-ray tube and Fe α radiation arising from the impurity of the Cu anode diffracting on the (004), (006), or (008) planes. Thus the lattice constants

can be determined to within 1/2% quite easily by this method.

In the actual measurements on alloys reported, the sample composition was determined by measuring the lattice parameter and assuming a linear variation. If the departures from linearity reported by References 1 and 2 are true, the measurement gives the parameter x in $Cd_xZn_{1-x}Sb$ to within $\pm$ .01 for $0 < x < 0.3$ and $0.7 < x < 1.0$ and to within - .04 to - .01 for $0.3 < x < 0.7$. If the departures from linearity are not real, the measurement gives x to within $\pm$ 0.01 over the entire composition range.

When the lattice parameters of the alloy samples were measured, the following behavior was observed. The two axes for each region which were measured always gave the same composition when a linear variation of lattice constant with composition was assumed. This would not have happened if the deviations from linearity reported in Figure 3.1 by Keloglu and Fedorko[1] were real. Rather, the two determinations would have given different compositions wherever the lattice parameter curves versus composition departed from linearity.

To check the assignment of alloy composition given to the alloy optical samples, the samples were sent for wet chemical analysis after the measurements were completed. The chemical analysis determined the weight per cent of both Zn and Cd. These analysis results were checked against the x-ray method of determining composition. Of the eight alloys studied, five

agreed within one per cent in composition and three did not. The three for which the composition by both methods did not agree were alloys of low Cd concentration. The wet analysis was redone on these three samples. The new determination of weight per cent Zn agreed with the former while the determination of weight per cent Cd did not. Based on the weight per cent Zn the composition agreed with that determined by lattice parameter. The chemists in the analytical lab claimed that it is difficult to titrate completely small amounts of Cd to account for the discrepancies in their results.

Thus the evidence suggests that the alloy system does obey Vegard's law in that the lattice constants vary linearly with composition. Also the composition of the alloy samples is accurate to $\pm$ .01 in x.

3.2 Determination of the Refractive Indices

The aim of the optical portion of this work was to study the optical absorption of ZnSb, CdSb, and their alloys. The most convenient way to do this is to measure optical transmission and then convert the data to optical absorption. In order to achieve this conversion the refractive indices of the material must be known. As the refractive index data in the literature was sparse and incomplete in the wavelength range of 3 to 15 μ the refractive indices of ZnSb and CdSb were determined experimentally.

In order to perform the desired optical measurements on ZnSb, CdSb, and $Cd_xZn_{1-x}Sb$, an optical system to measure transmission of infrared radiation is necessary. The radiation should be monochromatic and linearly polarized. A Perkin-Elmer Model 112 spectrometer and its associated electronics was utilized with AgCl transmission polarizers and a NaCl prism to achieve this purpose in the wavelength range of 3 to 15 microns.

Figure 3.2 shows the arrangement of the optical system external to the spectrometer. The individual components are mounted on a heavy aluminum table to minimize vibration and facilitate alignment. The output of the spectrometer is reflected by a 6" diameter plane mirror onto a 10" diameter spherical mirror which focuses the radiation into a beam coming to a focus at the sample location. The envelope of this beam makes a 5^o angle with its center. A Reeder thermocouple detector and an ellipsoidal mirror having the sample at one focus and the thermocouple at the other are placed behind the sample.

Two PE transmission polarizers, each consisting of six AgCl single crystal sheets aligned near the Brewster's angle, were used. The one positioned in front of the sample served as a polarizer while the one behind the sample served as an analyzer. Each polarizer has the property that if completely unpolarized radiation in the wavelength region utilized, 3 to 15 microns,

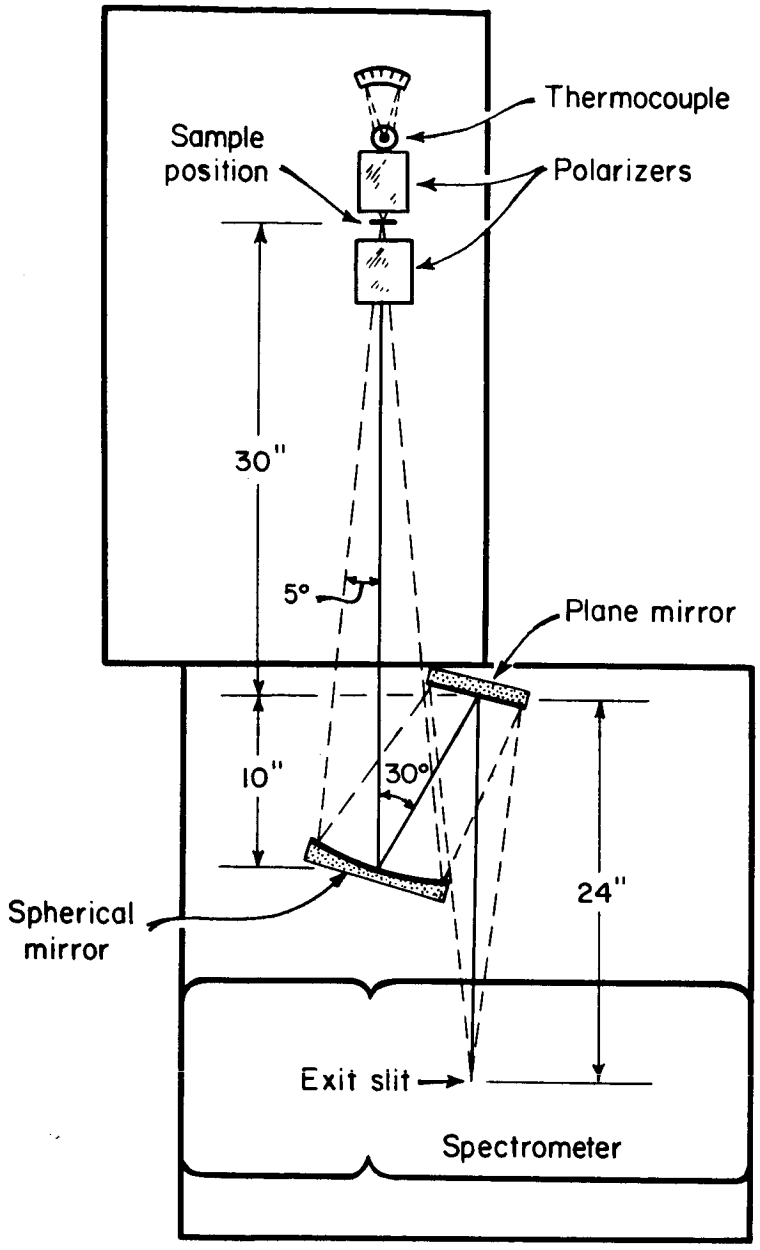

Figure 3.2. External optical arrangement.

is incident on the polarizer, the transmitted radiation is 94% polarized. That is, the ratio of the intensity of the radiation having its electric vector perpendicular to the desired direction, I_n, to the intensity of the radiation having its electric vector in the desired direction, I_p, is 0.06. The actual ratio of electric field strength is $E_n/E_p = 0.245$. Thus, when the two polarizers are aligned the net transmitted radiation will have an I_n/I_p ratio of 0.0036 and a field ratio of $E_n/E_p = 0.06$. The polarizers can be rotated about an axis through their center to change the direction of polarization. The polarizers were aligned horizontally or ninety degrees from the horizontal with a Starrett combination square containing a bubble level.

The signal from the thermocouple is sent through a PE thermocouple preamplifier to a PE 107 amplifier whose output is displayed on a Leeds and Northrup recorder. The rotation of the spectrometer's prism is controlled by a vernier drum. The drum number versus wavelength calibration was accomplished by locating known absorption lines in the NH_3 vapor and polystyrene spectrum. Then the known points were plotted on a graph of drum number versus wavelength and a smooth curve drawn through them. The calibration curve was accurate to within 0.05 microns over most of the range.

ZnSb, CdSb, and their alloys by virtue of their symmetry have refractive index tensors in the crystal axis coordinate system of the form

$$n = \begin{pmatrix} n_a & 0 & 0 \\ 0 & n_b & 0 \\ 0 & 0 & n_c \end{pmatrix}. \tag{3.1}$$

As discussed in Appendix 2, for radiation linearly polarized with its electric field along a crystallographic axis i the material acts as a normal optical medium of refractive index n_i.

One method which can be used to determine refractive indices is to observe the transmission of radiation through a sample thin enough for interference effects to occur. The samples will have absorption coefficients of the order of 2 or 3 cm^{-1} in the wavelength range 3 to 15 microns. On the thin interference samples, 30 to 50 μ thick, this absorption will be small and may be neglected. As discussed by T. Moss,[3] the transmitted intensity neglecting absorption through a sample of thickness d and refractive index n_i is

$$T = \frac{(1 - R_s)^2}{1 - 2 R_s \cos 2\delta + R_s^2} \tag{3.2}$$

where $R_s = (n_i - 1)^2/(n_i + 1)^2$ is the reflectance of a semi-infinite slab of material and $\delta = (2\pi/\lambda)n_i d$ is the phase change

per traversal of the sample at normal incidence. In the expression for δ, λ is the wavelength of the radiation in free space. From Eq. (3.2) the value of the transmission will oscillate with wavelength and will have maxima when $2n_i d = N\lambda$ where N is any integer and minima when $4n_i d = (2N + 1)$. This will be true so long as R_s is not too wavelength dependent. Then from the observation of transmission maxima the refractive index n_i can be determined as a function of wavelength if the order N of each maximum is known.

Additional information on the refractive indices can be obtained by observing transmission between crossed polarizers. This phenomena has been discussed by Sommerfeld.[9] Consider the sample and polarizers in the configuration shown in Figure 3.3. The sample plane contains the principal axes 1 and 2 of the sample. The polarizer in front of the sample is aligned to polarize radiation at 45^o to the principal axes while the polarizer behind the sample is aligned 90^o from the first polarizer. Radiation from the first polarizer excites both crystal optical oscillation modes 1 and 2 with equal amplitude aside from the small difference due to the different refractive indices. However, after traversing the sample the two modes will have approximately the same amplitude but different phases. The phase difference between the modes will be given by

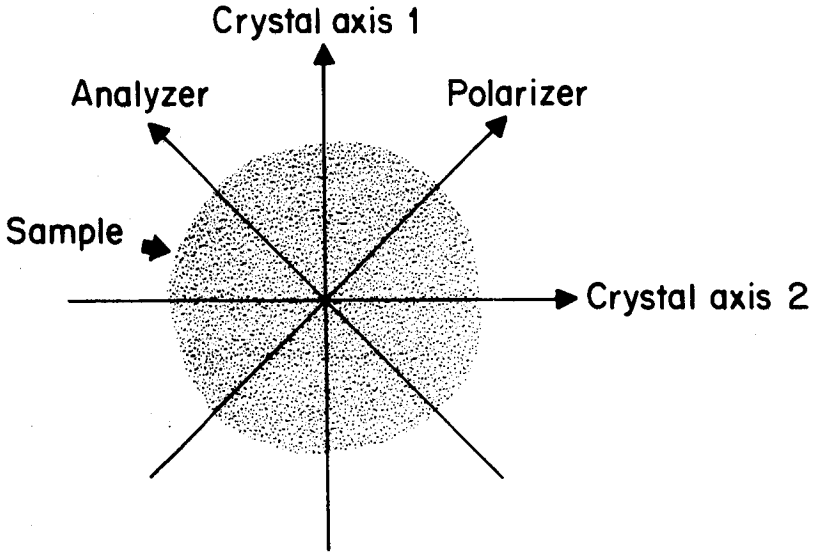

Figure 3.3. Arrangement for observing interference between crossed polarizers.

$$\Delta = \frac{2\pi}{\lambda} (n_2 - n_1)d. \tag{3.3}$$

The electric field components incident on the analyzer may be represented by

$$\begin{aligned} E_1 &= E_o \exp (2\pi i n_1 d/\lambda) \\ E_2 &= E_o e^{i\Delta} \exp (2\pi i n_1 d/\lambda) \end{aligned} \tag{3.4}$$

where E_o is a plane wave traveling in the desired direction in free space. The amplitude of the resultant field transmitted by the analyzer is

$$E_t = A \left| 1 - e^{i\Delta} \right| = 2A \sin \frac{\Delta}{2} \tag{3.5}$$

where A is a constant independent of wavelength. Thus the transmitted intensity will be proportional to $\sin^2 \Delta/2$. Transmission maxima will occur for $(n_2 - n_1) = (2M + 1)\lambda/2d$ for M an integer and transmission minima will occur for $(n_1 - n_2) = M\lambda/d$. From the observation of this behavior the difference between two refractive indices as a function of wavelength can be obtained if M the order of the extrema is known. As the anisotropies in the refractive indices are certainly much less than the refractive indices, actually about 5 or 10%, this phenomena will have the order M of the interference a factor of 10 or 20 lower than N the order of the parallel polarizer

interference on the same sample.

The refractive indices of ZnSb and CdSb were measured in the following way. For each axis, the transmission of a sample thin enough to show interference effects was obtained with the polarizers aligned along the axis. This was done by recording the thermocouple response as a function of wavelength with the sample in place and then dividing the resulting response by the thermocouple response with the sample removed. For these experiments only relative transmission is needed so that the absolute transmission was not obtained. The wavelengths of the transmission maxima for each axis and the sample thickness were recorded. From the data of others,[4,5] the refractive indices of both materials are known to be between 4 and 5. Since the samples were between 28 and 50 microns thick, the lowest order fringe observed in the wavelength range 3 to 15 microns was $N = 15$ or 16. Thus since the first maxima for which $N = 1$ was not observed, the value of N for each fringe was not known.

The difficulty of finding the refractive index without knowing N was resolved in the following way. From the known range of the refractive indices, several reasonable values for N of the longest wavelength maxima observed were calculated. Once the lowest order fringe is labelled, the N's for all the fringes are obtained by requiring adjacent fringes to have

consecutive N's. Then with these guesses for the fringe orders the resulting $n_i(\lambda)$ was calculated from the experimental fringe pattern of the sample. This gave a set of possible curves for each axis showing n_i as a function of λ. The next problem was to determine which was the correct curve. This was accomplished by obtaining $(n_i - n_j)$ for pairs of axes as a function of wavelength and matching this with the superposed sets of trial curves. The correct curve of refractive index versus wavelength for each axis was chosen by a best fit criteria. The $(n_i - n_j)$ as a function of λ were obtained from sample transmission between crossed polarizers. In the crossed polarizer experiments it was possible to observe the lower order extrema with the available sample thicknesses because of the factor of 10 to 20 reduction in interference order from the order of the parallel polarizer interference. The procedure for determining the n_i's will be clarified further in Section 4.1 where the actual data will be presented.

3.3 Determination of Absorption Coefficients

The optical absorption tensor for ZnSb, CdSb, and $Zn_xCd_{1-x}Sb$, like the refractive index tensor, is a diagonal tensor in the principal axis coordinate system. As discussed in Appendix 2, for radiation linearly polarized along axis i the material behaves as a normal optical medium of refractive index n_i and

absorption coefficient α_i. For these measurements thick samples, 1 to 4 mm, were used so that the absorption was large enough to be detectable. The absorption then eliminates the interference effects contained in Eq. (3.2) of the previous section. The usual expression for transmission through an absorbing slab, as discussed by Moss,[3] can be used to relate T and α. In this case, letting T_i represent the transmission for radiation linearly polarized along axis i, the relation is

$$T_i = \frac{(1 - R_s)^2 \, e^{-\alpha_i d}}{1 - R_s^2 \, e^{-2\alpha_i d}} . \tag{3.6}$$

By the use of Eq. (3.6) the absorption coefficients can be determined from experimental transmission data. However, knowledge of the refractive index is necessary to specify R_s.

The experimental transmission versus wavelength curves were obtained in the following way. Using the optical system described in Eq. (3.2) with both polarizers aligned along a crystal axis, the response of the thermocouple with the sample in position was recorded. Then the response of the thermocouple with an open aperture, the size of the aperture on the crystal mount, replacing the sample was recorded. The entire spectrum from 3 to 15 microns was scanned in three intervals chosen to best display the thermocouple response. For both the sample

response and the source response, the duration of the wavelength interval and the spectrometer slit width were identical. The amplifier gain was not held constant but adjusted to allow the signal to range over the whole chart width. When the sample response is divided by the source response at any wavelength the relative transmission is obtained. The wavelength intervals chosen overlapped enough to enable a single relative transmission curve to be obtained over the whole wavelength range.

The absolute transmission curve can be determined from the relative transmission curve by multiplying by a suitable constant. The correct constant was obtained by determining the absolute transmission of the sample at one wavelength. To obtain the absolute transmission, the aligned sample and the open aperture of equal area to the sample aperture are alternately inserted in the optical system having its drum position and amplifier gain fixed. Now when the sample response is divided by the source response the absolute transmission at a particular wavelength is obtained and may be used to normalize the entire transmission curve. This normalization procedure was checked at several points and found to be accurate.

A computer program was written to facilitate the calculation of α_i from the experimental T_i using Eq. (3.6). Using the computer α_i was calculated for the entire wavelength range at

intervals of 10 or 20 units of drum rotation. In the wavelength range of 3 to 15 microns, α_i was usually calculated at from 60 to 120 points.

Errors in the optical measurements resulted from signal noise, incorrect polarizer-sample alignment, incomplete polarization, and the off normal incidence of part of the beam. Signal noise was variable depending on the sample thickness, absorption strength, and wavelength region due to the spectral emission of the globar source. Without exception, the noise increased with wavelength. The polarizers could be aligned with the sample axes to within $\pm$ 2 degrees. The unwanted to wanted radiation intensity ratios for two aligned polarizers is 0.36:100. The input beam was convergent with a 5^{o} angle between envelope and center. The high refractive index of the material acts to make the beam quite parallel, approximately 1^{o} deviation, in the sample. This should make any birefringent effects quite small. The net effect of these errors on the experimental measurements will be discussed when the optical data is presented.

3.4 Determination of Conductivity and Hall Effect

The measurement of electrical conductivity and Hall effect were made on oriented samples prepared as described in section 2.5. The samples were mounted on a sample holder designed by

J. Blair[6] to facilitate isothermal transport measurements. The actual electrical measurements were made at 25 to 30 cps rather than d.c. to avoid thermoelectric effects which are quite large in these semiconductors.

A Hewlett-Packard model 400D vacuum tube voltmeter was calibrated and used for the electrical measurements. A Hewlett-Packard 200 CD wide range oscillator was used with a current limiting resistor as a current source. The sample current was obtained by measuring the voltage drop across a 100 ohm precision resistor in series with the sample's current leads. The transverse or Hall voltage and the longitudinal voltage were measured with the meter directly. The low carrier concentration of the measurement samples made the Hall voltage large enough to measure accurately without suppressing the voltage difference due to contact misalignment. In the actual measurements, the voltage was measured for the magnetic field first one way and then rotated 180°. The difference of the two voltage measurements is twice the Hall voltage. Although the meter used has an accuracy of 2% of full scale, the accuracy was greatly increased by taking a set of measurements at various current levels and choosing the best linear fit as the experimental value. This practice made the electrical measurements accurate to $\pm$ 1%.

The magnetic field was produced by a 6 inch Varian magnet

with a 3/4" gap between the pole faces. The field strength was measured with a Rawson fluxmeter having an accuracy of $\pm$ 1%.

The actual accuracy of the conductivity and Hall coefficient determinations are determined by a factor other than the instrumentation and sample dimension accuracy. The hole concentration of ZnSb, CdSb, and their alloys is irreversibly increased when the samples are heated to more than 100°C.[7,8] This is presumably due to the creation of electrically active interstitial defects which anneal out with time constants on the order of months. Thus putting electrical contacts on a sample with a soldering iron changes the carrier concentration slightly. In light of this, a measure of the accuracy of the measurements is given by the scatter in the experimental values obtained from samples cut from the same or adjacent slices.

REFERENCES

1. Y. Keloglu and A. Fedorko, Russ. Journ. of Inorganic Chem., 9, 1036 (1964).

2. K. Toman, Phys. and Chem. Solids, 11, 342 (1959).

3. T. S. Moss, Optical Properties of Semiconductors, p. 12, Butterworth, London (1959).

4. M. Zavetova, Czech. Journ. Physics, B 14, 271 (1964).

5. H. Komiya, K. Masumoto, and H. Fan, Phys. Rev., 133, A1679, (1964).

6. J. Blair, "An Investigation into the Thermal and Electrical Properties of the HgTe-CdTe Semiconductor Solid Solution System", M.I.T. Electronics Systems Laboratory Scientifie Report No. 2, Contract No. AF 19(604)-4153, June 15, 1960.

7. P. Shaver and J. Blair, Phys. Rev., 141, 649 (1966).

8. I. Andronik and M. Kot, Izv. Akad. Nauk. SSSR Ser. Fiz., 28, 1028 (1964).

9. A. Sommerfeld, "Optics; Lectures on Theoretical Physics, Vol. IV", p. 173, Academic Press, New York (1964).

CHAPTER IV. MEASUREMENTS ON ZnSb AND CdSb

4.1 Refractive Indices

The refractive indices for ZnSb and CdSb must be obtained so that later transmission data can be converted to absorption coefficient data. Existing literature contains a single determination of the refractive indices for each. For CdSb, M. Zavetova[1] has determined the refractive indices near the absorption edge only. For ZnSb, Komiya, Masumoto, and Fan[2] have measured the refractive indices from the absorption edge to a wavelength of 25 μ. As a result of incomplete data on CdSb and only a single determination for ZnSb, it was decided to measure the n_i's for both materials in the wavelength range of 3 to 15 μ.

As explained in Section 3.2, there are two interference phenomena which can be used to yield information on the refractive indices. The first concerns the oscillations in transmission with wavelength of radiation linearly polarized along a crystal axis. The second concerns the oscillations in transmission with wavelength of a configuration consisting of two crossed polarizers with the sample between them as shown in Figure 3.3. The first interference phenomena involves a single n_i only, while the second involves the anisotropy of the refractive indices or $\left|n_i - n_j\right|$.

The determination of the refractive indices of CdSb will be presented in detail. Samples of CdSb containing the a-b axes and a-c axes were cut, lapped, and polished to the smallest thickness that was practical to fabricate and handle. This thickness usually turned out to be 25 to 40 microns. The transmission of these samples in the wavelength range of 3 to 15 microns was observed with radiation polarized along each crystal axis. If sharp oscillations in transmission occurred the parallelism obtained in fabrication was adequate. If the oscillations did not occur, subsequent measurements showed the taper in sample thickness to be excessive. The maximum taper in thickness for which fringes could be seen was 3.0 μ in one cm for a 30 μ thick slice. The yield of samples which had sufficient parallelism to observe fringes was 1 in 3.

The wavelength positions of the transmission maxima are recorded for each sample axis. As discussed in Section 3.2, the transmission maxima for each axis satisfy the relation $2 n_i d = N\lambda$, where N is an integer. From the data on the refractive indices on both materials contained in references 1 and 2, the refractive indices are known to lie in range $4.0 < n_i < 5.0$. With the sample thicknesses used, the first maximum for which $N = 1$ did not fall at an observable wavelength. Therefore the orders of the maxima, the value of N for each, is uncertain. From the knowledge of the range of n_i, a set of probable values

of N_o for the longest wavelength maximum that was clearly discernible can be obtained.

If the order of one maximum is assigned as N_o, then the order of the adjacent shorter wavelength maximum is $N_o + 1$ unless the refractive index is a violent function of wavelength. The refractive indices are not expected to be fast varying functions of wavelength in this region. Thus each value of N_o assigned to the longest wavelength maximum assigns an order to each maximum in the set. Then using the relation $2n_i d = N\lambda$, the wavelength positions and the orders of the maxima can be used to calculate N_i versus λ for each assignment of N_o. In this way several curves for n_i versus λ are obtained for each axis. One set of values of n_i versus λ is the correct one for each axis. The problem is to uniquely identify the proper curve.

The actual values obtained for CdSb will be given here. For a 32.5 μ thick sample cut perpendicular to the c axis and containing the a and b axes, transmission fringes were observed for radiation linearly polarized along the a and b axes. The longest wavelength maxima that could easily be detected over the noise occurred around 13 μ. A sharply defined set of maxima was obtained down to about 9 μ where the maxima were too close for proper identification. Each axis yielded a set of 10 maxima in the wavelength range from 9 to 13 μ. The wavelength positions

of the maxima were recorded and several trial solutions calculated as discussed above. The variation of n_i with λ turned out to be linear with respect to λ for all of the assigned orders. For n_a, six possible curves of n_a versus λ were obtained, while for n_b, seven possible curves of n_b versus λ were obtained. The equations describing the behavior of each trial solution (all varied linearly with λ) are given in Table 4.1. The various experimental solutions are denoted by A-1, A-2, etc., for identification purposes.

For a sample of CdSb 29.5 μ thick and cut perpendicular to the b axis, containing the a and c axes, transmission fringes were obtained with radiation polarized along each axis. The trial solutions were obtained in a similar manner and again all the solutions were linear with respect to λ. For this sample n_a had 6 possible solutions while n_c had 6 possible solutions also. The equation for each solution is given in Table 4.2.

Now the problem remains to determine which solution is the correct n_i versus λ curve. By observing the transmission of the sample between crossed polarizers, information on the difference in refractive indices can be obtained which will then aid in selecting the correct curves. As discussed in Section 3.2, the maxima of transmission in the case of crossed polarizers will occur for $|n_i - n_j| = (2M + 1)\lambda/2d$ and minima will occur for $|n_i - n_j| = M\lambda/2\,d$. In each case M can be zero or any positive integer. For the case of transmission of radiation

n_a for CdSb

Trial Solution	Equation for Solution
A-1	$n_a = 4.665 + (0.017 \pm 0.001)\ \lambda$
A-2	$n_a = 4.700 \pm 0.001\ \lambda$
A-3	$n_a = 4.700 - (0.015 \pm 0.001)\ \lambda$
A-4	$n_a = 4.785 - (0.038 \pm 0.001)\ \lambda$
A-5	$n_a = 4.765 - (0.052 \pm 0.001)\ \lambda$
A-6	$n_a = 4.850 - (0.086 \pm 0.001)\ \lambda$

n_b for CdSb

Trial Solution	Equation for Solution
B-1	$n_b = 4.405 + (0.051 \pm 0.001)\ \lambda$
B-2	$n_b = 4.420 + (0.034 \pm 0.001)\ \lambda$
B-3	$n_b = 4.405 + (0.022 \pm 0.001)\ \lambda$
B-4	$n_b = 4.460 \pm 0.001\ \lambda$
B-5	$n_b = 4.465 - (0.015 \pm 0.001)\ \lambda$
B-6	$n_b = 4.465 - (0.031 \pm 0.001)\ \lambda$
B-7	$n_b = 4.465 - (0.046 \pm 0.001)\ \lambda$

Table 4.1. Equations describing the trial solutions of n_a and n_b versus λ for CdSb from data obtained from a 32.5 μ thick sample.

n_a for CdSb

Trial Solution	Equation for Solution
A'-1	$n_a = 4.735 + (0.014 \pm 0.001)\ \lambda$
A'-2	$n_a = 4.705 \pm 0.001\ \lambda$
A'-3	$n_a = 4.755 - (0.022 \pm 0.001)\ \lambda$
A'-4	$n_a = 4.745 - (0.038 \pm 0.001)\ \lambda$
A'-5	$n_a = 4.820 - (0.062 \pm 0.001)\ \lambda$
A'-6	$n_a = 4.800 - (0.077 \pm 0.001)\ \lambda$

n_c for CdSb

Trial Solution	Equation for Solution
C-1	$n_c = 4.485 + (0.041 \pm 0.001)\ \lambda$
C-2	$n_c = 4.520 + (0.021 \pm 0.001)\ \lambda$
C-3	$n_c = 4.560 \pm 0.001\ \lambda$
C-4	$n_c = 4.505 - (0.012 \pm 0.001)\ \lambda$
C-5	$n_c = 4.535 - (0.031 \pm 0.001)\ \lambda$
C-6	$n_c = 4.560 - (0.041 \pm 0.001)\ \lambda$

Table 4.2. Equations describing the trial solutions of n_a and n_c versus λ for CdSb from data obtained from a 29.5 μ thick sample.

polarized parallel to a crystal axis (i.e., the polarizers both aligned along the same crystal axis) the order of the maxima was given by $N = 2n_i d/\lambda$. Now for the case of crossed polarizers the order of the minima is given by $M = 2|n_i - n_j| d/\lambda$. The minima rather than the maxima is used for convenience in comparing the expressions. Since the anisotropies in refractive index are of the order of 5 or 10%, there is a factor of 10 or 20 reduction in the order of the interference observed. Thus on the same sample where a 15^{th} or 20^{th} order maxima was observed at long wavelengths with parallel polarizers, a first order maxima or minima will be observed with crossed polarizers in the same wavelength range. In many cases it was necessary to make thicker samples, 50 or 75 μ, to observe interference phenomena in the longer wavelength region. For the crossed polarizer interference the order of the extrema could be unambiguously identified by the movement of the interference effects with changes in thickness. Many samples were available for these measurements since the rejects from the parallel interference measurements, those with insufficient parallelism, were perfectly good for this experiment.

For the a-b plane of CdSb the transmission of many samples between crossed polarizers was observed. Analysis of the data showed $|n_a - n_b|$ to be essentially constant at the value 0.250 $\pm$ .010 over the wavelength range of 3 to 15 microns. In order

for the experimental data to fit this criteria the slopes of the variation of n_a and n_b with λ must agree to within 0.001. From Table 4.1 there are two pairs of trial solutions which fit the slope matching criteria namely A-2 with B-4 having essentially zero slope and A-3 with B-5 having - 0.015 slope. For all other pairs of trial solutions the slopes, with experimental error considered, differ by more than 0.001. The pair A-2 with B-4 has a value of $(n_a - n_b)$ of 0.24 while the pair A-3 with B-5 has a value of $(n_a - n_b)$ of 0.235. The data does not enable the unique determination of the correct n_i curves but narrows the choice to two possible curves for each axis.

In a similar manner, samples of CdSb cut to contain the a-c plane were examined with crossed polarizers. The observed interference effects showed $|n_a - n_c|$ to be essentially constant from 3 to 14 μ in wavelength at a value of 0.150 ± 0.020. To exhibit this behavior the slopes of the n_a and n_c versus λ solutions must agree to within 0.002. Examination of Table 4.2 shows that only two pairs of lines satisfy this criteria and they are A'-2 with C-3 and A'-4 with C-6. For A'-2 with C-3, $|n_a - n_c| = 0.145$ while for A'-4 with C-6, $|n_a - n_c| = 0.175$. Again the data on $|n_a - n_c|$ has lead to two possible solutions rather than a unique one.

However, the value of n_a should not depend on which plane the a-b or the a-c is used for the measurement. For the a-b

plane the following acceptable solutions for n_a were obtained

A-2 $\quad n_a = 4.700 \pm 0.001\ \lambda$

A-3 $\quad n_a = 4.700 - (0.015 \pm 0.001)\ \lambda.$

For the a-c plane the following acceptable solutions for n_a were obtained

A'-2 $\quad n_a = 4.705 \pm 0.001\ \lambda$

A'-4 $\quad n_a = 4.785 - (0.038 \pm 0.001)\ \lambda.$

Forcing n_a from both determinations to be equal allows the identification of A-2 or A'-2 as the correct value for n_a. This in turn identifies B-4 and C-3 as the correct solutions for n_b and n_c. The closeness of n_a from A-2 and A'-2 increases the confidence in the accuracy of the measurements.

The obtained refractive indices for CdSb are essentially independent of wavelength between 3 and 15 microns. To an accuracy of $\pm$ 1% the values are $n_a = 4.70$, $n_b = 4.46$, and $n_c = 4.56$. M. Zavetova[1] who has determined the refractive indices in the neighborhood of the absorption edge has obtained at 3 microns wavelength the values $n_a = 4.78$, $n_b = 4.57$, and $n_c = 4.50$. These results would be in quite close agreement with those obtained here if axes b and c were interchanged. The orientation of all samples used to determine the n_i's for CdSb was checked and no errors were found.

The refractive indices of ZnSb were found by the use of the

same two interference phenomena. First transmission fringes were obtained for the b and c axes for radiation polarized parallel to each axis using a 53 μ thick sample. For each axis about 27 maxima were observed in the wavelength range of 7.5 to 13 μ. The reason so many extrema were discernible was due to the high parallelism of the sample. The peaks were very high and sharp and could be isolated even when closely spaced for λ of 9 μ or less. From this data, nine trial solutions were obtained for both n_b and n_c versus λ. Using data, from this sample and other b-c samples, obtained with crossed polarizers, information on $|n_b - n_c|$ was obtained which enabled n_b and n_c to be determined uniquely from the trial curves. The solutions identified as the correct ones are

$$n_b = 4.22 + (0.003 \pm 0.0005)\ \lambda$$

$$n_c = 4.31 - (0.0005 \pm 0.0005)\ \lambda.$$

Both n_b and n_c are very close to being independent of λ and may be taken as such for all practical purposes.

On a 70.5 μ thick sample that also had very high parallelism and was cut to contain the a and b axes, transmission fringes were obtained for radiation polarized along the a axis. This sample had the highest parallelism that was attained in the course of these experiments. The taper in its thickness was about 1 micron per cm. The fringes were sharp and of a high quality.

This tends to show that parallelism is a more important parameter than small thickness in obtaining transmission fringes for radiation polarized parallel to an axis. From the observed maxima, eleven trial solutions of n_a versus λ were obtained. The correct solution was obtained by comparing the trial solutions to the known solutions for n_b and n_c with data on $|n_a - n_b|$ and $|n_a - n_c|$. The information on $|n_a - n_b|$ and $|n_a - n_c|$ was obtained from a-b and a-c samples respectively and enabled the correct solution for n_a to be determined uniquely. The value of n_a obtained was $n_a = 4.50 + (0.001 \pm 0.0005)\ \lambda$.

For ZnSb the experimental values of n_i are essentially independent of wavelength and to an accuracy of $\pm$ 1% are given by $n_a = 4.51$, $n_b = 4.25$, and $n_c = 4.30$. Komiya, Masumoto, and Fan[2] have measured the refractive index of ZnSb and find the values to be $n_a = 5.11$, $n_b = 4.58$, and $n_c = 4.65$ at a wavelength of 10 microns. Their data shows a slight linear variation of the n_i's with wavelength between 4 to 25 microns. Although their results disagree numerically with those obtained here, it is interesting to note the size order is the same for both, that is, $n_a > n_c > n_b$.

The refractive indices reported by Komiya, Masumoto, and Fan[2] are about 10% higher than those obtained in this work. They obtained their data by the observation of interference effects on thin samples with radiation polarized along each axis. They

do not give the thickness of their samples or how they determined the order of each fringe. From their data, their samples would have had to be 2 μ thick for the first maxima they observed to be the first order maxima. This would be an extraordinarily thin sample to handle. The large discrepancy in their results from those reported here may be due to one of these causes. If their samples were about 2 μ thick for observation of the first order fringes, the refractive indices would be extremely sensitive to any errors in thickness measurements. The sample thickness would be very difficult to measure accurately in this range and any error could shift the refractive indices obtained severely. If they did not have samples at this low thickness, they would not have observed a first order interference and could have erred in assigning orders to the interference peaks. This also would lead to incorrect refractive indices. It is also possible that the values obtained here are in error despite careful measurements and crosschecking.

A + 10% change in a refractive index will affect the absorption coefficient calculation in the following way. For a + 10% increase in n_i, $R_s = (n_i - 1/n_i + 1)^2$ will have a 10% increase. The quantity $(1 - R_s)^2$ which enter the relation for transmission through a slab will suffer an 18% increase. Then αd will be decreased by - 0.16 for an initial n_i of 4.50. For a 2 mm thick sample α_i would be decreased by 0.80 cm^{-1}. However, the

wavelength dependence of α_i would not be affected. The increase in n_i by 10% would add a wavelength independent contribution of - 0.80 cm^{-1} to the observed absorption coefficient. To first order a linear variation of n_i with wavelength will not affect the absorption coefficient since R_s will remain essentially wavelength independent.

The effect of a + 10% error in the refractive index on the experimental results will be the following. The magnitude of α_i the absorption coefficient will be affected by a wavelength independent contribution of - 0.16/d cm^{-1}. The slope of α_i versus λ^2 will not be altered by this error. However, the effective mass which is determined directly from α_i, σ_i, and R will be altered. This results from the dependence of α_i on n_i and m_i^* in the expression for free carrier absorption discussed in Appendix 2. A 10% increase in n_i will cause a 10% increase in $(1/m_i^*)^2$ or a 5% decrease in m_i^*. If such an error were present in the refractive indices used, a systematic variation would be observed in the wavelength independent portion of the absorption coefficient. For the absorption coefficient of an axis measured on various thickness samples, the wavelength independent portion of the absorption coefficient would fluctuate by an amount $+ 0.16 \left(\frac{1}{d_1} - \frac{1}{d_2}\right)$ cm^{-1} where d_1 and d_2 are the sample thicknesses. Such a variation was not observed in the experimental data. The background absorption varied randomly rather than systematically.

4.2 Optical Absorption

The absorption spectrum of each axis of both CdSb and ZnSb was examined to determine whether or not there is any free carrier absorption. If found, the free carrier absorption could be used quantitatively to help determine the effective masses of the valence band. The optical absorption tensor is diagonal in the crystal axes coordinate system. The components of the absorption tensor may be examined individually by utilizing radiation linearly polarized along each crystal axis. This is discussed in detail in Appendix 2. In order to obtain information on α_i, the absorption coefficient for the i^{th} axis, it is only necessary to use radiation linearly polarized to have its electric vector along axis i.

The procedure used to obtain the absorption coefficients has been described in detail in Section 3.3. Basically the procedure consists of obtaining the absolute transmission of the sample versus wavelength. This is obtained by recording the thermocouple response with and without the sample present in the optical path and then dividing the two responses. The absorption coefficients can then be obtained from the transmission data using Eq. (3.6) and the experimentally determined refractive indices.

The experimental data for ZnSb will be presented first. Figure 4.1 shows α_a and α_b versus wavelength as was obtained

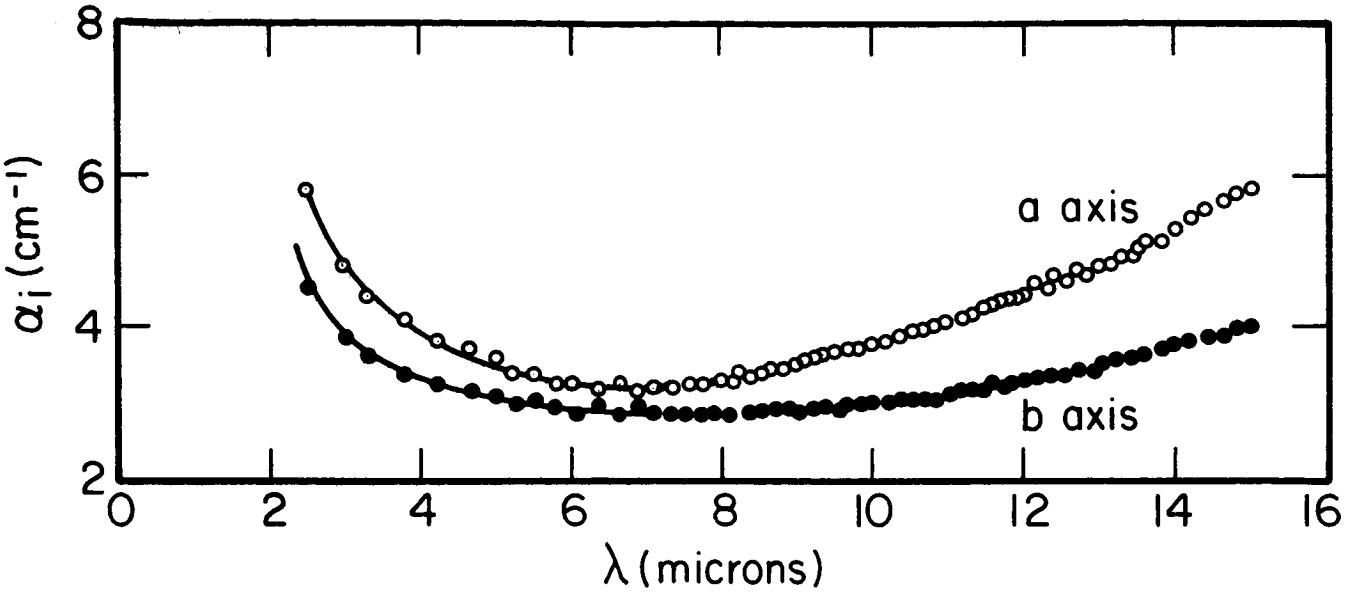

Figure 4.1. Absorption coefficient versus wavelength for ZnSb a and b axes from sample 0.0992 cm thick with p = 8.6 x 10^{16} cm^{-3}.

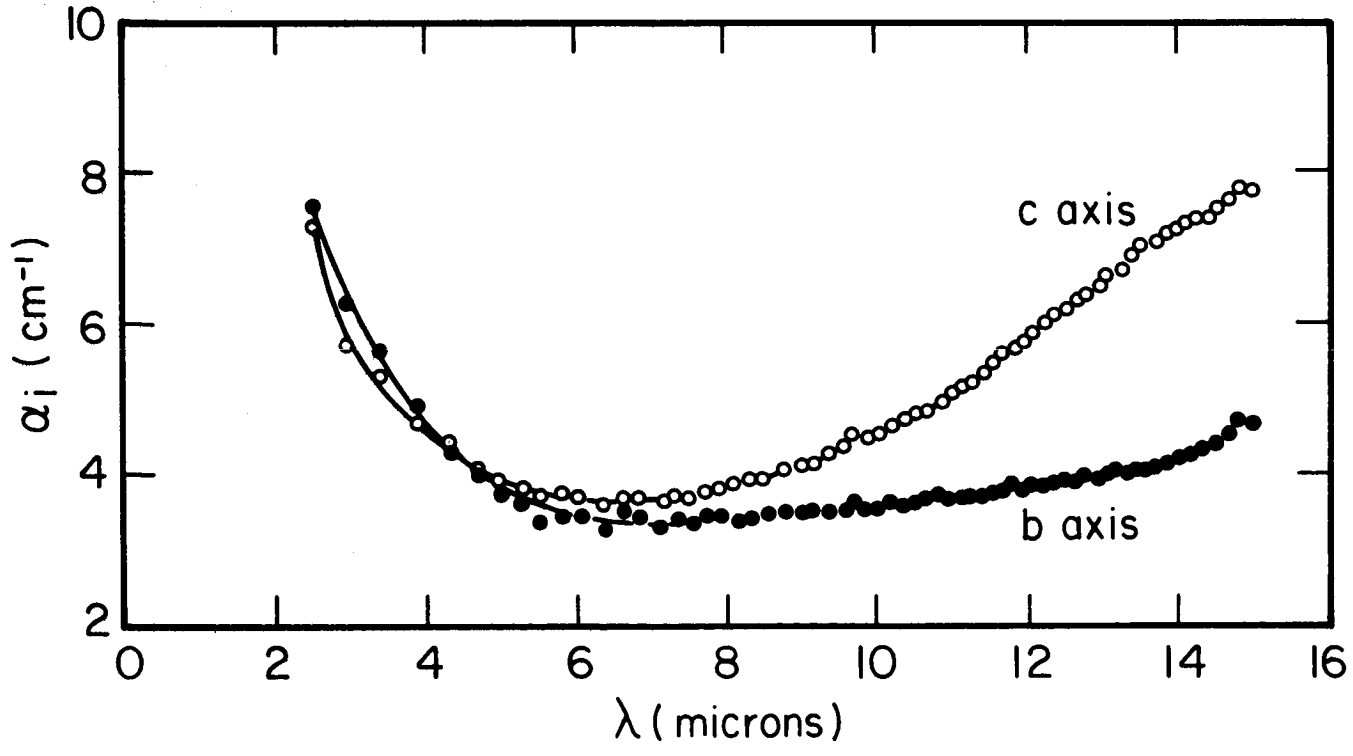

Figure 4.2. Absorption coefficient versus wavelength for ZnSb b and c axes from sample 0.108 cm thick with p = 9.2 x 10^{16} cm^{-3}.

from a ZnSb sample that was 0.0992 cm thick with a hole concentration p = 8.6 x 10^{16} cm^3. In order to have all three absorption coefficients displayed, Figure 4.2 shows α_b and α_c versus λ obtained from a ZnSb sample 0.108 cm thick with p = 9.2 x 10^{16} cm^{-3}. The a-b plane sample was cut from ingot x-1041 while the b-c plane sample was cut from ingot x-1040.

The absorption edge is indirect and as a result not very steep. The structure of the absorption edge and some impurity absorption extend out to about 6 μ microns. The accuracy of the absorption coefficient is not very good for wavelengths less than 6 μ. This is caused by the long air path of the optical system and the water vapor absorption bands in the atmosphere combining to make the thermocouple response highly sensitive to room conditions. The wavelength range between 14 and 15 μ was also a region of low accuracy because the source intensity was very low in that range. This resulted in a very poor signal to noise ratio in this region.

The two independent determinations of α_b from Figure 4.1 and 4.2 agree quite well. The major discrepancies lie in the region of low accuracy of the optical system. The two curves differ slightly in the detailed behavior of α_b for λ less than 6 μ. Also in the data from the b-c plane of ZnSb there is an increase of α_b for λ between 14 and 15 μ which does not appear on the data from the a-b plane.

To analyze the absorption data further it is desirable to plot α_i versus λ^2. Figures 4.3 and 4.4 shows the absorption coefficient data from Figures 4.1 and 4.2, respectively, plotted versus λ^2. The data in all cases fits a straight line very well for λ greater than 7 microns. For λ less than 7 microns the influence of impurity absorption and the absorption edge dominates over any λ^2 dependence which may be there. The slope of the lines appear to be proportional to carrier concentration as the slope ratio of the two independent determinations of α_b are in the ratio of the hole concentrations of their respective samples.

For the determination of the slope of the α_i versus λ^2 lines, fifty or more experimental points were available in the range $50 < \lambda^2 < 220\ \mu$. The confidence in the slope determination depended on the extent of scatter present in the set of data. The regions where large scatter was obtained were rechecked several times in order to obtain better data. Also the α_i's were each measured on various thickness samples and checked for consistency. As an example of this, Figure 4.5 shows the absorption coefficient, α_b, versus wavelength for two samples of equal carrier concentration and different thicknesses. The carrier concentration for both was $p = 9.2 \times 10^{16}\ cm^{-3}$ and the thicknesses were 0.108 and 0.170 cm. In each case the slope of the α_i versus λ^2 curve was independent of sample thickness so long as the carrier concentrations were equal in the samples.

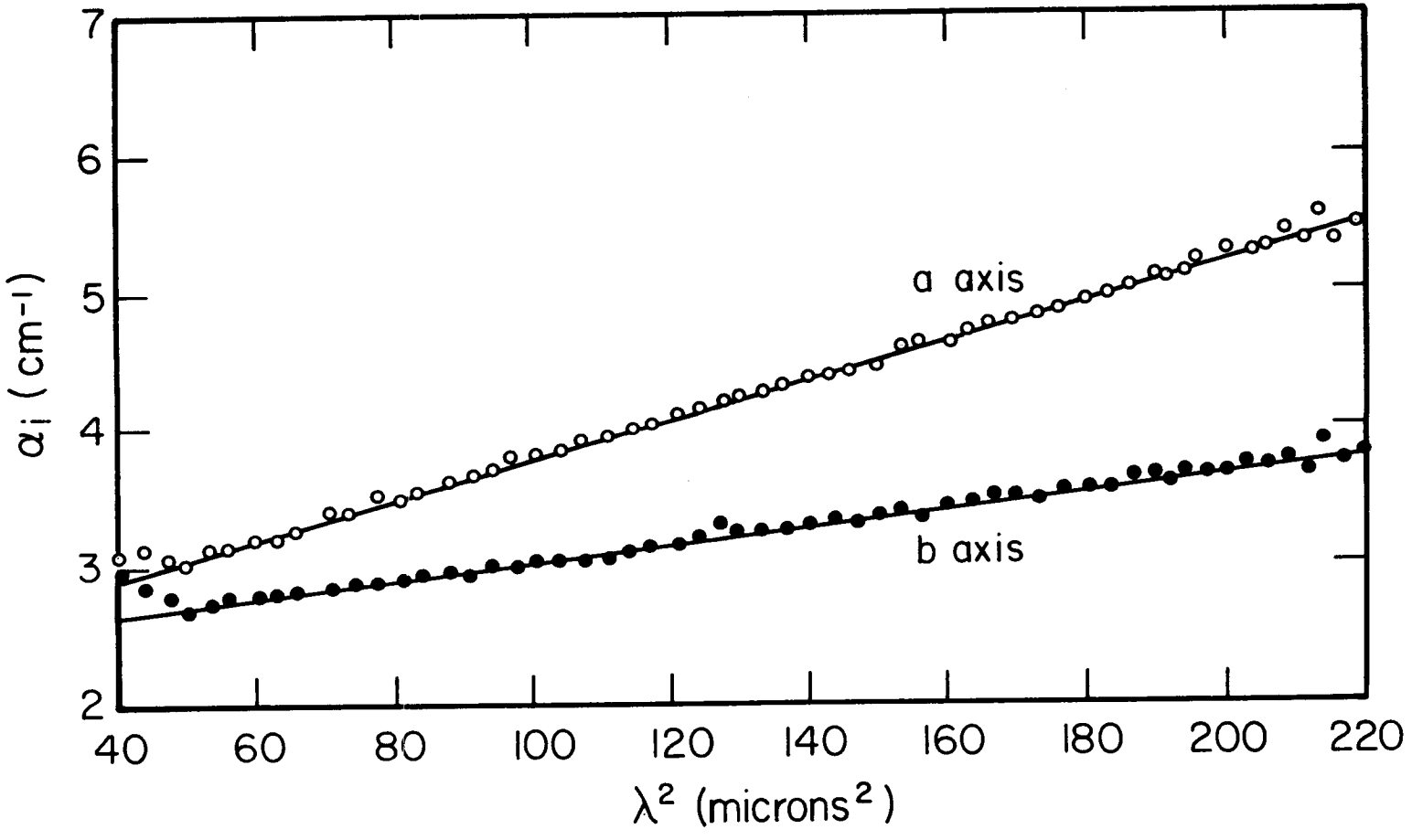

Figure 4.3. Absorption coefficient versus wavelength squared for ZnSb a and b axes from sample 0.0992 cm thick with p = 8.6 x 10^{16} cm^{-3}.

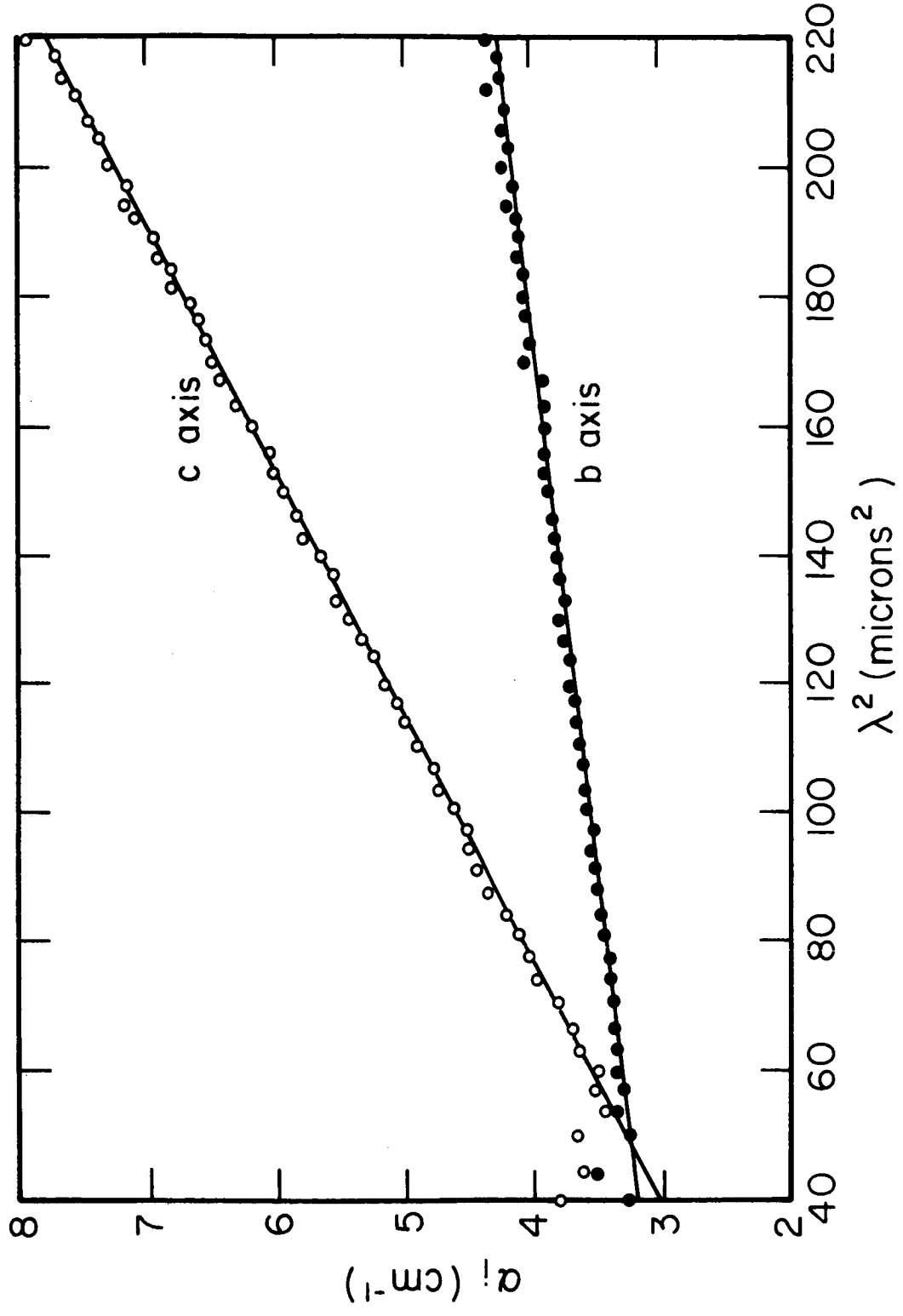

Figure 4.4. Absorption coefficient versus wavelength squared for ZnSb b and c axes from sample 0.108 cm thick with p = 9.2 x 10^{16} cm^{-3}.

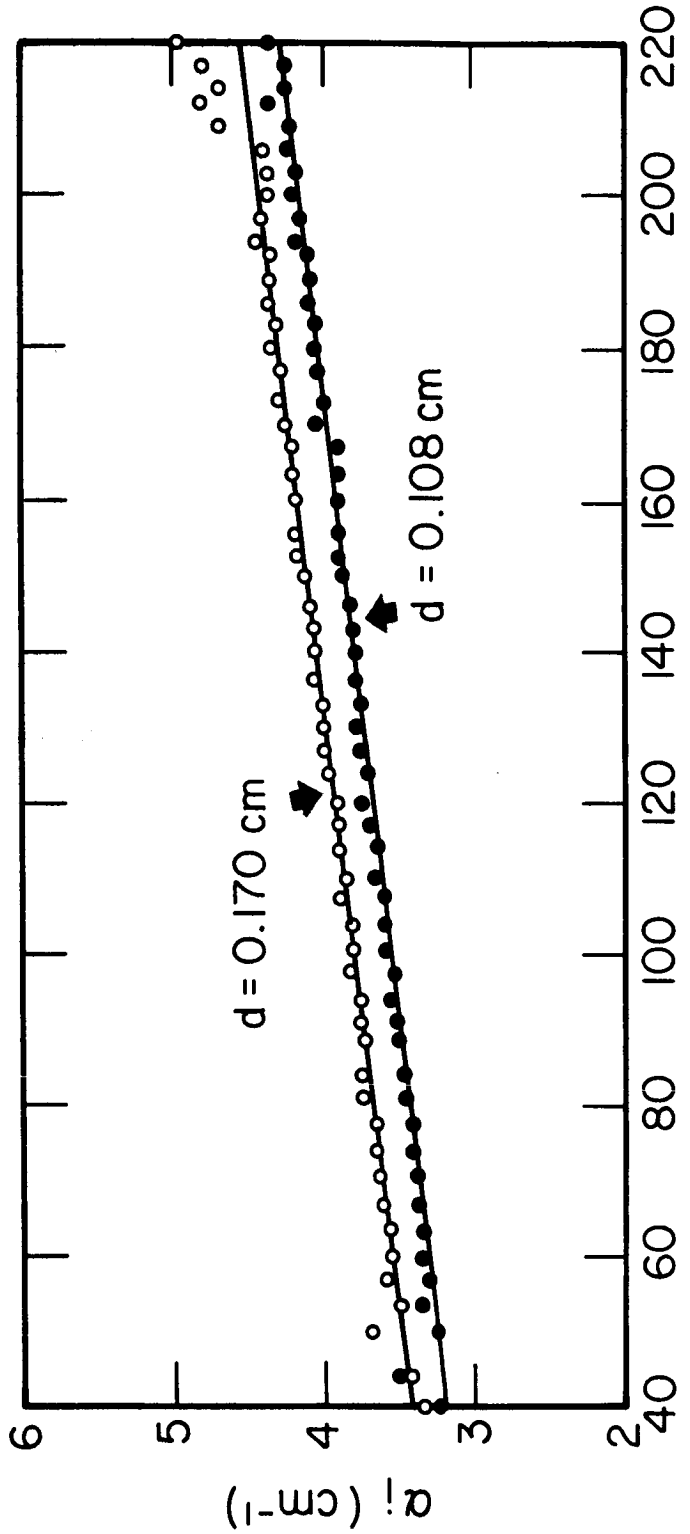

Figure 4.5. Absorption coefficient for b axis versus wavelength squared as obtained from two b-c plane samples of ingot x-1040 with the same carrier concentration but of different thicknesses.

This check on the data serves a multiple purpose. It increases the confidence in the experimental values of the refractive index used to convert the transmission data to absorption data. It confirms the validity of the use of Eq. (3.6) to convert from transmission data to absorption data. It also serves to confirm the accuracy of the experimental procedures used. The agreement of α_b versus λ^2 from two sample planes, the a-b and the b-c, confirms the accuracy of the experimental procedures also. By the reproducibility observed in the data and consideration of errors in the optical system discussed in Section 3.3, the accuracy in the absolute value of α_i for $7 < \lambda < 14\ \mu$ is $\pm$ 5% but the slope of α_i versus λ^2 can be determined to $\pm$ 2%.

To determine the dependence of the absorption on hole concentration, measurements were made on doped samples of ZnSb grown by P. Shaver.[3] The results of the absorption measurements on the a and b axes are shown in Figure 4.6 where the slope of α_i versus λ^2, that was obtained, is plotted as the ordinate while hole concentration is plotted as the abcissa. Similar data was not taken for the c axis due to lack of suitable material. For the data shown the accuracy of p is $\pm$ 5% and the accuracy of the slope determination is $\pm$ 2%. Straight lines have also been drawn through the data. The fit of the data to a straight line is quite good and indicates that the

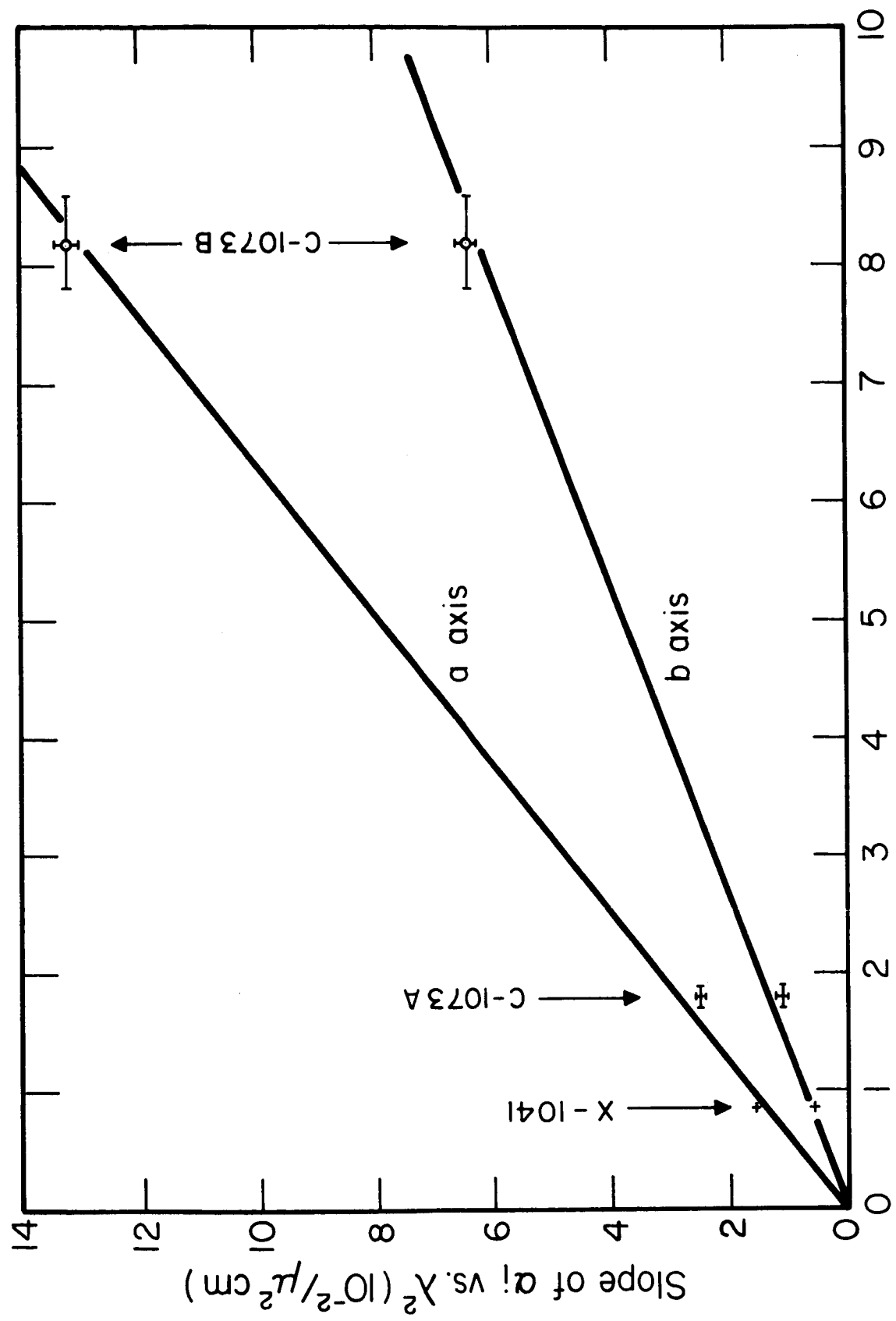

Figure 4.6. Slope of α_i versus λ^2 curves plotted versus hole concentration for ZnSb a and b axes.

slopes of the absorption versus λ^2 curves varies linearly with hole concentration.

The characteristics of the data indicate that free carrier absorption is the dominant process in the wavelength range of 7 to 15 microns. As discussed in Appendix 2, free carrier absorption for an ellipsoidal valence band maximum oriented along the crystal axes is described for each axis by

$$\alpha_i = \frac{pe^2 \lambda^2}{(2\pi)^2 n_i c^3 \varepsilon_o m_i^*} \left\langle \frac{1}{\tau_i} \right\rangle . \qquad (4.1)$$

In Eq. (4.1) e is the electronic charge, c is the speed of light, ε_o is the permittivity of free space, and m_i^* is the effective mass in the i^{th} direction. In addition, τ_i is the relaxation time in the i^{th} direction and the brackets $< >$ are defined by

$$< G > = \frac{\int_o^\infty E^{3/2} G\, e^{-E/k_B T} dE}{\int_o^\infty E^{3/2} e^{-E/k_B T} dE} . \qquad (4.2)$$

In Eq. (4.2), E is the energy of a hole in this case, k_B is Boltzmann's constant, and T is the absolute temperature. Equation (4.2) is valid for non-degenerate material which all of the grown and used material was. The linear behavior at α_i with λ^2 and p has been confirmed experimentally. From these observations the portion of the absorption data which varies linearly

with λ^2 can be attributed to free carrier absorption with a good deal of certainty. The possibility of a degenerate valence band or multiple valence bands contributing interband absorption to that observed is not discounted and will be discussed at the end of this chapter.

In addition to the free carrier contribution of the absorption coefficient there is a wavelength independent contribution present in all of the data taken in this study. While the slope of α_i versus λ^2 was quite reproducible from sample to sample, the wavelength independent portion was not. This contribution might be explained by the following two effects. First, bulk defects such as low angle grain boundaries may produce wavelength independent scattering which would appear as a radiation loss or absorption. The second and more likely cause is that the presence of the sample in the optical path slightly defocuses the thermocouple-ellipsoidal mirror subsystem in the optical system. The system was brought to a very delicate focus with the sample absent and a slight defocusing would appear as a wavelength independent light loss.

Similar absorption measurements were made on undoped p-type CdSb. The values of α_a, α_b, and α_c obtained are plotted versus λ^2 on Figure 4.7. All of the CdSb samples were cut from ingot x-1014 whose carrier concentration was $p = 3.1 \times 10^{16}$. The hole concentration was measured for each region from which

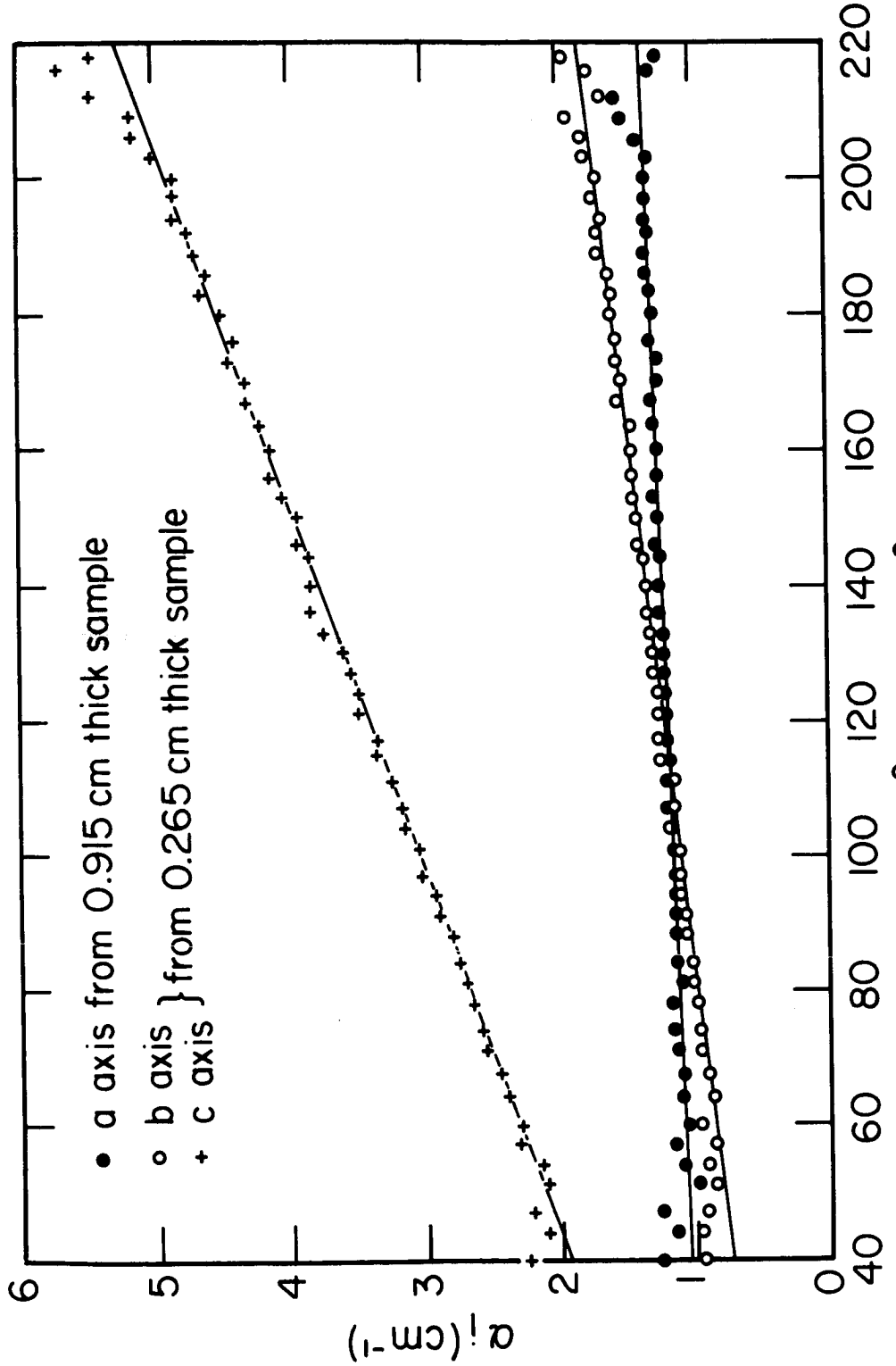

Figure 4.7. Absorption coefficients α_i's versus wavelength squared for CdSb from x-1014 with p = 3.1 x 10^{16} cm^{-3}.

samples were cut and found to be uniform over the ingot. The data for α_b and α_c shown in Figure 4.7 was obtained from a b-c plane sample 0.265 cm thick. The change in α_a with λ was very slight on the initial samples measured. In fact, an increase in α_a with λ could not be detected. The small value of α_a allowed a thick sample 0.915 cm to be used to determine the variation of α_a with λ. The data from this sample almost 1 cm thick is shown in Figure 4.7.

The absorption coefficients for CdSb follow a linear relation with λ^2 quite well in the range $7 < \lambda < 15$ μ. The slope and magnitude of the α_b data was checked in the a-b and the b-c planes and found to agree very well. In addition the data for α_a, α_b, and α_c was measured on several samples of different thickness and found to agree.

The experimental values of the free carrier absorption, the portion of the absorption coefficient varying linearly with λ^2, were obtained to an accuracy of $\pm$ 2%. For ZnSb the values obtained are $\alpha_a = 1.55\ \lambda^2 m^{-1}$ with $p = 8.6 \times 10^{16}$ cm^{-3}, $\alpha_b = 0.55\ \lambda^2 m^{-1}$ with $p = 9.2 \times 10^{16}$ cm^{-3}, and $\alpha_c = 2.75\ \lambda^2\ m^{-1}$ with $p = 9.2 \times 10^{16}$ cm^{-3}. For the values given, λ is in microns. Similarly for CdSb the values obtained are $\alpha_a = 0.20\ \lambda^2\ m^{-1}$, $\alpha_b = 0.50\ \lambda^2 m^{-1}$, and $\alpha_c = 1.95\ \lambda^2 m^{-1}$ all with $p = 3.1 \times 10^{16}$ cm^{-3} and λ in microns.

4.3 Conductivity and Hall Effect

The main purpose of the conductivity and Hall measurements is to give additional information about the optical absorption samples. Then the optical absorption, the electrical conductivity, and the Hall coefficient all pertaining to the same sample region can be used to extract information concerning the parameters of that sample region. For this reason the conductivity and Hall samples were cut from slices which, in the original ingot, sandwiched the slices used for optical absorption measurements. That is, each optical absorption sample had its adjacent slices cut into oriented electrical samples.

From symmetry considerations discussed by Shaver,[3] the electrical conductivity of both semiconductors is a diagonal tensor in the crystal axes coordinate system. While crystal symmetry and Onsager symmetry considerations allow three independent Hall coefficients, namely, R_{abc}, R_{bca}, and R_{cab}, the experimentally observed Hall coefficient was isotropic within experimental error. This is in agreement with the experimental data of others, as related in Chapter I.

In order to determine the electrical parameters of a given region, measurements were made on several electrical samples cut from the same region of material. The data was handled in the following way. The experimental value is taken as the mean of the values measured on the set of like samples. The mean of

a set of N values x_i is defined as

$$\bar{x} = \frac{\sum_i x_i}{N} .$$

The standard deviation or rms deviation of the set of N values x_i is defined as

$$D = \left[\sum_i \frac{(x_i - \bar{x})^2}{N} \right]^{1/2} .$$

In the electrical data taken, there were from six to twelve samples involved in determining each parameter. The number of samples is too small to justify any rigorous application of statistics to determine the probable error. Therefore the standard deviation of the data will be taken directly, as a measure of the probable error in the values.

In Section 3.4 mention was made of the problem of irreversible changes in hole concentration occurring when electrical contacts were soldered to the sample. This would help to account for the fact that the standard deviation or probable error in the electrical data obtained from samples cut from adjacent material was higher than the accuracy of the measurements would predict.

Random increases in hole concentration would introduce a systematic error into the electrical data. That is, the mean

conductivity would be higher than that of the unheated optical samples while the mean Hall constant would be lower. If the hole concentration was increased in the samples randomly, the standard deviation in the Hall mobility μ_H, defined as σR, should be less than the standard deviations of σ and R. The carrier concentration changes would affect both σ and R directly but would have much less effect on the individual carrier's mobility.

Some of the data showed evidence for the presence of such a systematic error. For the electrical data describing the b axis of the ZnSb a-b samples, the standard deviation of σ_b was 7%, the standard deviation of R was 9%, and that of μ_H was 5%. Here the standard deviation of μ_H is clearly less than the standard deviations of σ and R. This behavior indicative of a systematic error occurred in 1/3 of the data sets obtained.

Further evidence for a systematic error was given by the behavior of the electrical data from the b-c plane ZnSb samples. This sample had a relatively large carrier concentration. It is expected that small changes in carrier concentration which would affect the properties of samples with lower carrier concentrations would not affect the properties of this sample. The experimental data which was obtained did support this statement. The standard deviation for σ was 3%, that for R was 1%, and that for μ_H was 4%. These standard deviations or probable

errors are near those which would be expected from the measuring techniques. In fact, the standard deviation for R is lower than the value of 2% which would be predicted from the measuring techniques.

The remainder of the data was inconclusive as to the presence of a systematic error. Typical was the c-axis of CdSb, for which the standard deviation in σ was 7%, that in R was 6%, and that in μ_H was 8%. The standard deviation of μ_H is neither markedly smaller than the standard deviation in σ and R nor is it as large as the sum of the standard deviations of σ and R. Thus the error seems neither entirely correlated or entirely uncorrelated. This behavior occurred in almost 1/2 of the data taken.

For two of the sets of samples for which the standard deviation was high, the measurements were repeated a month later and the changes noted. The increased carrier concentration caused by heating would have annealed out to be at most 25% of their initial value in this time interval. This estimate is based on measurements made by Shaver[3] on carrier precipitation phenomena in undoped ZnSb. The mean of the conductivity values in each set decreased by 2% from its original value. The standard deviation of σ decreased from 7% to 6%. Similarly for R, the mean increased by 2% and the standard deviation decreased from 6% to 5%. This data shows that the systematic part of the error

is of the order of 3% of the electrical conductivity and Hall coefficient.

Thus the evidence shows some systematic error present in both σ and R for the samples from material other than the high carrier concentration ZnSb. Just how much systematic error is present and how to best correct for it is not clear. One problem is that the number of measurements involved is not enough to justify the use of statistics in their interpretation.

The effect on our results of a systematic error in the data will be investigated here. The overall objective of the experiments is to obtain the effective mass parameters and the relaxation time coefficients. Consider the effect of a + 4% error in σ_i and a - 4% error in R, i.e., a systematic 4% error in p. This represents a generous estimate of the systematic error present considering the discussion above of the shift in mean values of the data with time. The analysis shows that m_i^{*2} is directly proportional to $(R^2\alpha_i\sigma_i)^{-1}$ where α_i is the free carrier absorption relative to axis i. A systematic error of 4% in p would then cause a + 4% error in m_i^{*2} or about a + 2% error in m_i^*. For the relaxation coefficients A_i, the analysis shows A_i^2 to be proportional to (σ_i/α_i). A systematic error of + 4% in carrier concentration would then lead to an error of about + 2% in A_i. Thus the systematic error, if present, is of little significance in the ultimate use of the data, namely, the determination of

the m_i^*'s and the A_i's.

As a result of the inconclusive evidence of a systematic error, and the small effect it would have on the effective masses and relaxation time coefficients, the data will not be corrected for a systematic error. The error limits will be taken as the standard deviation of the experimental data. The standard deviation of the experimental data contains a contribution from the measurement errors, a contribution from the variation of the systematic error from its mean, and a contribution from sample inhomogenieties. The standard deviation of the conductivity data was 7% for the majority of the sets of 6 samples. The standard deviation of the Hall coefficient was 6% for the majority of the sets of 12 samples. Thus the predicted accuracy of the σ_i's will be $\pm$ 7% and that of the R's will be $\pm$ 6%. This will lead to accuracy limits on the effective masses and relaxation times which will be generous enough to enclose the small systematic error which seems to be present.

The experimental values of σ_i and R for ZnSb at room temperature, 294^{o}K, and pertaining to the optical samples for which data have previously been given are given here. For the a-b optical sample, σ_a = 3.33 (ohm-cm)$^{-1}$, σ_b = 2.25 (ohm-cm)$^{-1}$ and R = 86 (cm^3/coul). For the b-c optical sample, σ_b = 2.30 (ohm-cm)$^{-1}$, σ_c = 5.90 (ohm-cm)$^{-1}$, and R = 80 (cm^3/coul). As previously stated the conductivities and Hall coefficients have

an expected accuracy of ± 7% and ± 6%, respectively. The Hall mobilities are somewhat lower (about 30%) than those obtained by Shaver[3] on similar samples. The conductivity ratio obtained here for ZnSb of $\sigma_a:\sigma_b:\sigma_c$ = 1.55:1.00:2.56 agrees very well with that reported by Shaver of $\sigma_a:\sigma_b:\sigma_c$ = 1.50:1.00:2.50. Shaver[3] is the only one who has reported in the literature the conductivity along identified axes for ZnSb.

For CdSb, all the optical samples came from the same ingot which had transport properties uniform within experimental error. The experimental values at 294°K for the CdSb samples are σ_a = 0.60 $(\text{ohm-cm})^{-1}$, σ_b = 0.84 $(\text{ohm-cm})^{-1}$, σ_c = 0.52 $(\text{ohm-cm})^{-1}$, and R = 240 $(\text{cm}^3/\text{coul})$. The expected accuracy is ± 7% for σ_i and ± 6% for R. The conductivity ratio is $\sigma_a:\sigma_b:\sigma_c$ = 1.15:1.62:1.00. The conductivity ratios reported in the literature are $\sigma_a:\sigma_b:\sigma_c$ = 1.10:2.23:1.00 by Andronik and Kot,[4] $\sigma_a:\sigma_b:\sigma_c$ = 1.6:2.6:1.0 by Kawasaki and Tanaka,[5] and $\sigma_a:\sigma_b:\sigma_c$ = 1.09:1.45:1.00 by Ermanis and Miller.[6] The values quoted here have in common the property that $\sigma_b > \sigma_a > \sigma_c$ in agreement with the data obtained here. Also the magnitude of the conductivity ratios obtained are within the limits of those reported in the literature.

The large deviation in the conductivity ratio for CdSb from the literature must be discussed further. None of the works, references 4, 5, and 6, give any details of the measurement

techniques used. Presumably the values were all obtained from d.c. electrical measurements. If extreme care was not taken to insure against temperature gradients in the samples, the large thermoelectric effects in this material would cause the results to be in error. This may be part of the cause of the large discrepancies in the values. The conductivity ratio of Andronik and Kot[4] was obtained at 90°K where some ionized impurity scattering may have altered the anisotropy due to acoustic phonon scattering which is dominant at room temperature.

The conductivity ratio of Kawasaki and Tanaka was obtained at 250°K on very pure samples with carrier concentrations $p \approx 3 \times 10^{15}$ cm^{-3}. At this temperature for this carrier concentration the material is very near to its intrinsic region. Also the problem of irreversible changes in carrier concentration is extremely severe in very pure samples. In addition, these samples were cycled over a large temperature range in the course of the measurements. Each of these points is capable of explaining an altered conductivity ratio of the Kawasaki-Tanaka material.

The conductivity ratio of Ermanis and Miller was obtained from samples with $p \approx 10^{18}$ cm^{-3} at room temperature. In samples with carrier concentrations in this range the effects of carrier concentration changes on heating would not be noticable. The conductivity ratio reported by Ermanis and Miller is the one in

closest agreement with that measured in this work. Thus the literature is not at all in agreement about the true values of the conductivity ratios of CdSb, and the measured values found here will have to be accepted with the consideration that care was taken to minimize the expected parasitic errors.

4.4 Determination of the Effective Masses

The free carrier absorption, Hall effect, and electrical conductivity measurements can now be used to obtain the effective masses for the valence band of ZnSb and CdSb. Before this can be done several points must be discussed.

The magnetoresistance measurements performed on ZnSb by Shaver[3] and on CdSb by Frei, et al,[7] show that the valence band energy ellipsoids lie along the crystallographic axes. The number of ellipsoids is not determined. This allows the expressions for the transport properties of a general ellipsoid to be adopted directly to ZnSb and CdSb by identifying the crystal axes with the ellipsoid axes. This same fact dictates the form of the free carrier absorption discussed in Appendix 2.

The expressions for the electrical conductivity and Hall coefficient are from Shaver[3]

$$\sigma = \begin{pmatrix} \sigma_a & 0 & 0 \\ 0 & \sigma_b & 0 \\ 0 & 0 & \sigma_c \end{pmatrix} \qquad (4.3)$$

where

$$\sigma_i = \frac{pe^2 < \tau_i >}{m_i^*} \tag{4.4}$$

and

$$R_{ijk} = \frac{1}{p} \frac{< \tau_i \tau_j >}{< \tau_i >< \tau_j >} . \tag{4.5}$$

In Eq. (4.5) R_{ijk} is the Hall coefficient defined by $E_i = R_{ijk} J_j B_k$ where E_i is the electric field in the i direction, J_j is the electric current density in the j direction, and B_k is the magnetic flux density in the k direction. The expressions are valid in the extrinsic region for p-type material. In Eqs. (4.4) and (4.5), τ_i is the relaxation time for the i direction and the average value brackets are defined by Eq. (4.2).

The expression for free carrier absorption is from Appendix 2

$$\alpha = \begin{pmatrix} \alpha_a & 0 & 0 \\ 0 & \alpha_b & 0 \\ 0 & 0 & \alpha_c \end{pmatrix} \tag{4.6}$$

where α_a is given by Eq. (4.1) which will be repeated here

$$\alpha_i = \frac{pe^2 \lambda^2}{(2\pi)^2 n_i c^3 \varepsilon_o m_i^*} \left\langle \frac{1}{\tau_i} \right\rangle . \tag{4.1}$$

The effective masses, the m_i^*'s appearing in Eqs. (4.4) and (4.1) are the sought after parameters.

To proceed any further, information about the form of τ the relaxation time tensor is necessary. The measurements performed by Shaver[3] on ZnSb and by Andronik and Kot[8] on CdSb show the Hall coefficient and the thermoelectric power to be isotropic in the extrinsic p region. From this fact Shaver[3] has shown that the relaxation time tensor must have a factorable energy dependence, that is, its most general form must be

$$\tau = \begin{pmatrix} A_a & 0 & 0 \\ 0 & A_b & 0 \\ 0 & 0 & A_c \end{pmatrix} E^{-s}. \qquad (4.7)$$

In Eq. (4.7) the A_i's are constants but the relaxation time can be anisotropic in that A_i does not have to equal A_j.

In the set of equations given by Eqs. (4.3), (4.5), (4.6) and (4.7) there are eight unknown quantities, namely, m_a^*, m_b^*, m_c^*, p, A_a, A_b, A_c, and s. The experimental measurements provide seven quantities for the equations, namely, the three conductivities, the three free carrier absorption coefficients, and the Hall coefficient. One additional piece of information is necessary to extract the desired information from the measurements.

The energy dependence of the relaxation time, the parameter

s in Eq. (4.7) can be obtained from the temperature dependence of the electrical conductivity in the extrinsic range or the mobility. For both materials the hole mobility varies as $T^{-3/2}$ with temperature. This behavior has been observed in ZnSb by Shaver[3] and in CdSb by Andronik and Kot[8] and by Gusev and Rakin.[9] As discussed by Smith[10] and Ziman[11] the $T^{-3/2}$ dependence of the mobility indicates that acoustic phonon scattering is the dominant scattering process in these materials. For acoustic phonon scattering the energy dependence of the relaxation time is given by s = 1/2.

By using s = 1/2 for the energy dependence of the relaxation time, the experimental data can be used with the above equations to yield the m_i^*'s and the A_i's. The average value brackets associated with τ and defined by Eq. (4.2) can now be evaluated to yield

$$< \tau_i > = \frac{4 A_i}{3(\pi k_B T)^{1/2}} \tag{4.8a}$$

$$< \frac{1}{\tau_i} > = \frac{8}{3A_i} \left(\frac{k_B T}{\pi}\right)^{1/2} \tag{4.8b}$$

$$\frac{< \tau_i \tau_j >}{< \tau_i >< \tau_j >} = \frac{3\pi}{8} . \tag{4.8c}$$

Table 4.3 shows the experimental data assembled for ZnSb and CdSb. Table 4.4 shows the effective masses and relaxation

	ZnSb			CdSb		
	a axis	b axis	c axis	a axis	b axis	c axis
Free Carrier Absorption $\alpha_i(cm^{-1})$ for λ in microns	$(1.55\pm0.03) \times 10^{-2}\lambda^2$	$(0.55\pm0.011) \times 10^{-2}\lambda^2$	$(2.75\pm0.06) \times 10^{-2}\lambda^2$	$(0.20\pm0.004) \times 10^{-2}\lambda^2$	$(0.50\pm0.01) \times 10^{-2}\lambda^2$	$(1.95\pm0.04) \times 10^{-2}\lambda^2$
Electrical Conductivity $\sigma_i(ohm\text{-}cm)^{-1}$	3.33 ± 0.23	2.30 ± 0.16	5.90 ± 0.41	0.60 ± 0.04	0.84 ± 0.06	0.52 ± 0.035
Hall coefficient for above data R (cm^3/coul.)	86 ± 5.1	80 ± 4.8	80 ± 4.8	240 ± 14	240 ± 14	240 ± 14
Refractive Index n_i	4.51 ± 0.05	4.25 ± 0.04	4.30 ± 0.04	4.70 ± 0.05	4.46 ± 0.04	4.56 ± 0.05

Table 4.3. Experimental data for ZnSb and CdSb used to calculate effective masses and relaxation time coefficients.

	ZnSb	CdSb
Effective masses		
m_a^*/m_o	0.55 ± 0.06	1.26 ± 0.13
m_b^*/m_o	1.23 ± 0.12	0.69 ± 0.07
m_c^*/m_o	0.34 ± 0.03	0.44 ± 0.04
Relaxation time coefficients ($jouls^{1/2}$ sec)		
A_a	$(0.65 \pm 0.07) \times 10^{-23}$	$(0.75 \pm 0.08) \times 10^{-23}$
A_b	$(0.93 \pm 0.09) \times 10^{-23}$	$(0.58 \pm 0.06) \times 10^{-23}$
A_c	$(0.66 \pm 0.07) \times 10^{-23}$	$(0.23 \pm 0.02) \times 10^{-23}$

Table 4.4. Effective masses and relaxation time coefficients obtained for ZnSb and CdSb.

time coefficients obtained from the experimental data and Eqs. (4.1), (4.4), (4.5), and (4.8). From the errors in the experimental results previously discussed the m_i^*'s and the A_i's should be accurate to $\pm$ 10%.

The experimental values from Table 4.4 show the relaxation time to be anisotropic. It is interesting to note that for ZnSb, A_a is approximately equal to A_c. In ZnSb there are very strong cleavage planes perpendicular to the a and c axes. For CdSb this symmetry in the A_i's is not observed and also the cleavage plane perpendicular to the c axis is not as strong as that perpendicular to the a axis. The observations on the cleavage planes are made from experience in handling and cutting the material. There may be a connection between the bond strength and the relaxation time in the various directions through the velocity of sound since the scattering is presumably via acoustic phonons.

There is slight symmetry to the experimental effective mass values for ZnSb and CdSb. The values for m_c^* for each material are quite close being 0.34 m_o for ZnSb and 0.44 m_o for CdSb. The mass of a free electron is designated by m_o. For ZnSb m_b^* is the largest effective mass, while for CdSb m_a^* is the largest. The a and b axes seem to switch roles in the materials in that for ZnSb $m_b^* \approx 2\ m_a^*$ and for CdSb $m_a^* \approx 2\ m_b^*$. The actual numbers are close to one another as well as just their ratios.

The number of extrema in the valence band can be determined from the comparison of experimental thermoelectric power with the value predicted by the experimental effective masses. From Smith,[12] the thermoelectric power for nondegenerate p-type material is given by

$$P = \frac{k_B}{e} \left[\left(\frac{5}{2} - s \right) + \ell n \left(\frac{N_v}{p} \right) \right] \tag{4.9}$$

where

$$N_v = 2N \left(2\pi m_d^* k_B T/h \right)^{3/2} \tag{4.10}$$

In Eq. (4.10), N_v is the density of states in the valence band, N the number of equivalent maxima, h is Planck's constant, and m_d^* is the density of states effective mass defined by $m_d^{*3} = m_a^* m_b^* m_c^*$.

For ZnSb, Shaver[3] has measured a thermoelectric power of 430 $\mu V/^oK$ for a sample with $p = 4.0 \times 10^{17}$ cm^{-3} at room temperature. According to Shaver,[3] this experimental value is accurate to $\pm$ 3%. There are no other reliable measurements of the thermoelectric power of ZnSb in the literature. The other measurements in the literature are either on polycrystalline material or on undoped ZnSb which has been held at high temperatures long enough so that the initial carrier concentration data has no bearing on the thermoelectric data.

When the experimental effective mass values are used to

calculate the thermoelectric power for a hole concentration of $p = 4 \times 10^{17}$ cm^{-3} at room temperature, the value 454 $\mu V/^{o}K$ is obtained for N = 1 and the value 514 $\mu V/^{o}K$ for N = 2. As the accuracy of the effective mass parameters is expected to be $\pm$ 10% and the hole concentration $\pm$ 7% (from Shaver[3]), the corresponding accuracy in the predicted thermoelectric power should be $\pm$ 18 $\mu V/^{o}K$. The value of the thermoelectric power predicted for a single extremum, 454 $\pm$ 18 $\mu V/^{o}K$ is quite close to Shaver's[3] experimental value 430 $\pm$ 13 $\mu V/^{o}K$. The accuracy limits of the two values overlap. The value of the predicted thermoelectric power for two extrema in the valence band, 514 $\pm$ 18 $\mu V/^{o}K$ is considerably higher than the experimental value.

The effect of a systematic error in the effective mass values on the predicted thermoelectric power values will be investigated here. Consider a + 5% systematic error in each m_i^*. The density of states effective mass would in turn have an error of + 5% resulting in an error in N_v of + 7.5%. The predicted thermoelectric power would then be 6 $\mu V/^{o}K$ higher than it should be without the systematic error. This is about a - 1% error in the predicted thermoelectric power. The presence of a small systematic error in the effective masses caused by carrier concentration increases in the electrical samples will thus be of little significance to the determination of the number of extrema in the valence band.

For CdSb, there is more data on the thermoelectric power of single crystal material than for ZnSb. However, most of this data is sketchy and incomplete. The thermoelectric power and carrier concentrations are not given for the same sample, or if both quantities are given for a sample, they were measured at different temperatures. The data of Andronik and Kot[8] differs from the rest of the literature in that it is both very recent and complete. They have measured the Hall coefficient and an isotropic thermoelectric power for several samples. Their data will be used to determine the number of valence band maxima in CdSb by comparison of theoretical and experimental thermoelectric power values.

For a sample at 200°K with $p = 4.4 \times 10^{15}$ cm^{-3}, Andronik and Kot[8] obtained a thermoelectric power of 790 ± 20 $\mu V/^{o}K$. For a similar sample, the effective mass values obtained here predict a value of 812 ± 18 $\mu V/^{o}K$ for N = 1 and 872 ± 18 $\mu V/^{o}K$ for N = 2. At 200°K with $p = 1.6 \times 10^{16}$ cm^{-3}, Andronik and Kot[8] measured a value of 705 ± 20 $\mu V/^{o}K$ while the predicted values are 700 ± 18 $\mu V/^{o}K$ for N = 1 and 760 ± 18 $\mu V/^{o}K$ for N = 2. On a third sample with $p = 2.2 \times 10^{17}$ cm^{-3} at the same temperature, the predicted values are 474 ± 18 $\mu V/^{o}K$ for N = 1 and 534 ± 18 $\mu V/^{o}K$ for N = 2 as compared to an experimentally measured value[8] of 440 ± 20 $\mu V/^{o}K$. In each case, the experimental value and the predicted value for N = 1 agree within

their accuracy limits. In each case, the predicted value for N = 2 is considerably higher than the experimental value.

For both materials, the predicted thermoelectric power values for a single extremum are in good agreement with experimental values. This does not constitute positive evidence that there is a single maximum in the valence band. However, there is certainly evidence to suspect that both materials have a single maximum in their valence bands. The consequences of this conclusion will be pursued further in the next sections.

The first Brillouin zone of ZnSb and CdSb is a rectangular parallelepiped centered on the origin of k-space with edges aligned along the axes. Associating the real space coordinates x, y, z with the unit cell edges a, b, c, respectively, the first Brillouin zone has dimensions $2\pi/a$, $2\pi/b$, $2\pi/c$ in the k_x, k_y, k_z directions. The point group symmetry of both compounds is essentially three perpendicular mirror planes. Since the extremum ellipsoid has its axes along the k-space axes, the maximum can occur in k-space at the origin Γ (0, 0, 0), the zone corner, R $\left(\frac{\pi}{a}, \frac{\pi}{b}, \frac{\pi}{c}\right)$, or the center of the zone faces X $\left(\frac{\pi}{a}, 0, 0\right)$, Y $\left(0, \frac{\pi}{b}, 0\right)$ or Z $\left(0, 0, \frac{\pi}{c}\right)$. Both Khartsiev[13] and Frei and Velicky[14] have shown that group theory will allow E(k) to have zero gradient in all three directions at the points Γ and R, and not at X, Y, or Z.

Stevenson[15] has observed cyclotron resonance in both p-type ZnSb and p-type CdSb. The experiments were done at liquid helium temperatures and across the gap optical excitation of carriers was necessary to observe the resonance. When a filter passing only photons of energy 0.20 V or less was used on the optical excitation source, the resonance was not observed. Stevenson was unable to determine the charge sign of the carrier causing the resonance experimentally. He obtained the effective mass values $m_a^* = 0.175\ m_o$, $m_b^* = m_c^* = 0.146\ m_o$ for ZnSb and $m_a^* = m_c^* = 0.159\ m_o$, $m_b^* = 0.140\ m_o$ for CdSb. The acceptor levels are from 0.005 to 0.008 ev away from the valence band in both materials.[3,16] In CdSb the donor levels are about 0.27 to 0.30 ev away from the conduction band[17] and in ZnSb the donor levels are even farther away as the material cannot be made n-type. The observed resonances seem most likely due to electrons and not relevant for comparison with those obtained here. Stevenson[15] states that the reason he could not see the hole resonance is because the hole relaxation time was too short or the hole effective mass values put the resonance outside the range of his equipment.

All other determinations of the effective mass parameters in the literature are based on transport properties alone. The effective mass and relaxation time cannot be uncoupled by low frequency transport measurements alone. Thus the other mass

determinations are, in reality, determinations of $< \tau_i > / m_i^*$ rather than of effective masses. The agreement of the transport results with others in the literature was discussed in Section 4.3

If the valence band is degenerate at the extremum or if two bands are occupied by holes the interpretation of the free carrier absorption data will be in error. In Si and Ge at $k = 0$, the valence band consists of a fourfold degenerate state with spin and a twofold degenerate state below split off by spin orbit interaction.[18] Therefore the valence band of Si and Ge is actually composed of three bands, since the fourfold state splits into two bands for $k \neq 0$, rather than a single band. Optical transitions are allowed between bands for $k \neq 0$ as well as transitions within a given band. In Ge the structure of the valence band causes the free carrier absorption to deviate from a simple λ^2 dependence and to become a series of peaks and valleys.[19] In Si where the split off band is not as far removed from the other band the free carrier absorption does not show any structure but follows a linear dependence on λ^2.[20] Thus the λ^2 dependence of the free carrier absorption observed for ZnSb and CdSb is not enough to insure a simple valence band for these materials. If interband transitions as well as intraband transitions are contributing to the absorption in this energy range, the simple interpretation used in this work is in error.

If intraband transitions from more than one band are contributing to the absorption, the effective masses obtained pertain to some properly weighted average of the properties of the bands involved rather than to the properties of a single band.

The experimental data shows the extremum to be at either Γ or R. Frei and Velicky[14] have shown that in the spinless case, only one dimensional representations are possible at Γ and only two dimensional representations are possible at R. The point group of the material contains inversion so that all states must be doubly degenerate with spin considered. In the spin case Frei and Velicky[14] have shown that only two dimensional representations are possible at both Γ and R. Thus the valence band extremum cannot be degenerate other than for spin. The possibility of a degenerate valence band is ruled out.

The Hall coefficient of a p-type material where more than one type of hole is present is not independent of magnetic field.[22] For CdSb and ZnSb over wide ranges of temperature and magnetic field strength, the Hall coefficient is found to be independent of magnetic field.[3,23] Thus it is quite likely that in each only one type of hole is present to contribute to the transport properties. The possibility exists of there being a valence band several k_BT from the highest valence band which will not affect transport properties but will affect

optical absorption. If such interband transitions were to contribute to the absorption, the affect would probably be strong and would not behave linearly with λ^2.

There appears to be quite a bit of evidence to justify the use of a simple, one type of hole, model that has been used here.

REFERENCES

1. M. Zavetova, Czech. J. Phys., B14, 271 (1964).

2. H. Komiya, K. Masumoto, and H. Y. Fan, Phys. Rev., 133, A1679 (1964).

3. P. Shaver, Phys. Rev., 141, 649 (1966).

4. I. Andronik and M. Kot, Fiz. Tver. Tela, 2, 1128 (1960).

5. T. Kawasaki and T. Tanaka, Japan J. Appl. Phys., 2, 516 (1963).

6. F. Ermanis and E. Miller, J. Electrochem. Soc., 108, 1048 (1961).

7. V. Frei, M. Matyas, B. Velicky, and M. Zavetova, Proc. Int. Conf. on Physics of Semiconductors at Exeter, p. 766, Inst. of Physics and Phys. Soc., London (1962).

8. I. Andronik and M. Kot, Akad. Nauk. SSSR Ser. Fiz., 28, 1028 (1964).

9. S. Gusev and G. Rakin, Soviet Physics-Solid State, 4, 1704 (1963).

10. R. A. Smith, "Semiconductors", p. 135, Cambridge Univ. Press, Cambridge (1959).

11. J. M. Ziman, "Electrons and Phonons", p. 431, Oxford Univ. Press, Oxford (1960).

12. R. A. Smith, Ibid, p. 172.

13. V. Khartsiev, Soviet Physics-Solid State, 4, 721 (1962).

14. V. Frei and B. Velicky, Czech. J. Phys., B15, 43 (1965).

15. M. J. Stevenson, Proc. of the Int. Conf. on Semiconductor Physics, Prague, 1960, p. 1083.

16. I. Andronik, M. Kot, and O. Emel'yanenko, Soviet Physics-Solid State, 3, 1853 (1962).

17. I. Pilat and L. Anatychuk, Soviet Physics-Solid State, 6, 1195 (1964).

18. C. Kittel, "Quantum Theory of Solids", p. 268, Wiley, New York (1963).

19. T. S. Moss, "Optical Properties of Semiconductors", p. 129, Butterworth, London (1959).

20. T. S. Moss, Ibid, p. 113.

21. R. A. Smith, Ibid, p. 360.

22. E. H. Putley, "The Hall Effect and Related Phenomena", p. 119, Butterworth, London (1960).

23. L. Stouvac, Czech. J. Phys., B15, 141 (1965).

CHAPTER V. MEASUREMENTS ON $Cd_xZn_{1-x}Sb$ ALLOYS AND INTERPRETATION

5.1 Optical Absorption

From consideration of the effective masses of ZnSb and CdSb it was decided to investigate the a and b axes of the alloy system. Investigating all three axes thoroughly would have required an excessive amount of time. Thus an effort was made to choose the area where the results would be most interesting. For CdSb and ZnSb, m_c^* is very similar in that in both cases it is not only the smallest mass but also almost numerically equal in the two compounds. On the other hand, m_a^* and m_b^* seem to change roles as the largest and second largest mass in each material. More changes seem to be occurring along the a and b than along the c axis in the transition from ZnSb to CdSb.

Regions of alloy ingots were oriented and cut perpendicular to the c axis. Then the length of the c axis was measured and used to determine the composition of the region. A linear variation was confirmed by wet chemical analysis. The c axis was the closest major axis to the growth axis for all of the ingots. Thus the c axis was almost perpendicular to the planes of constant composition due to the mechanics of the crystal growth. The maximum change in alloy composition would be

expected to occur along the c axis with the composition remaining constant along the a and b axes. As discussed in Section 2.3, there is present a variation in composition along the growth axis of less than 1% per cm. To minimize the effect of such composition gradients on the measurements, all measurements were taken on samples cut from an ingot region 6 or 7 mm long. This permitted the cutting of three slices. The center slice was used for optical measurements and the adjacent slices were used for electrical measurements.

For purposes of both cutting the electrical samples and orienting the electric field for the optical measurements, it was necessary to know the directions of the crystal axes, a and b, in the slice plane. This was accomplished in the following way. First a Laue photograph was made of the slice along the c axis. Then the directions of the twofold axes were transferred from the photograph to the slice. A small flat was cut near the edge of the slice parallel to the c and one of the twofold axes and perpendicular to the other twofold axis. Using the flat surface, the lattice constant of the axis perpendicular to the flat surface could be determined. This immediately determined the identity of this axis as a or b as the two do not overlap for any compositions. The size of the lattice parameter could then be used as a check on the alloy composition.

There was not enough time or material available to measure the refractive indices of the alloy samples. The changes in refractive index from ZnSb to CdSb are not very large. As determined experimentally, for ZnSb, $n_a = 4.51$ and $n_b = 4.25$, while for CdSb, $n_a = 4.70$ and $n_b = 4.46$. Arbitrarily, the dielectric constant, $K_i = n_i^2$, was taken to vary linearly across the composition range. This approximation should be sufficiently accurate for interpretation of the transmission data. Thus the refractive indices determined from the linear approximation to the variation of the dielectric constants will be used to convert the transmission data to absorption data.

Using the same optical system and techniques used on ZnSb and CdSb, the transmission versus wavelength data was obtained for the a and b axes of 8 samples of $Cd_xZn_{1-x}Sb$. For each sample, two transmission curves were obtained, one for radiation linearly polarized along each axis. Each transmission curve was measured at least twice to assure reproducibility of the data. Then using the approximate refractive indices appropriate to the alloy sample composition, the transmission data was converted to absorption data.

In each case the absorption coefficient was found to vary linearly with λ^2 for λ between 7 and 15 μ. This is exactly the same behavior that was observed on the pure compounds ZnSb and

CdSb. As in the former cases, the portion of the absorption coefficient that varies linearly with λ^2 may be taken as free carrier absorption. A wavelength independent component of absorption was present on all samples measured, again similar to the data from ZnSb and CdSb. The free carrier absorption observed in the alloy samples is given in Table 5.1. The estimated accuracy of the free carrier absorption is $\pm$ 5%. The table also contains the sample identification number, sample composition, conductivities, and Hall coefficient for each sample.

The various alloy samples had different carrier concentrations and structure sensitive relaxation times. Thus the variation in absorption coefficients α_a and α_b with composition cannot be obtained directly. However, if the ratio α_a/α_b is used, the carrier concentration and structure sensitivity cancel out and a comparison can be made between samples. Figure 5.1 shows the variation in the free carrier absorption anisotropy α_a/α_b versus composition for the $Cd_xZn_{1-x}Sb$ alloys. From the figure, α_a/α_b changes abruptly for low alloy concentrations and remains relatively constant across the mid-range of x. The form of presentation of this data is somewhat deceptive. If the ratio α_b/α_a rather than α_a/α_b had been plotted versus composition, the behavior near CdSb would appear more abrupt. In fact, the data is somewhat symmetrical in that an abrupt change is observed within 0.1 in x at each end ZnSb and CdSb.

Sample Number	Composition Parameter x	Free Carrier Absorption (cm^{-1}) for λ in microns		Electrical Conductivity $(ohm\text{-}cm)^{-1}$		Hall Coefficient R
		$\alpha_a x10^2/\lambda^2$	$\alpha_b x10^2/\lambda^2$	σ_a	σ_b	(cm^3/coul)
x-1041	0	(1.55 ± 0.03)	(0.51 ± 0.01)	3.33 ± 0.23	2.14 ± 0.15	86 ± 6
x-1042	0.06	(1.02 ± 0.05)	(0.60 ± 0.03)	2.32 ± 0.19	1.51 ± 0.12	106 ± 7
x-1042*	0.09	(1.10 ± 0.05)	(0.63 ± 0.03)	4.34 ± 0.35	2.43 ± 0.19	64 ± 4
x-1046	0.28	(1.83 ± 0.09)	(0.97 ± 0.05)	2.98 ± 0.24	2.12 ± 0.17	50 ± 3.5
x-1025	0.55	(2.14 ± 0.11)	(1.07 ± 0.05)	6.34 ± 0.50	3.75 ± 0.30	30 ± 2
x-1022	0.68	(1.87 ± 0.09)	(0.94 ± 0.05)	6.02 ± 0.48	3.27 ± 0.26	28 ± 2
x-1021	0.80	(0.55 ± 0.03)	(0.36 ± 0.02)	0.88 ± 0.07	0.57 ± 0.05	116 ± 8
x-1020	0.90	(0.56 ± 0.03)	(0.53 ± 0.03)	0.56 ± 0.04	0.35 ± 0.03	160 ± 11
x-1018	0.91	(0.57 ± 0.03)	(0.63 ± 0.03)	0.44 ± 0.03	0.33 ± 0.03	180 ± 13
x-1014	1.00	(0.20 ± 0.004)	(0.50 ± 0.01)	0.60 ± 0.04	0.84 ± 0.06	240 ± 17

Table 5.1. Electrical and optical parameters measured for the a and b axes of samples of $Cd_xZn_{1-x}Sb$ alloys.

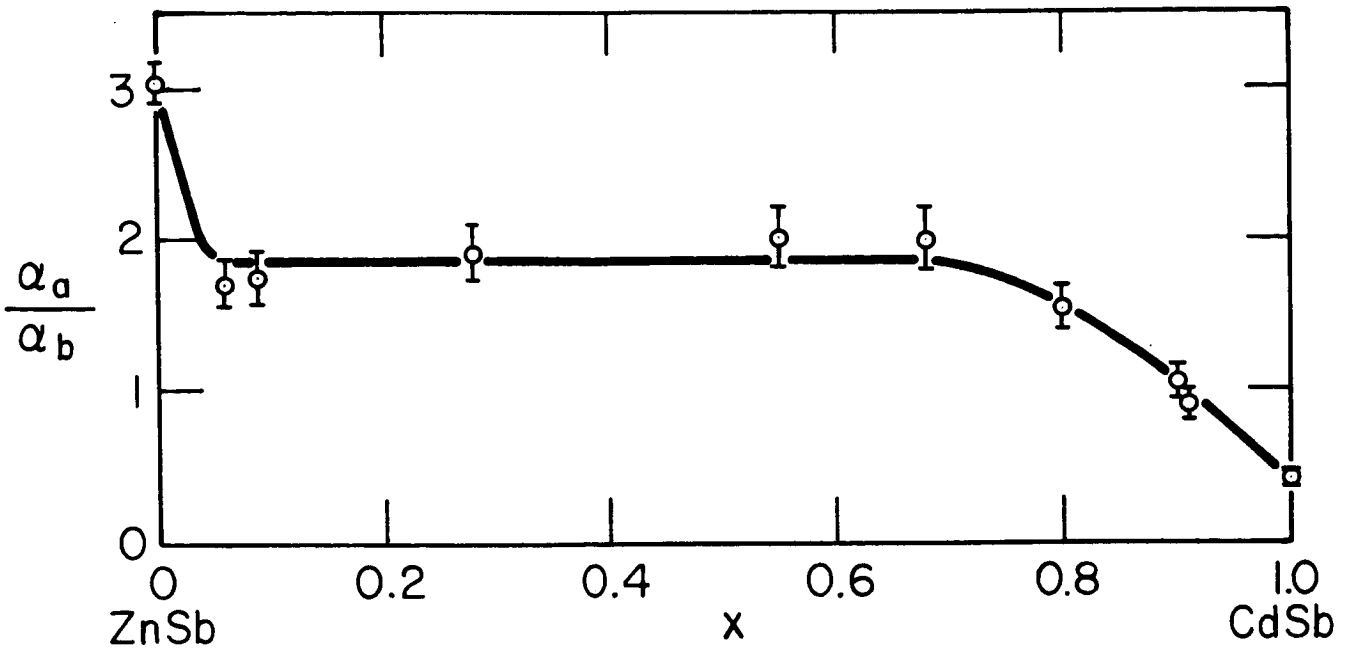

Figure 5.1. Ratio of free carrier absorption coefficients α_a/α_b versus x for $Cd_xZn_{1-x}Sb$.

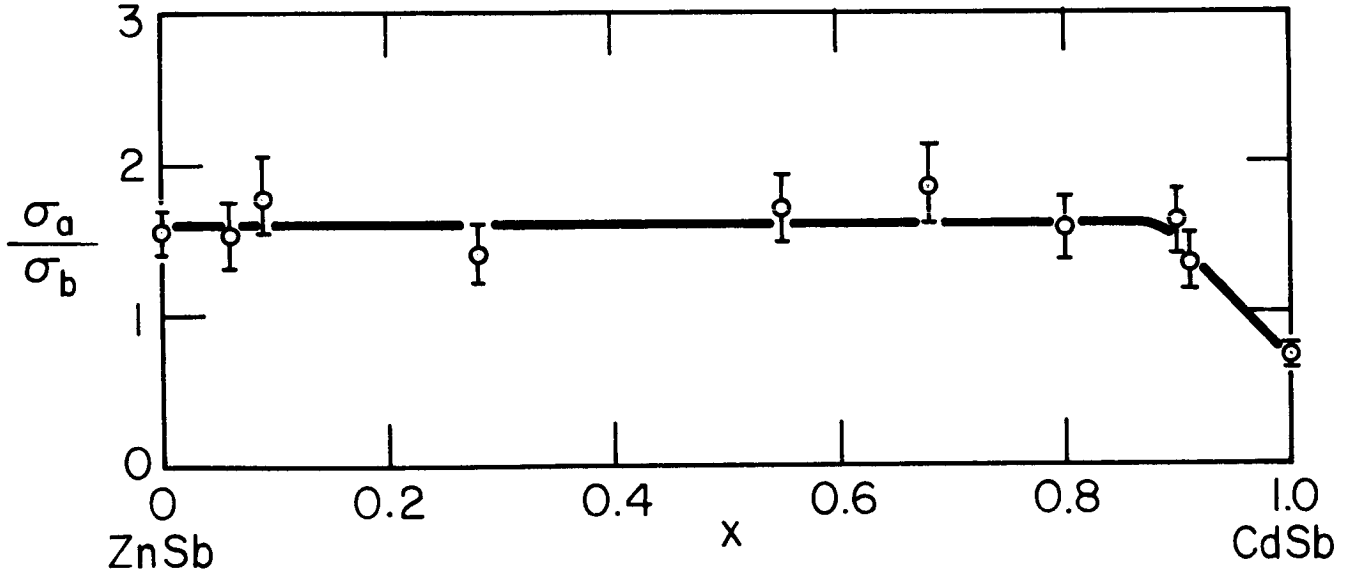

Figure 5.2. Ratio of electrical conductivities σ_a/σ_b versus x for $Cd_xZn_{1-x}Sb$.

5.2 Conductivity and Hall Effect

To further characterize the samples on which optical measurements were made, it was desirable to measure the electrical conductivities and Hall coefficients of the alloys. The slices on each side of the one which was fabricated into an optical sample were cut into oriented electrical samples. To maximize the number of samples, each slice was cut into samples of the same orientation. Thus for each optical sample, the adjacent slice on one side was cut into 3 or 4 a axis conductivity and Hall samples, while the adjacent slice on the other side was cut into 3 or 4 b axis samples.

The sample fabrication and measurement techniques were identical to those used for the ZnSb and CdSb samples. A large standard deviation, about 8% for electrical conductivity 7% for Hall coefficient, was observed in the data. The problem of irreversible increases in hole concentration occurring when contacts are soldered to the samples is probably still present for the alloy material as well as for the pure material. Thus there is reason to suspect the presence of a systematic error in the data. The evidence in behalf of a systematic error is very sketchy. For 3 of the 8 samples measured the standard deviation for the Hall mobility data was much less than the standard deviation of the Hall or conductivity data. The other 5 samples showed no evident trends in the standard deviations

of the data. The number of samples involved in each set of data, 4 for the conductivity, 8 for the Hall coefficient, is too small to be statistically meaningful. On one sample the electrical data was rechecked one month after the initial measurements were made. The new data showed a 4% decrease in hole concentration from the earlier data. This value of 4% may be taken as a reasonable estimate of any systematic error present. In the discussion of the data for ZnSb and CdSb, it was shown that such an error is of little consequence to the values of effective masses and relaxation time coefficients ultimately obtained. On this basis the error estimates will be made without an attempt to correct for the presence of a systematic error.

The probable error range for the conductivity values will be taken as the standard deviation of the data or $\pm$ 8%. Similarly the probable error range for the Hall coefficient values will be taken as $\pm$ 7% from the standard deviation of the data.

The electrical data for the alloy samples used is given in Table 5.1. As in the case of the absorption coefficients, the ratio σ_a/σ_b is the most meaningful comparison to make between samples. This measure eliminates the effect of different carrier concentrations and structure sensitivity. Figure 5.2 shows the anisotropy of the electrical conductivities σ_a/σ_b versus composition for the alloys measured. This ratio appears

to stay constant for $0 < x < 0.8$ and then drop in the region near CdSb.

5.3 Determination of the Effective Masses

The next step in the data analysis is to determine the effective masses and relaxation time coefficients for the a and b axes of the alloys. The available data is the measured free carrier absorption, the electrical conductivity and Hall coefficient for each axis. The expressions for the individual components of the free carrier absorption and electrical conductivity, Eqs. (4.1) and (4.3), are valid for the alloys as well as ZnSb and CdSb. Also the expression for the Hall coefficient, Eq. (4.5), is equally valid. The only essential difference lies in the form of the relaxation time.

The form of the relaxation time, Eq. (4.7), cannot be taken as directly applicable to the alloy system without some discussion. The end compounds, ZnSb and CdSb, have been shown to have acoustic phonon scattering as the dominant scattering mechanism. As either compound is alloyed in small concentrations, the acoustic phonon scattering should not disappear but rather remain present. Added to this portion of the scattering will be an additional component due to the alloying perturbing the periodic lattice. The resulting relaxation time will be a combination of the two relaxation times given by

$$\frac{1}{\tau} = \frac{1}{\tau_{\text{ac. phonon}}} + \frac{1}{\tau_{\text{alloy}}} . \qquad (5.1)$$

In Appendix 3, alloy scattering is discussed and shown to vary with energy as $E^{-1/2}$. As acoustic phonon scattering varies as $E^{-1/2}$ also, the energy dependence of the relaxation time is factorable. Thus Eq. (4.7) with s = 1/2 can be used for the form of the relaxation time. If this form of the relaxation time could not be used, the effective masses and relaxation times could not be extracted from the experimental data.

The values for the effective masses, m_a^* and m_b^*, and the relaxation time coefficients, A_a and A_b, for the alloy samples are shown in Table 5.2. These parameters are obtained in a manner identical to that used previously for the pure compounds. For convenience in comparison, the values for ZnSb and CdSb from the previous chapter are included in the Table. The effective masses for the alloys have an estimated accuracy of $\pm$ 13% based on the experimental errors present in the data. Also the relaxation time coefficients have an accuracy of $\pm$ 10%.

Figure 5.3 shows the ratio of the relaxation times A_a/A_b versus composition. For an isotropic relaxation time A_a/A_b equals one. The data shows deviations from isotropy only for very low alloy concentrations. This is the behavior that would be expected from the nature of the relaxation time. The relaxation time has two processes competing for dominance, acoustic

Sample Number	Composition Parameter x	Effective Masses		Relaxation Time Coefficients	
		m_a^*/m_o	m_b^*/m_o	$A_a x10^{23}$(joule$^{1/2}$-sec)	$A_b x10^{23}$(joule$^{1/2}$-sec)
x-1041	0	0.55 ± 0.06	1.23 ± 0.12	0.65 ± 0.07	0.93 ± 0.09
x-1042	0.06	0.66 ± 0.09	1.09 ± 0.14	0.67 ± 0.07	0.72 ± 0.07
x-1042*	0.09	0.77 ± 0.10	1.39 ± 0.18	1.06 ± 0.10	1.08 ± 0.11
x-1046	0.28	0.91 ± 0.12	1.53 ± 0.20	0.56 ± 0.06	0.67 ± 0.07
x-1025	0.55	0.96 ± 0.12	1.80 ± 0.23	0.75 ± 0.08	0.84 ± 0.08
x-1022	0.68	1.12 ± 0.15	2.22 ± 0.29	0.78 ± 0.08	0.84 ± 0.08
x-1021	0.80	1.29 ± 0.17	2.06 ± 0.27	0.55 ± 0.06	0.56 ± 0.06
x-1020	0.90	1.10 ± 0.14	1.56 ± 0.20	0.33 ± 0.03	0.29 ± 0.03
x-1018	0.91	1.17 ± 0.15	1.31 ± 0.17	0.26 ± 0.03	0.22 ± 0.02
x-1014	1.00	1.26 ± 0.13	0.69 ± 0.07	0.88 ± 0.09	0.23 ± 0.02

Table 5.2. Effective masses and relaxation time coefficients calculated for a and b axes of $Cd_xZn_{1-x}Sb$ alloy samples.

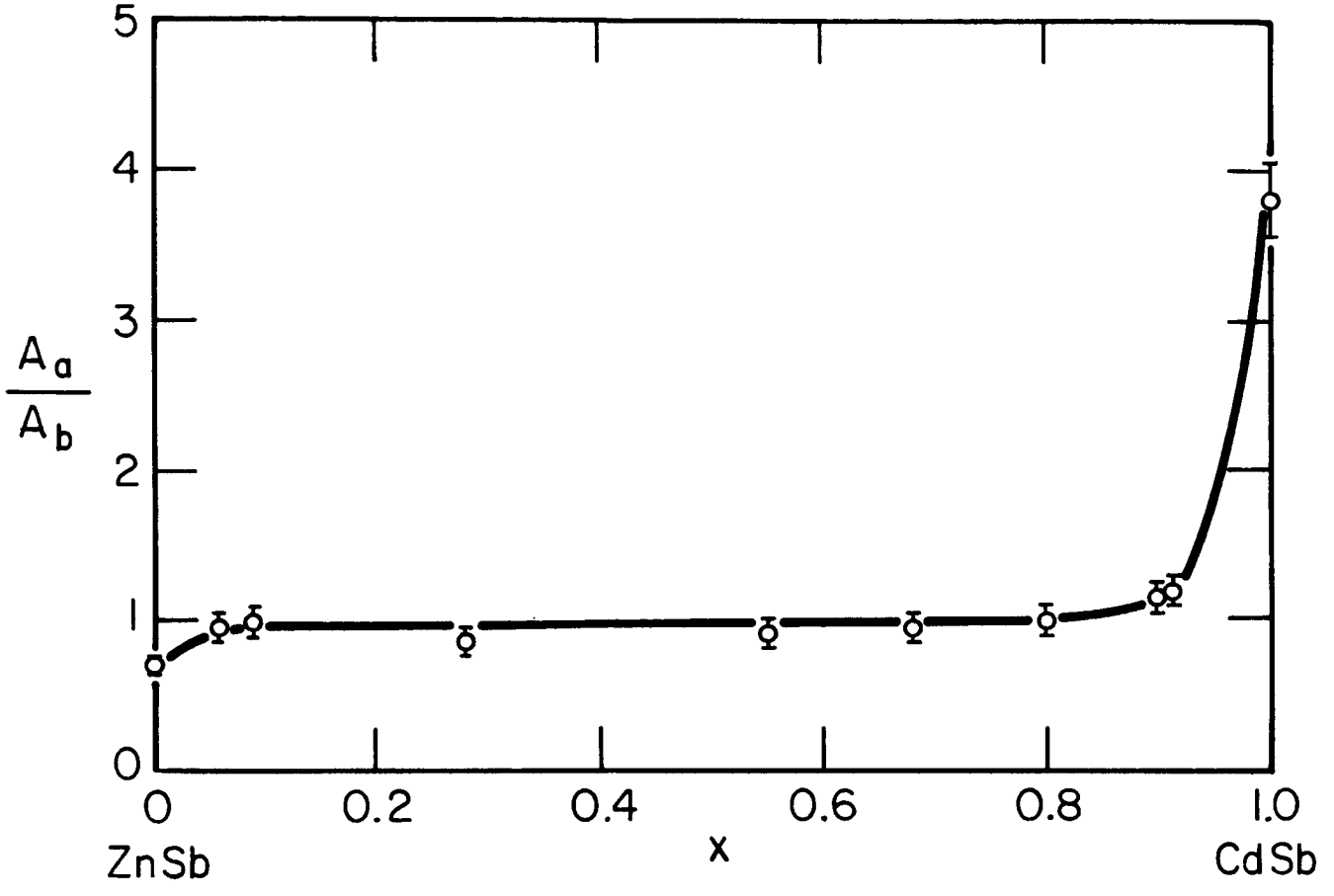

Figure 5.3. Ratio of relaxation time coefficients A_a/A_b versus composition for $Cd_xZn_{1-x}Sb$ alloys.

phonon scattering and alloy scattering. The acoustic phonon scattering has been shown to be anisotropic in the end compounds. There is no reason why this type of scattering should suddenly become isotropic upon alloying. On the other hand, by the randomness of the disorder in the lattice, the alloy scattering should be isotropic. The expected behavior of the relaxation time with composition would be that the anisotropic scattering is dominant near the pure compounds and the isotropic scattering is dominant over the mid-range of alloy composition. The behavior of A_a/A_b in Figure 5.3 follows this pattern very nicely.

Figures 5.4 and 5.5 show m_a^*/m_o and m_b^*/m_o, respectively, versus composition for the alloy system $Cd_xZn_{1-x}Sb$. The data for m_b^*/m_o in Figure 5.5 shows a definite rise and than a steeper fall with increasing x. The data for m_a^*/m_o in Figure 5.4 shows a much more gradual variation with x. The progression from ZnSb to CdSb for m_a^*/m_o shows some deviation from a straight line so that it cannot be taken as simply linear. However, its curvature is so slight and the error limits large enough so that no single curve can be drawn through the data with confidence. A curve following somewhat the general shape of the m_b^*/m_o curve will fit the experimental points and has been drawn through the data in addition to a straight line.

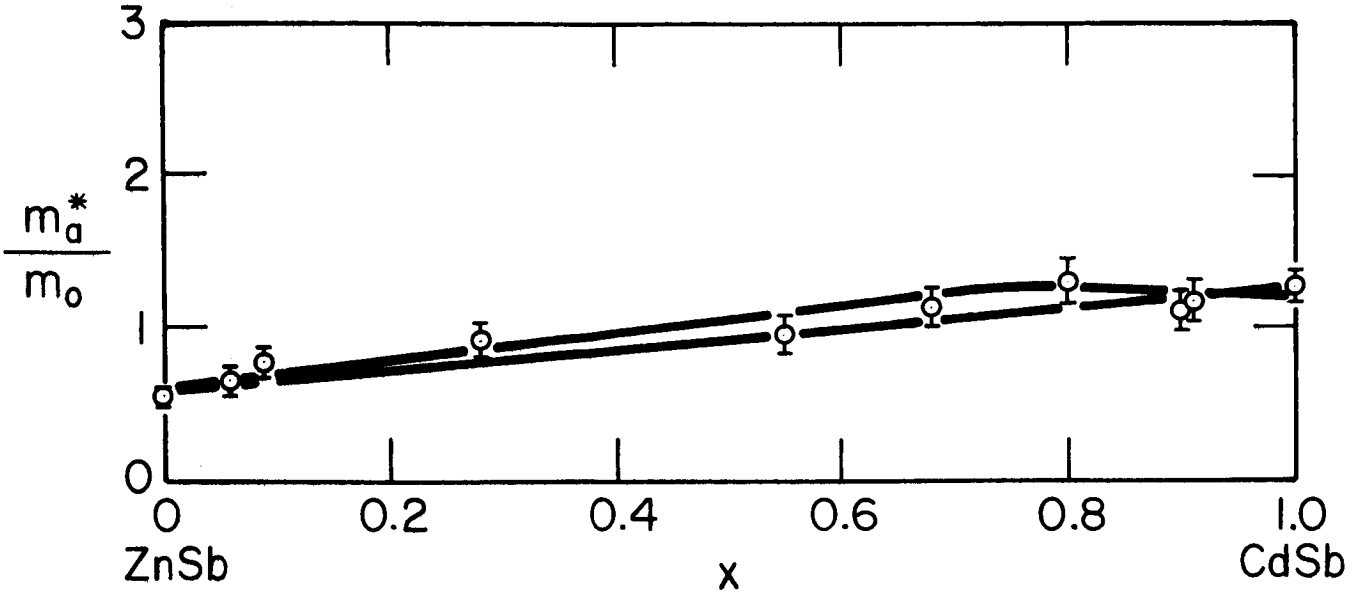

Figure 5.4. Effective mass for a axis versus composition for $Cd_xZn_{1-x}Sb$ alloys.

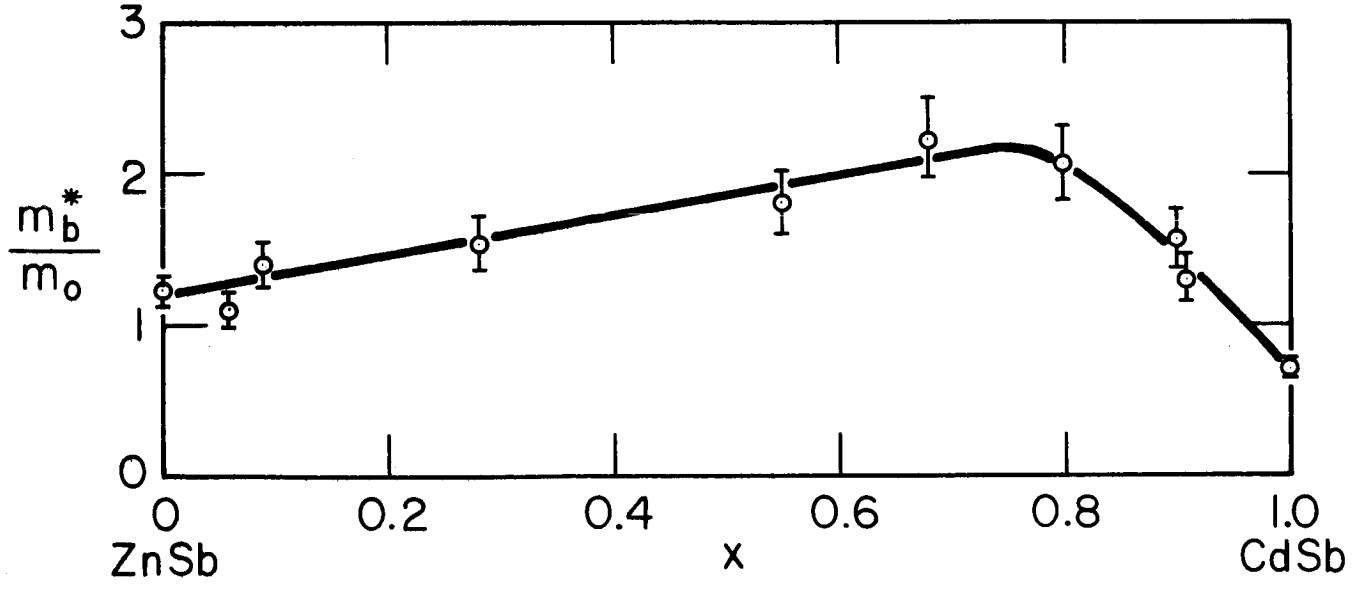

Figure 5.5. Effective mass for b axis versus composition for $Cd_xZn_{1-x}Sb$ alloys.

5.4 Discussion of Results

The unit cell of ZnSb and CdSb contains 16 atoms, eight of each type. As Zn or Cd has 2 valence electrons and Sb has 5, there are 56 valence electrons to accomodate per unit cell. Since the space group of the materials contains the inversion operator, all electron states must be doubly degenerate with spin considered. Thus in addition to the energy bands of the core electrons there are 28 energy bands below the energy gap of the material. This represents an extremely complicated situation for computation or meaningful discussion of the band structure.

The band structure of ZnSb or CdSb is not known. The locations of the extrema of the valence and conduction bands in the Brillouin zone are not known. This presents a severe handicap on the further analysis of the data on the alloy system. However, the behavior can be discussed in very general terms.

In a strict sense a structure is either periodic or it is not. In an alloy the basic periodicity of the lattice is broken. As a result, $\vec{k}$ the crystal momentum is no longer a good quantum number and conventional band theory cannot be applied to alloys. In reality, the effect of alloying is not found to be extremely severe. Energy gaps and semiconducting properties are found to exist in semiconductor solid solutions. Nordheim[1] has proposed a "virtual crystal" approximation to an alloy. This approximation

consists of replacing the exact potential of the alloy with a periodic potential. The periodic potential should be an average of the actual potential in all possible atomic configurations. Then the energy bands can be obtained for the "virtual crystal" by conventional means. The effect of the actual disorder can then be applied as a perturbation to the resulting energy bands. This scheme has been tried and found to work well for the Ge-Si alloy system.[2] At present it is the only tractable scheme for handling an alloy and it is very fortunate that it seems to work quite well.

Using such a "virtual crystal" scheme the transition from ZnSb to CdSb can be viewed in k-space as a continuous transition from one set of bands to another. Small increments in alloy concentration should not affect the average potential severely. In turn the bands should not be radically changed by a small change in potential. Thus the change in band structure should be continuous across the entire composition range. The movement of the bands and the changing electron wave functions will in turn affect the effective masses. The behavior of the effective masses can be predicted by the use of $\vec{k} \cdot \vec{p}$ perturbation theory.

The $\vec{k} \cdot \vec{p}$ perturbation theory has been discussed by E. Kane[3,4] and C. Kittel.[5] Given the electron energy levels and wavefunctions for $\vec{k} = \vec{k}_o$ and given that the energy $E_i(k_o)$ is an extremum of energy for band i, the theory predicts the behavior

of $E_i(\vec{k} - \vec{k}_o)$ for small $|\vec{k} - \vec{k}_o|$. To terms of second order in $|\vec{k} - \vec{k}_o|$, the energy for band i is given by $\vec{k} \cdot \vec{p}$ perturbation theory as

$$E_i(\vec{k}-\vec{k}_o) = E_i(\vec{k}_o) + \frac{\hbar^2}{2m}(\vec{k} - \vec{k}_o)^2 + \sum_{\mu,\alpha,\beta} \frac{h^2}{m^2} \frac{< b_i|p_\alpha|b_\mu >< b_\mu|p_\beta|b_i > (\vec{k}-\vec{k}_o)_\alpha (\vec{k}-\vec{k}_o)_\beta}{E_i(\vec{k}_o) - E_\mu(\vec{k}_o)} . \quad (5.2)$$

In Eq. (5.2) i is the index of the band that has an extremum at $\vec{k}_o$ and μ is the index of all other bands that have states at $\vec{k}_o$. Also α and β are the direction indices in k-space and $< b_i | p_\alpha | b_\mu >$ is the matrix element of the α component of the momentum operator with the wavefunction of state i and μ at $\vec{k} = \vec{k}_o$.

For a parabolic valence band the effective mass is defined by expanding the energy to second order in $|\vec{k} - \vec{k}_o|$ about $\vec{k}_o$ as

$$E_i(\vec{k}-\vec{k}_o) = E_i(\vec{k}_o) - \sum_{\alpha,\beta} \frac{\hbar^2}{2m^*_{\alpha\beta}} (\vec{k}-\vec{k}_o)_\alpha (\vec{k}-\vec{k}_o)_\beta . \quad (5.3)$$

In Eq. (5.3), $1/m^*_{\alpha\beta}$ is the reciprocal effective mass tensor element with indices $\alpha\beta$. By comparison of Eq. (5.2) with (5.3) the reciprocal effective mass tensor elements are given by $\vec{k} \cdot \vec{p}$ perturbation theory as

$$\frac{m}{m^*_{\alpha\beta}} = -\delta_{\alpha\beta} - \sum_{\mu} \frac{2 < b_i|p_\alpha|b_\mu >< b_\mu|p_\beta|b_i >}{m\,[E_i(\vec{k}_o) - E_\mu(\vec{k}_o)]} \tag{5.4}$$

where $\delta_{\alpha\beta}$ is the Kronecker delta symbol. For a coordinate system in which the effective mass tensor is diagonal along axes a, b, and c, Eq. (5.4) yields:

$$\frac{m}{m^*_a} = -1 - \sum_{\mu} \frac{2}{m} \frac{< b_i|p_a|b_\mu >< b_\mu|p_a|b_i >}{E_i - E_\mu} \tag{5.5a}$$

$$\frac{m}{m^*_b} = -1 - \sum_{\mu} \frac{2}{m} \frac{< b_i|p_b|b_\mu >< b_\mu|p_b|b_i >}{E_i - E_\mu} \tag{5.5b}$$

$$\frac{m}{m^*_c} = -1 - \sum_{\mu} \frac{2}{m} \frac{< b_i|p_c|b_\mu >< b_\mu|p_c|b_i >}{E_i - E_\mu} \tag{5.5c}$$

In Eqs. (5.5) i is the index of the valence band and μ is a running index over all the other bands.

From Eqs. (5.5), the following observation can be drawn. The denominators of the terms in each effective mass equation are the same for each mass component. Thus the numerators of the terms or the directional momentum matrix elements must be responsible for effective mass anisotropies.

In CdSb and ZnSb, the band structure is not known. Thus the value of $\vec{k}_o$, the separation in energy of the states at $\vec{k}_o$, and the wavefunctions are not known for either material. Much less, the movement of the bands with composition is not known.

The elements which enter the $\vec{k} \cdot \vec{p}$ theory are just not available. The only course left open is to assume variations in the parameters. The behavior of other alloy systems about which more is known can be used as a guide in making these assumptions.

Bassani and Brust have calculated the energy bands of the virtual crystal of the Ge-Si alloy system.[2] Their data shows that the bands in Ge-Si alloy move almost linearly in energy with composition from the energy bands of pure Ge to the bands of pure Si. Thus there is some evidence which states that the bands in the virtual crystal vary linearly with composition from one end to the other.

There are no such trends that are observed in the behavior of the momentum matrix elements. In fact, there are very few materials for which the wavefunctions are known with any certainty. It is a trait of band calculations that good energy levels can be obtained without good wavefunctions. Thus even for materials for which the band structure is well known, the wavefunctions obtained from the calculations may be very inaccurate.

S. Rabii[6] has calculated the band structure of PbSe and PbS by the latest techniques using the APW method. PbSe and PbS both have the NaCl crystal structure and have a common sublattice. In this way they are somewhat analogous to ZnSb and

CdSb which both have the D_{2h}^{15}, in the Schoenflies notation, crystal structure and have a common sublattice. Both PbSe and PbS have direct energy gaps at the same point in k-space. Thus in evaluating the theoretical effective masses for the valence band, Rabii has calculated the matrix elements which occur in the $\vec{k} \cdot \vec{p}$ theory for both materials. The matrix elements and the energy separations which determine the effective mass were compared for PbS and PbSe. No trends in the data were found. Some energy differences decreased while others increased. Similarly, the matrix elements for the two materials were not equal. In going from PbS to PbSe, some matrix elements increased while others decreased.

Thus the situation appears to be that both the energy separation between states and the momentum matrix elements will change with alloying. The change in the energy separation with alloying may be approximated by a linear variation between the two materials with some confidence. No evidence is available which suggests the manner of change for the matrix elements.

For ZnSb and CdSb to consider the effective mass is determined by the interaction of just a few states is a great oversimplification, especially in light of the complex band structure caused by the large number of atoms per unit cell. Nevertheless it is instructive to see if the general shape of the effective

mass versus composition curves can be achieved with simple models. If this can be done, it lends plausibility to the experimental data. Thus the following discussion is not intended to in any way propose with rigor a model for the behavior. Rather it is an attempt to see if the trends in the data may be reproduced with very oversimplified models.

Since there is some evidence that the energy separation between states changes linearly with composition and no evidence for the change in matrix elements, the models considered will have constant matrix elements and linearly changing energy separation between states. Then Eq. (5.5) can be written as a function of x as

$$\frac{m_o}{m_i^*} = -1 - \sum_n \frac{C_{on}}{E_o - E_n + \triangle_n x}. \qquad (5.6)$$

In Eq. (5.6) C_{on} is a constant, E_o is the energy of the valence band state for ZnSb, E_n is the energy of state n for ZnSb, and $\triangle_n$ is the change in energy separation between states o and n in the transition from ZnSb to CdSb. Also $\triangle_n$ can be positive or negative. From Eq. (5.6), states higher in energy than E_o, $E_o - E_n < 0$, will give a positive contribution to m_o/m_i^*, while states lower in energy than E_o, $E_o - E_n > 0$, will give a negative contribution. This equation may be rewritten as

$$\frac{m}{m_i^*} = -1 - \sum_{n \text{ for } E_o - E_n > 0} \frac{A_n}{1 + B_n x} + \sum_{n \text{ for } E_o - E_n < 0} \frac{A_n}{1 + B_n x} \qquad (5.7)$$

where A_n is a constant and $B_n = \Delta_n / |E_o - E_\mu|$ is a constant which reflects the change in separation over the initial separation.

In the transition from ZnSb to CdSb the maximum of the valence band may or may not stay at the same point in k-space. In the following analysis, the simplest model which duplicates the experimentally observed behavior will be examined for each case, the location of the extremum staying fixed and the location changing.

The analysis of Section 4.4 lead to a model for the valence band of ZnSb and CdSb which had a single maximum located either at Γ or R in the Brillouin zone. If the location of the extremum stays fixed at Γ or R throughout the composition range, the effective mass will be determined only by the states at this point. Thus changes in the effective mass will be the direct result of changes in energy separation and momentum matrix elements for a single set of states. Using the modeling scheme outlined above and contained in Eq. (5.7), the simplest model which follows the experimental data closely contains three interacting states. The states are the valence band and two higher band states as shown in Figure 5.6. The

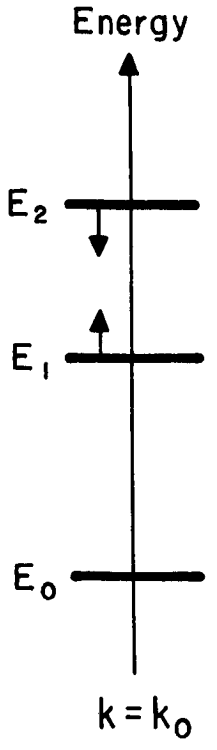

Figure 5.6. Configuration of states used in model for effective mass variation. Arrows indicate direction of movement in energy of states with increasing x.

Figure shows the position of the states for ZnSb. The arrows on the Figure indicate the direction of movement of the states upon alloying. Figures 5.7 and 5.8 show the experimental data for m_o/m_a^* and m_o/m_b^* versus composition. On each figure the curve given by the three state model is shown and the equation of the model is given. The parameters in the equations were chosen to give the best fit to both curves subject to the constraint that the denominators of the individual terms are the same for both the a and b axis. The details of the fit of theoretical to experimental variation is not important. Rather the general curvature is what was sought after, since small variations in the matrix elements with composition, taken constant in these models, could easily make the fit better. Thus a model containing two higher states interacting with the valence band state predicts an effective mass variation similar to that observed experimentally.

A model can also be made which fits the experimental data and incorporates a change in the location of the extremum in k-space. At each location in k-space Γ and R the model only requires two states to interact. Figure 5.9 shows the configuration of states at each location in k-space. For ZnSb the state E_o is the top of the valence band and E_1 is a higher state which moves away from E_o with increasing x. E_o' at the other location in k-space is the top of the valence band for CdSb and

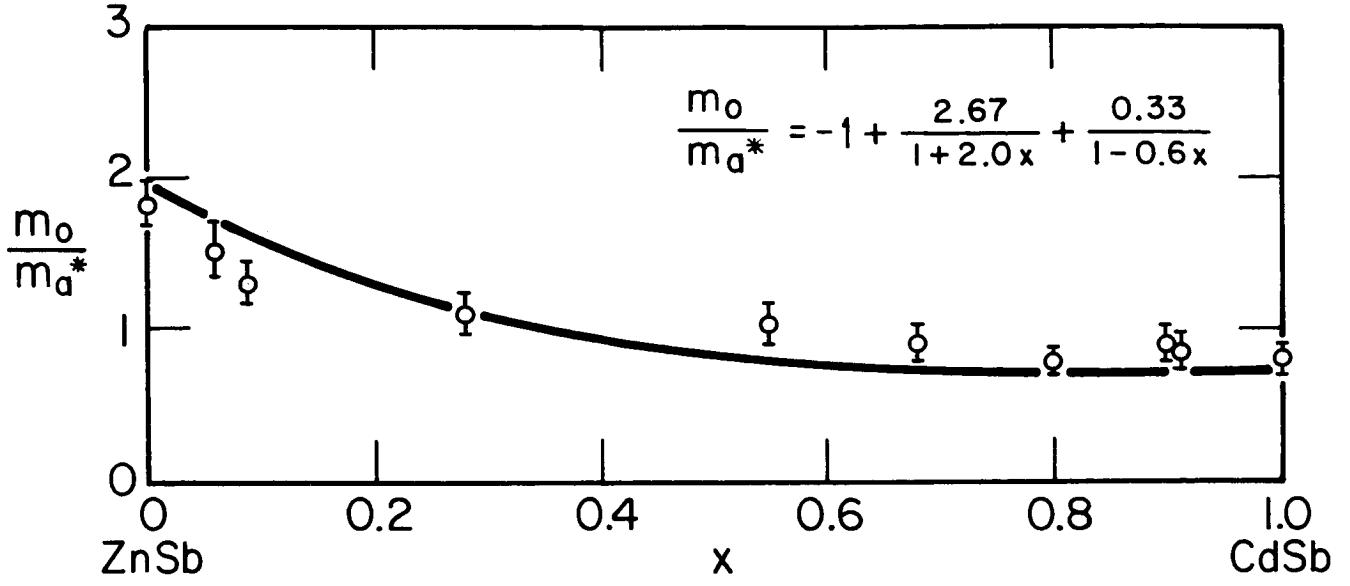

Figure 5.7. Fit of model for effective mass variation using state configuration of Figure 5.6 to experimental values for m_o/m_a^* versus x for $Cd_xZn_{1-x}Sb$.

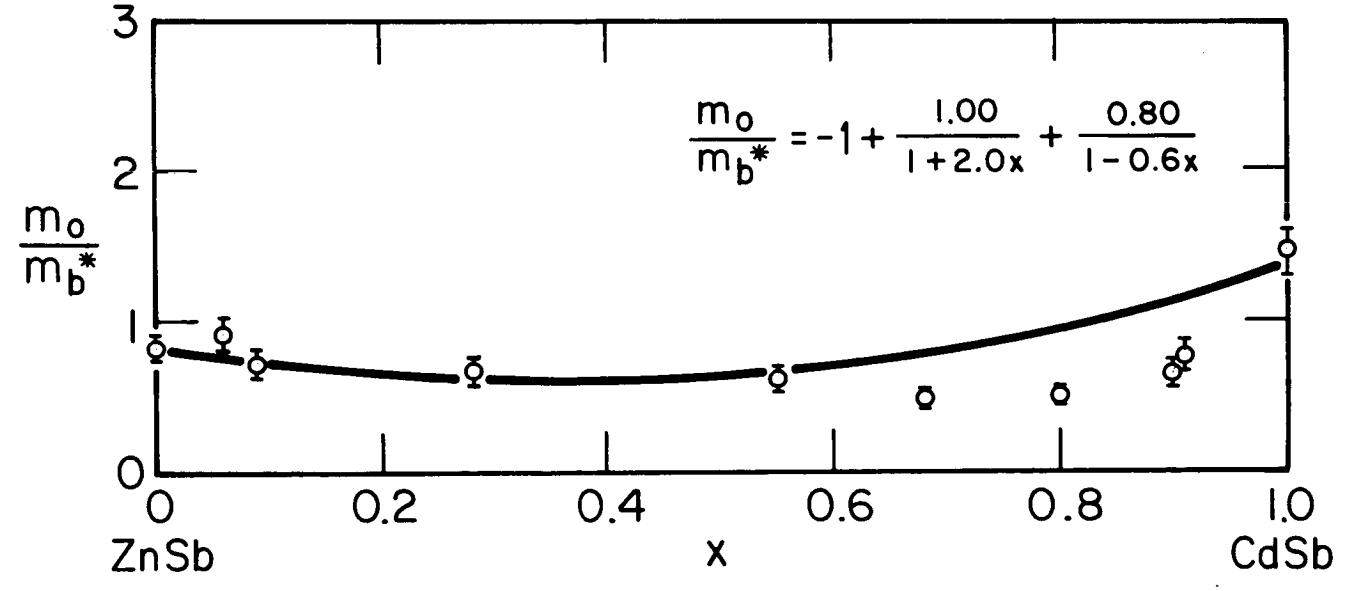

Figure 5.8. Fit of model for effective mass variation using state configuration of Figure 5.6 to experimental values for m_o/m_b^* versus x for $Cd_xZn_{1-x}Sb$.

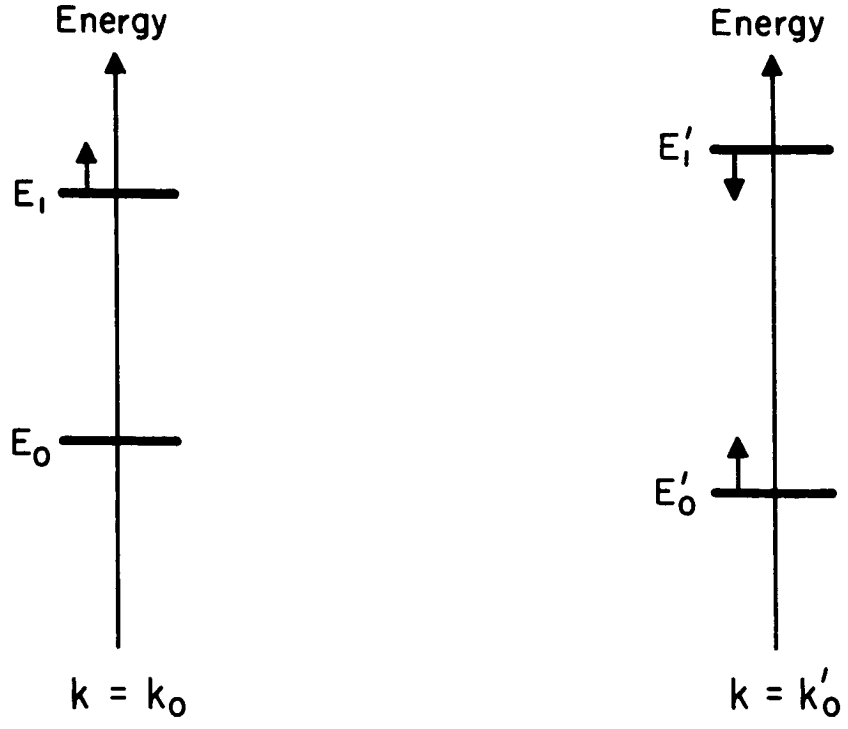

Figure 5.9. Configuration of states in k-space used in model for effective mass variation in which the valence band extremum changes with composition. Arrows indicate the direction of movement in energy of states with increasing x.

E_1' is a higher state at this same k value which moves toward E_o' with increasing x. The relative position in energy of E_o and E_o' change with composition also. Near ZnSb E_o is above E_o' and is the top of the valence band. As x increases E_o and E_o' approach each other and E_o' becomes higher than E_o. E_o' is the top of the valence band for CdSb. For the small composition range where $E_o \approx E_o'$ the valence band will have two types of holes. The observed reciprocal effective mass will be an average of the reciprocal masses of the two extrema weighted by a Boltzmann occupation factor.

Figures 5.10 and 5.11 show the experimental data for m_o/m_a^* and m_o/m_b^* versus composition. Also each Figure shows the effective mass variations predicted by a model such as shown in Figure 5.9 with parameters chosen to fit the experimental data. The best fit is obtained when the valence band changes position in k-space at $x = 0.85$ and an average of the two predicted masses are used for $0.80 < x < 0.90$.

The situation just described could also occur at the same point in k-space. In this case, the valence band state would change with composition as depicted in Figure 5.12. E_o and E_o' would be non-interacting by parity and both would interact with a single higher state. By suitable movement of the states in energy with composition the situation described in Figures 5.10 and 5.11 could be duplicated.

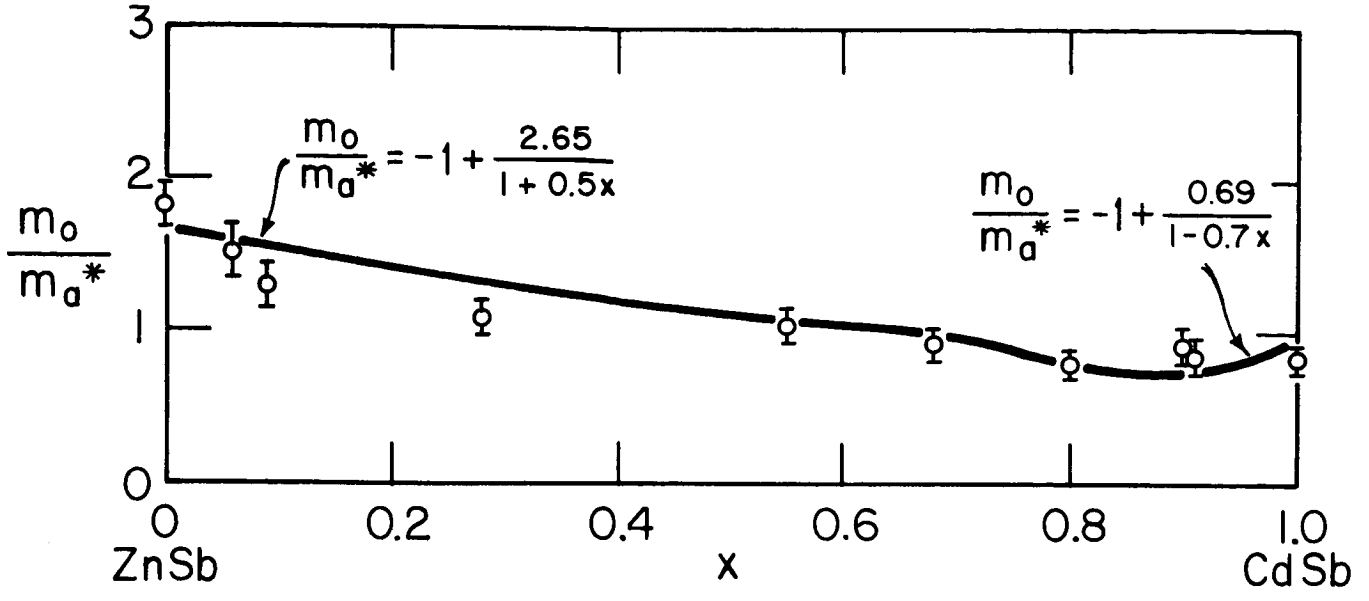

Figure 5.10. Fit of model for effective mass variation using state configuration of Figure 5.9 to experimental values for m_o/m_a^* versus x for $Cd_xZn_{1-x}Sb$.

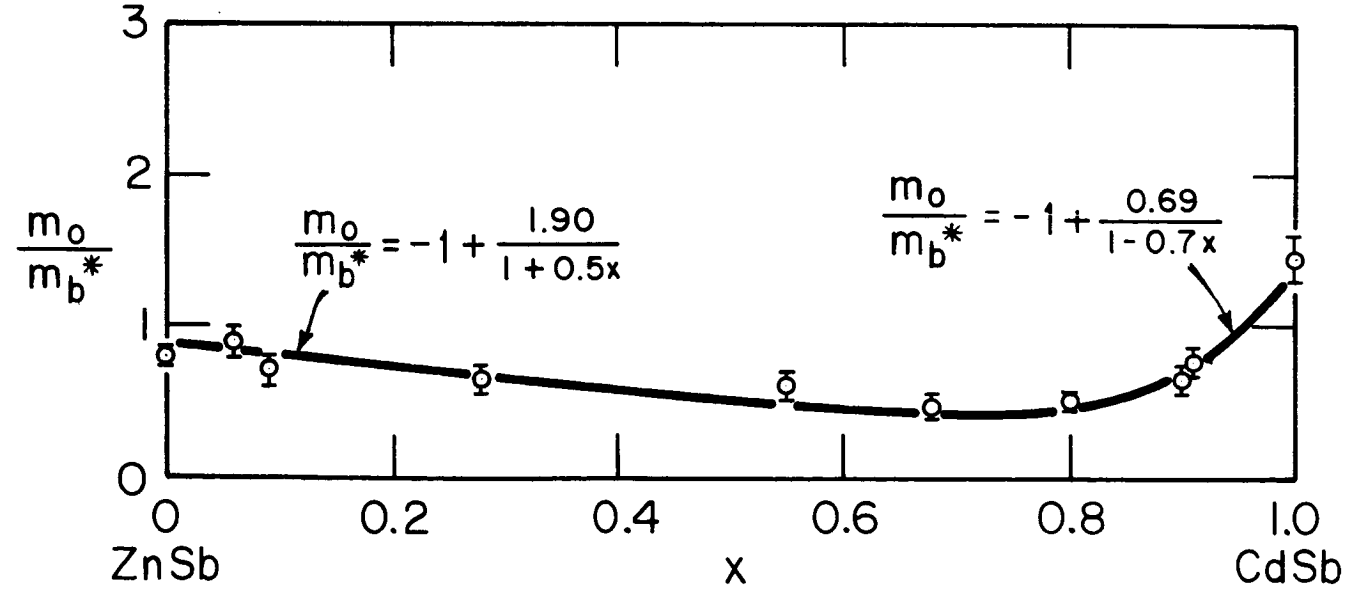

Figure 5.11. Fit of model for effective mass variation using state configuration of Figure 5.9 to experimental values for m_o/m_b^* versus x for $Cd_xZn_{1-x}Sb$.

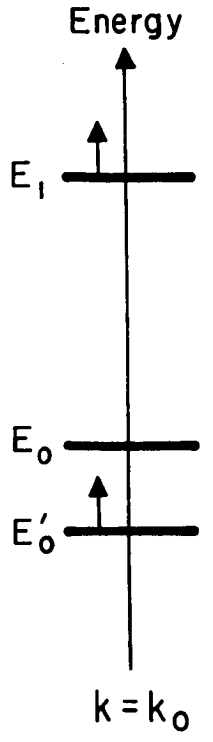

Figure 5.12. Configuration in k-space of states which will give same behavior of effective masses with composition as portrayed in Figures 5.10 and 5.11. Arrows indicate the direction of movement in energy of states with increasing x.

The analysis has shown that effective mass variations similar to those observed experimentally can be obtained with very simple models. The point of this discussion has been to show that the variations of effective mass with composition obtained experimentally are in no way unreasonable.

REFERENCES

1. L. Nordheim, Ann. Phys., 9, 607 (1931).

2. F. Bassani and D. Brust, Phys. Rev., 131, 1524 (1963).

3. E. Kane, Phys. Chem. Solids, 1, 82 (1956).

4. E. Kane, Phys. Chem. Solids, 1, 249 (1956).

5. C. Kittel, "Quantum Theory of Solids", p. 186, Wiley, New York (1963).

6. S. Rabii, "An Investigation of Energy Band Structure and Electronic Properties of Lead Sulfide and Lead Selenide", Ph.D. Thesis, M.I.T. (1966).

CHAPTER VI. SUMMARY AND RECOMMENDATIONS FOR FUTURE WORK

6.1 Summary

The aim of this work has been to study the free carrier absorption in ZnSb, CdSb, and their alloys and to use the resulting data to study the effective masses and the relaxation times. The valence band effective masses of ZnSb and CdSb were determined for the first time in the course of this work. Also an anisotropic relaxation time was observed in these materials for the first time. The alloy data represents the first determination of effective mass across any entire alloy composition range as well as for the $Cd_xZn_{1-x}Sb$ system. The behavior of a relaxation time anisotropy with alloy composition has not previously been observed either. In the following, a summary of this work will be given.

In Chapter II, the growth of single crystal ingots of p-type ZnSb, CdSb, and $Cd_xZn_{1-x}Sb$ by a horizontal zone method was described. The material was fabricated into oriented optical and electrical samples. The optical samples were used to measure the refractive indices and free carrier absorption. The electrical samples were used to measure the electrical conductivity and Hall effect.

Chapter III described the measurement techniques and methods employed. The refractive indices were determined by utilizing two interference phenomena. The absorption

coefficients were obtained from transmission measurements taken on polished samples. Electromagnetic radiation linearly polarized along a sample crystallographic axis and rendered monochromatic by means of a spectrometer was utilized for the transmission measurements. The electrical measurements were made at 30 cps to minimize thermoelectric effects.

In Chapter IV the experimental results for ZnSb and CdSb are presented. The components of the refractive index tensor were found to be independent of wavelength λ for λ between 3 and 15 μ. For ZnSb the refractive indices obtained are $n_a = 4.51 \pm 0.05$, $n_b = 4.25 \pm 0.04$, and $n_c = 4.30 \pm 0.04$, while for CdSb the refractive indices are $n_a = 4.70 \pm 0.05$, $n_b = 4.46 \pm 0.04$, and $n_c = 4.56 \pm 0.05$. The transmission of infrared radiation of wavelength between 3 and 15 μ was measured for each axis of the two materials. The absorption coefficient was then obtained from the transmission data. In the wavelength range of 7 to 15 μ, the absorption coefficient varied linearly with both λ^2, the wavelength squared, and p, the carrier concentration. The dominant absorption mechanism was identified as free carrier absorption. The Hall coefficient and electrical conductivity of each axis was measured on samples fabricated from material originally adjacent to each optical sample slice. In this way the free carrier absorption, electrical conductivity, and Hall coefficient were known for the same region of material.

Then the effective mass values were extracted from the experimental data. The reduction of the data was aided by knowledge of the directions of the principal axes of the valence band constant energy ellipsoids and by the form and energy dependence of the relaxation time tensor. This information was obtained from the data of others. For ZnSb the hole effective masses obtained are $m_a^*/m_o = 0.55 \pm 0.06$, $m_b^*/m_o = 1.23 \pm 0.12$, and $m_c^*/m_o = 0.34 \pm 0.03$. Similarly for CdSb, the hole effective masses obtained are $m_a^*/m_o = 1.26 \pm 0.13$, $m_b^*/m_o = 0.69 \pm 0.07$, and $m_c^*/m_o = 0.44 \pm 0.04$.

The relaxation time tensor in ZnSb and CdSb is known to be diagonal with a factorable energy dependence. The energy independent coefficients of the relaxation time tensor were determined from the experimental data. For both materials an anisotropic relaxation time was observed. The ratios of the relaxation time coefficients $A_a:A_b:A_c$ was 1.0 : 1.4 : 1.0 for ZnSb and 3.3 : 2.5 : 1.0 for CdSb.

Using the effective masses determined from the experimental data, the theoretical thermoelectric power for ZnSb and CdSb was calculated. The values for a single ellipsoid agreed quite well with the experimental values of thermoelectric power from the literature. Although this is not concrete evidence that both materials have a single extremum in their valence band, it suggests strongly that they do. From group theoretical

discussions in the literature, the single extremum will be nondegenerate except for spin and will be located in k-space at Γ, the origin, or R, the (111) corner of the Brillouin zone. The experimental data thus leads to a simple, single extremum, nondegenerate valence band with ellipsoidal constant energy surfaces having their principal axes along the crystal axes for both ZnSb and CdSb.

In Chapter V the measurements made on the a and b axes for the entire alloy composition range were presented. The free carrier absorption, electrical conductivity, and Hall coefficient were measured for each axis at each of eight alloy compositions. Because the alloy disorder scattering has the same energy dependence as acoustic phonon scattering, the relaxation time tensor has a factorable energy dependence for the alloys. Thus it was possible to extract the effective masses and relaxation time coefficients for the alloys in the same manner as for the pure compounds. Both of these quantities were obtained for the a and b axes across the composition range.

From the ratio of the relaxation time coefficients A_a/A_b, the anisotropy of scattering versus alloy composition could be studied. The scattering was found to be anisotropic for samples of $Cd_xZn_{1-x}Sb$ when $0 \leqslant x < 0.1$ and when $0.9 < x \leqslant 1.0$. Over the rest of the alloy composition range, the scattering was isotropic. This behavior is what would be expected if anisotropic

acoustic phonon scattering were dominant for low alloy concentrations and isotropic disorder scattering were dominant for all other concentrations.

The valence band effective mass parameters for the a and b axes were obtained as a function of composition for the alloy system. The quantity m_b^*/m_o rose rapidly with increasing x for $Cd_xZn_{1-x}Sb$ and then fell sharply near x = 1 or CdSb. The quantity m_a^*/m_o varied more gradually from ZnSb to CdSb. In fact, the deviation from a linear variation is quite small.

The band structure of ZnSb and CdSb are both unknown and complex. This makes further discussion of the alloy data difficult. A rigorous model cannot be set forth to account for the effective mass variations with composition. However, in Section 5.4 a few very oversimplified models were discussed in an effort to show that such changes as were observed represent plausible variations of effective mass with composition.

This completes a summary of the work discussed in this report. The following section will give some recommendations for future work.

6.2 Recommendations for Future Work

In future work on p-type ZnSb or CdSb it would be advantageous to use lightly doped material with the hole concentration about 10^{17}. This would eliminate the problems of excess carrier

generation encountered when the samples are heated. In ZnSb a good experiment would be to measure the speed of sound along each axis. Then the anisotropies in the hole relaxation time could be checked for correlation with the sound velocities through the formulas for acoustic phonon scattering. A similar experiment could be performed on CdSb as well.

CdSb can be made n-type at room temperature whereas ZnSb cannot. A study analogous to the one performed here on p-type CdSb could be repeated on n-type material. The electron effective masses could then be checked with those obtained by Stevenson[1] from cyclotron resonance. The anisotropy of the electron relaxation time should be similar to that of the hole relaxation time observed here if the scattering of electrons is predominantly by acoustic phonons.

In growing alloy samples for measurement care should be taken to eliminate the composition gradients which occurred in this work. This can be done by having the material in the molten zone of one composition and all other solid material another composition. The compositions of solid and melt must be chosen as those which can be held in equilibrium from the solidus-liquidus curves of the ZnSb-CdSb pseudobinary system.

The structure of the absorption edge versus composition would make an interesting study. This would provide some information on the movement and locations of the various extrema

in k-space. The energy gap versus composition would be an important result of such a study. The sound velocity along each axis of the alloy system could be measured versus composition. This would yield some basic information on the behavior of alloys as well as the specific anisotropies which occur for this system.

REFERENCES

1. M. J. Stevenson, Proc. of the Int. Conf. on Semiconductor Physics, Prague, 1960, p. 1083.

APPENDIX 1: Faraday Effect in ZnSb or CdSb

The Faraday effect or Faraday rotation has been observed in many cubic semiconductors and along the c-axis, an optic axis, in hexagonal semiconductors. The conventional experimental setup consists of a d-c magnet, a monochromator, two polarizers and a detector. Linearly polarized monochromatic radiation is directed along the magnetic field and normal to the front face of the semiconductor sample which is generally in the form of a polished slice. The second polarizer is rotated in the transmitted beam behind the sample for transmission maximum. The angular difference between the first polarizer and the second polarizer or analyzer is recorded as the Faraday rotation. In the following discussion, the Faraday effect will be derived and analyzed for an orthorhombic semiconductor, in particular, ZnSb or CdSb.

For the propagation of electromagnetic waves in a crystal Maxwell's equations may be written as

$$\text{curl}\ \vec{E} = -\frac{\partial}{\partial t}\overleftrightarrow{\mu}\vec{H}_1 \tag{A1.1}$$

$$\text{curl}\ \vec{H}_1 = \frac{\partial}{\partial t}\ \overleftrightarrow{\varepsilon}_L\ \vec{E} + \overleftrightarrow{\sigma}\cdot\vec{E}. \tag{A1.2}$$

In these equations $\vec{E}$ and $\vec{H}_1$ are the electric and magnetic field vectors of an electromagnetic wave. The electric permittivity and magnetic susceptibility tensors are given by $\overleftrightarrow{\varepsilon}_L$

and $\overleftrightarrow{\mu}$, respectively. For this analysis $\overleftrightarrow{\varepsilon}_L$ will be considered a real tensor, that is only absorption due to the electrical conductivity will be considered, and $\overleftrightarrow{\mu}$ will be taken equal to μ_o, the magnetic susceptibility of free space. The complex conductivity tensor has been written as $\overleftrightarrow{\sigma}$. The electric field can be written as the real part of a traveling wave as

$$\vec{E}(r,t) = \vec{E} \exp\ (i\omega t - \vec{\Gamma} \cdot \vec{r}) \qquad \text{(A1.3)}$$

where ω is the angular frequency of the wave, $\vec{\Gamma}$ is a complex propagation vector, and r is a position vector. Then using the form (A1.3) for $\vec{E}$, $\vec{H}_1$ can be eliminated from (A1.1) and (A1.2) to yield

$$-\Gamma^2 \vec{E} + \vec{\Gamma}\ (\vec{\Gamma} \cdot \vec{E}) = \omega^2 \overleftrightarrow{\varepsilon}_L \mu_o \vec{E} - i\omega\mu_o \overleftrightarrow{\sigma} \cdot \vec{E}. \qquad \text{(A1.4)}$$

For an orthorhombic crystal, the electric permittivity has the form

$$\overleftrightarrow{\varepsilon}_L = \begin{pmatrix} \varepsilon_1 & 0 & 0 \\ 0 & \varepsilon_2 & 0 \\ 0 & 0 & \varepsilon_3 \end{pmatrix} \qquad \text{(A1.5)}$$

with respect to the principal crystal axes. Also, to first order in the d.c. magnetic field and for $\vec{H}$, the applied d.c. field, along the 3 axis, the conductivity tensor has the form

$$\overleftrightarrow{\sigma} = \begin{pmatrix} \sigma_{11} & \sigma_{12} & 0 \\ -\sigma_{12} & \sigma_{22} & 0 \\ 0 & 0 & \sigma_{33} \end{pmatrix}. \tag{A1.6}$$

From conventional transport theory for a p-type semiconductor with an ellipsoidal constant energy surface having principal axes in directions 1, 2, and 3, one obtains

$$\sigma_{ii} = \frac{pe^2}{m_i^*} \left\langle \frac{1}{\nu_i + i\omega} \right\rangle \tag{A1.7}$$

and

$$\sigma_{ij} = \frac{pe^3}{m_i^* m_j^*} \left\langle \frac{1}{(\nu_i + i\omega)(\nu_j + i\omega)} \right\rangle \mu_o H. \tag{A1.8}$$

In (A1.7) and (A1.8) p is the hole concentration, e the magnitude of an electronic charge, m_i^* the effective mass in the i^{th} direction, ν_i the collision frequency in the i^{th} direction and $\langle\ \rangle$ indicates a suitable average over energy for $\nu_i(E)$. At infrared frequencies ν_i is generally much less than ω and Eqs. (A1.7) and (A1.8) may be approximated by

$$\text{Imag. } \sigma_{ii} \approx \frac{pe^2}{m_i^* \omega} \tag{A1.9}$$

$$\text{Real } \sigma_{ij} \approx \frac{pe^3}{m_i^* m_j^*} \left(\frac{1}{\omega^2}\right) \mu_o H \tag{A1.10}$$

where Imag. and Real indicate the imaginary and real parts of, respectively.

For the traveling wave (A1.3) form for $\vec{E}$ and a similar form for $\vec{H}_1$, Maxwell's equations become in the crystal

$$\vec{\Gamma} \times \vec{E} = i\omega\mu_o \vec{H}_1 \tag{A1.11}$$

$$-\vec{\Gamma} \times \vec{H}_1 = i\omega \overleftrightarrow{\varepsilon}_L \vec{E} + \overleftrightarrow{\sigma}\vec{E} = i\omega \left(\overleftrightarrow{\varepsilon}_L - \frac{i\overleftrightarrow{\sigma}}{\omega} \right) E \tag{A1.12}$$

$$\text{div } \overleftrightarrow{\varepsilon}_L \vec{E} = 0 \tag{A1.13}$$

$$\text{div } \mu_o \vec{H} = 0. \tag{A1.14}$$

Taking the dot product of $\vec{\Gamma}$ with Eq. (A1.12) one obtains

$$\vec{\Gamma} \cdot \left(\overleftrightarrow{\varepsilon} - \frac{i\overleftrightarrow{\sigma}}{\omega} \right) \vec{E} = 0. \tag{A1.15}$$

For an orthorhombic material with a d.c. magnetic field in the 3 direction, to first order in the magnetic field, one has

$$\left(\overleftrightarrow{\varepsilon}_L - \frac{i\overleftrightarrow{\sigma}}{\omega} \right) = \begin{pmatrix} \varepsilon_1 - \frac{i\sigma_{11}}{\omega} & -\frac{i\sigma_{12}}{\omega} & 0 \\ +\frac{i\sigma_{12}}{\omega} & \varepsilon_2 - \frac{i\sigma_{22}}{\omega} & 0 \\ 0 & 0 & \varepsilon_3 - \frac{i\sigma_{33}}{\omega} \end{pmatrix}. \tag{A1.16}$$

For waves propagating down the 3 axis, $\Gamma_1 = \Gamma_2 = 0$ and from Eq. (A1.15)

$$\Gamma_3 \left(\varepsilon_3 - \frac{i\sigma_{33}}{\omega} \right) E_3 = 0. \tag{A1.17}$$

Since $\left(\varepsilon_3 - \frac{i\sigma_{33}}{\omega}\right)$ does not have both its real and imaginary parts equal to zero, E_3 must be zero. Then for this type wave $\vec{\Gamma} \cdot \vec{E} = 0$ in Eq. (A1.4).

In the Faraday configuration it is this type of wave, that is waves with $\vec{\Gamma}$ in the 3 direction, that are excited in the crystal. Linearly polarized plane waves are incident normally on the crystal so that in free space E_1 and E_2 can be non-zero while E_3 must be zero. To determine the modes that are excited in the crystal a boundary value problem must be solved at the interface to insure that Maxwell's equations are satisfied. The components of $\vec{E}$ tangential to the interface E_1 and E_2 must be continuous across the boundary so that E_1 and E_2 can be non-zero in the crystal. Since there is no surface charge on the crystal the normal component of $\overleftrightarrow{\varepsilon}\vec{E}$ must be continuous. Thus since E_3 is zero on the air side of the interface E_3 must be zero in the crystal also. Then the Faraday experimental configuration is capable of exciting plane waves in the crystal which propagate along the 3 axis such that $\vec{\Gamma} \cdot \vec{E} = 0$. This statement cannot be made for arbitrary directions of propagation in the crystal.

Then substituting Eqs. (A1.5) and (A1.6) into Eq. (A1.4), for the special case $\vec{\Gamma} \cdot \vec{E} = 0$, yields the following equations for E_1 and E_2 the electric field components of interest.

$$(\Gamma^2 + \omega^2\varepsilon_1\mu_o - i\omega\,\mu_o\sigma_{11})E_1 - i\omega\,\mu_o\sigma_{12}E_2 = 0 \qquad \text{(A1.18)}$$

$$i\omega\,\mu_o\sigma_{12}E_1 + (\Gamma^2 + \omega^2\varepsilon_2\mu_o - i\omega\,\mu_o\sigma_{22})E_2 = 0. \qquad \text{(A1.19)}$$

Setting the determinant of the coefficients of E_1 and E_2 equal to zero yields a secular equation for Γ^2 which is

$$\Gamma^4 + \omega\,\mu_o\left[\omega(\varepsilon_1 + \varepsilon_2) - i(\sigma_{11} + \sigma_{22})\right]\Gamma^2 + \omega^2\mu_o^2\left[(\omega\varepsilon_1 - i\sigma_{11})(\omega\varepsilon_2 - i\sigma_{22}) - \sigma_{12}^2\right] = 0. \qquad \text{(A1.20)}$$

Solving Eq. (A1.20) for Γ^2 yields

$$\Gamma^2 = -\omega\,\mu_o\left[\omega\left(\frac{\varepsilon_1 + \varepsilon_2}{2}\right) - i\left(\frac{\sigma_{11} + \sigma_{22}}{2}\right)\right] \pm \omega\,\mu_o\left\{\left[\frac{\omega(\varepsilon_1 - \varepsilon_2)}{2} - i\,\frac{(\sigma_{11} - \sigma_{22})}{2}\right]^2 + \sigma_{12}^2\right\}^{1/2} \qquad \text{(A1.21)}$$

For a cubic crystal $\sigma_{11} = \sigma_{22}$ and $\varepsilon_1 = \varepsilon_2$ by symmetry and Eq. (A1.21) reduces to

$$\Gamma^2 = -\omega\,\mu_o\,[\omega\varepsilon_1 - i\sigma_{11} \pm \sigma_{12}] \qquad \text{(A1.22)}$$

Upon substituting this expression for Γ^2 into Eq. (A1.18) or (A1.19), one finds that the polarizations corresponding to these solutions are

$$E_1 = \pm\, i\, E_2. \qquad \text{(A1.23)}$$

These solutions correspond to right and left circularly polarized waves, respectively. At frequencies corresponding to

infrared radiation, the displacement current term $\omega\varepsilon_1$ in Eq. (A1.22) is usually much greater than the conduction terms σ_{11} and σ_{12}. Then Eq. (A1.22) can be expanded to give an approximate expression for $\Gamma_{\pm}$

$$\Gamma_{\pm} = i\omega\sqrt{\mu_o\varepsilon_1}\left[1 - \frac{i\sigma_{11}}{2\omega\varepsilon_1} \pm \frac{\sigma_{12}}{2\omega\varepsilon_1}\right] \qquad (A1.24)$$

$$= \alpha_{\pm} + i\beta_{\pm} .$$

The right and left circularly polarized waves will have different propagation constants β_+ and β_-, respectively. Neglecting attenuation, a linearly polarized beam incident normally on the sample and parallel to the d.c. magnetic field will have its plane of polarization rotated as a result of passage through the sample by an angle θ given by

$$\theta = \left(\frac{\beta_+ - \beta_-}{2}\right) d = - \sqrt{\frac{\mu_o}{\varepsilon_1}}\left[\text{Re } \sigma_{12}\right] d \qquad (A1.25)$$

where Re σ_{12} is the real part of σ_{12} and d is the thickness of the sample. For a semiconductor like Ge or Si, θ is about 2π radians per cm or more. The real part of σ_{12} from Eq. (A1.10) is directly proportional to both H and $1/\omega^2 = (2\pi)^2\,\lambda^2/c^2$. Thus for the cubic case θ varies linearly with H the applied magnetic field strength and λ^2 the wavelength of the electromagnetic radiation squared.

For the case of an orthorhombic semiconductor the relative magnitude of the terms in Eq. (A1.21) must be investigated. Then the expression for Γ^2 may be appropriately expanded to yield approximate analytic solutions for Γ. This will be done in the following sections.

At infrared frequencies ν_i is generally much less than ω and Eqs. (A1.7) and (A1.8) may be approximated for CdSb and ZnSb as

$$\sigma_{11} \approx \frac{pe^2}{m_1}\left(\frac{1}{\omega}\right) \approx 6(\text{ohm} - \text{m})^{-1} \tag{A1.26}$$

$$\sigma_{12} \approx \frac{pe^3}{m_1 m_2}\left(\frac{1}{\omega^2}\right)\mu_o H \approx (8.6 \times 10^{-3})\,\mu_o H\ (\text{ohm} - \text{m})^{-1}. \tag{A1.27}$$

In evaluating σ_{11} and σ_{22} the following approximate values for the parameters relative to CdSb and ZnSb have been used

$$m_1 \approx 2\ m_2 \approx 1.2\ m_o$$

$$p = 5 \times 10^{16}\ \text{cm}^{-3}$$

$$\omega = 2 \times 10^{14}\ \text{rad/sec or } \lambda = 10\mu \text{ in free space.}$$

The above values are representative of the parameter values obtained in the experimental phase of this work. In addition, $\omega\varepsilon_i$ will be about $3.6 \times 10^4\ (\text{ohm} - \text{m})^{-1}$ for the above value of ω and $\varepsilon_i \approx 20\ \varepsilon_o$, a reasonable value for ZnSb or CdSb.

The anisotropies in ZnSb and CdSb are such that one can expect

$$\frac{|\varepsilon_1 - \varepsilon_2|}{\varepsilon_1} \approx 5\%$$

$$\frac{|\sigma_{11} - \sigma_{22}|}{\sigma_{11}} \approx 50\%.$$

Then for a magnetic field of 2 webers/m^2 one can expect the terms in the latter part of Eq. (A1.21) to have the approximate values

$$\frac{\omega(\varepsilon_1 - \varepsilon_2)}{2} \approx 9 \times 10^2 \text{ (ohm - m)}^{-1}$$

$$\frac{\sigma_{11} - \sigma_{22}}{2} \approx 3 \text{ (ohm - m)}^{-1}$$

$$\sigma_{12} \approx (1.7 \times 10^{-2}) \text{ (ohm - m)}^{-1}.$$

Thus σ_{12} will be much smaller than the other terms.

Considering the magnitude of the terms involved Eq. (A1.21) can be written as

$$\Gamma_{\pm}^2 = -\omega \mu_o \left\{ \left[\frac{\omega(\varepsilon_1+\varepsilon_2)}{2} - \frac{i(\sigma_{11}+\sigma_{22})}{2} \pm \frac{\omega(\varepsilon_1-\varepsilon_2)}{2} - \frac{i(\sigma_{11}-\sigma_{22})}{2} \right] \right.$$
$$\left. \pm \left[\frac{\sigma_{12}}{\omega(\varepsilon_1-\varepsilon_2) - i(\sigma_{11}-\sigma_{22})} \right] \right\}. \quad \text{(A1.28)}$$

The two solutions can be written more compactly as

$$\Gamma_+^2 = -\omega \mu_o \left[\omega\varepsilon_1 - i\sigma_{11} + \frac{\sigma_{12}^2}{\omega(\varepsilon_1-\varepsilon_2) - i(\sigma_{11}-\sigma_{22})} \right] \quad \text{(A1.29)}$$

and

$$\Gamma_-^2 = -\omega\mu_o\left[\omega\varepsilon_2 - i\sigma_{22} - \frac{\sigma_{12}^2}{\omega(\varepsilon_1-\varepsilon_2) - i(\sigma_{11}-\sigma_{22})}\right] . \quad \text{(A1.30)}$$

Now these solutions may be plugged into Eqs. (A1.18) or (A1.19) to determine the polarizations corresponding to the two solutions (A1.29) and (A1.30). This yields for the + sign

$$E_2 = -i\left[\frac{\sigma_{12}}{\omega(\varepsilon_1-\varepsilon_2) - i(\sigma_{11}-\sigma_{22})}\right] E_1 \quad \text{(A1.31)}$$

and for the - sign

$$E_1 = i\left[\frac{\sigma_{12}}{\omega(\varepsilon_1-\varepsilon_2) - i(\sigma_{11}-\sigma_{22})}\right] E_2. \quad \text{(A1.32)}$$

In each case the coefficient in Eqs. (A1.31) or (A1.32) will be of the order of 10^{-5} so that for all practical purposes the modes of propagation correspond to two linearly polarized waves. One solution coming from Eq. (A1.29) where the lead terms involve ε_1 and σ_{11} corresponds to the E vector polarized in the 1 direction. The other solution coming from Eq. (A1.30) where the lead terms involve ε_2 and σ_{22} corresponds to the E vector polarized in the 2 direction. These modes are almost identical to those which can propagate independently in the absence of a d.c. magnetic field. Thus the magnetic field does not greatly alter the polarization modes that propagate

independently in the absence of the static magnetic field.

Because of the small magnitude of the last terms relative to the first terms in Eqs. (A1.29) and (A1.30), one can use an expansion to give an approximate analytical expression for Γ_+ and Γ_-. The following expressions are then obtained.

$$\Gamma_+ = i\left\{\omega\sqrt{\mu_o\left(\varepsilon_1 - \frac{i\sigma_{11}}{\omega}\right)} + \frac{\sigma_{12}^2\,\mu_o\omega}{2\omega\sqrt{\mu_o\left(\varepsilon_1 - \frac{i\sigma_{11}}{\omega}\right)}\left[\omega(\varepsilon_1-\varepsilon_2) - i\,(\sigma_{11}-\sigma_{22})\right]}\right\} \tag{A1.33}$$

$$\Gamma_- = i\left\{\omega\sqrt{\mu_o\left(\varepsilon_2 - \frac{i\sigma_{22}}{\omega}\right)} + \frac{\sigma_{12}^2\,\mu_o\omega}{2\omega\sqrt{\mu_o\left(\varepsilon_2 - \frac{i\sigma_{22}}{\omega}\right)}\left[\omega(\varepsilon_1-\varepsilon_2) - i\,(\sigma_{11}-\sigma_{22})\right]}\right\}. \tag{A1.34}$$

By neglecting the conduction component of the current relative to the displacement component in the denominator of Eqs. (A1.33) and (A1.34) the expressions for Γ_+ and Γ_- may be simplified to

$$\Gamma_+ = i\left\{\omega\sqrt{\mu_o\left(\varepsilon_1 - \frac{i\sigma_{11}}{\omega}\right)} + \frac{\sigma_{12}^2\,\mu_o}{2\omega(\varepsilon_1-\varepsilon_2)\sqrt{\mu_o\varepsilon_1}}\right\} \tag{A1.35}$$

and

$$\Gamma_- = i\left\{\omega\sqrt{\mu_o\left(\varepsilon_2 - \frac{i\sigma_{22}}{\omega}\right)} - \frac{\sigma_{12}^2\,\mu_o}{2\omega(\varepsilon_1-\varepsilon_2)\sqrt{\mu_o\varepsilon_2}}\right\}. \qquad \text{(A1.36)}$$

As in the cubic case the + and - solutions will have different propagation constants β_+ and β_- i.e., the imaginary parts of Γ_+ and Γ_- will differ. In this case the polarization modes are not right and left circularly polarized waves, but rather the + wave is linearly polarized in the 1 direction and the - wave is linearly polarized in the 2 direction. The phase difference between the two waves will be given by

$$\Phi = \beta_+ - \beta_- = \omega\sqrt{\mu_o}\ \mathrm{Re}\left[(\varepsilon_1-\varepsilon_2) - \frac{i}{\omega}(\sigma_{11}-\sigma_{22})\right]$$

$$+\frac{\sigma_{12}^2\,\mu_o}{2\omega(\varepsilon_1-\varepsilon_2)\sqrt{\mu_o\varepsilon_1}} + \frac{\sigma_{12}^2\,\mu_o}{2\omega(\varepsilon_1-\varepsilon_2)\sqrt{\mu_o\varepsilon_2}}\,. \qquad \text{(A1.37)}$$

On substituting reasonable values for the parameters in the term involving σ_{12} in Eq. (A1.37), one finds

$$\frac{\sigma_{12}^2\,\mu_o}{2\omega(\varepsilon_1-\varepsilon_2)\sqrt{\mu_o\varepsilon_1}} \approx \frac{\sigma_{12}^2\,\mu_o}{2\omega(\varepsilon_1-\varepsilon_2)\sqrt{\mu_o\varepsilon_2}} \approx 0.37\ B^2\lambda\ (m^{-1})$$

where λ is the free space wavelength of the radiation in meters and B is the magnetic flux density in webers/m^2. For $\lambda = 10\ \mu$ and B = 3 webers/m^2 the phase difference between the +

and - waves which is due to the magnetic field is

$$\Phi_B = \frac{\sigma_{12}^2 \mu_o}{\omega(\varepsilon_1-\varepsilon_2)\sqrt{\mu_o \varepsilon_1}} \approx 3.3 \times 10^{-5}/\text{meter}$$

$$= 3.3 \times 10^{-8}/\text{mm}.$$

On the other hand the phase difference which is due to the anisotropic dielectric constant is approximately

$$\omega\sqrt{\mu_o(\varepsilon_1-\varepsilon_2)} \approx 7 \times 10^{+5}/\text{m}$$

for $\lambda = 10\ \mu$. Thus a large rotation of the plane of polarization will be caused by the anisotropy of the material through $\varepsilon_1 \neq \varepsilon_2$. The additional rotation caused by the magnetic field will be so small as to be virtually unobservable for reasonable magnetic fields and sample thicknesses. It is also to be noted that β_+ and β_- vary quadratically with the static magnetic field rather than linearly as in the conventional Faraday rotation.

Thus the calculations have shown that the anisotropy of the dielectric constant virtually swamps out the magnetic field dependence of the propagation of electromagnetic radiation in the crystal. It is impossible to obtain an observable Faraday effect in either ZnSb or CdSb unless one propagates down an optic axis. For propagation down an optic axis the dielectric

constant will be isotropic in the plane perpendicular to the optic axis. While this eliminates the anisotropy in ε, the conductivity anisotropy will remain to still mask the Faraday effect. In addition the optic axes would be difficult to locate experimentally. Also their location would probably be temperature dependent. In conclusion the Faraday effect in CdSb or ZnSb does not seem a practical experiment to perform.

APPENDIX 2: Free Carrier Absorption

The electrical conductivity of a semiconductor leads to a loss mechanism for electromagnetic radiation known as free carrier absorption. This phenomenon is the optical analog of the electrical conductivity in the same sense that the Faraday effect is the optical analog of the Hall effect. Quantum mechanically, free carrier absorption corresponds to excitation of electrons between states in the same band. Thus free carrier absorption is an intraband phenomena. In this discussion the expressions for free carrier absorption will be derived for a semiconductor of orthorhombic symmetry.

The problem concerns the propagation of electromagnetic waves in a crystal and thus is similar to the problem of Appendix 1. However, the presence of a d.c. magnetic field is not considered. As a result of the form of the conductivity tensor, the problem is simpler here than in Appendix 1. The analysis leading to Eq. (A1.4) is the same for each case so that this will be repeated as a convenient starting point

$$-\nabla^2 \vec{E} + \vec{\nabla}(\vec{\nabla} \cdot \vec{E}) = \omega^2 \overleftrightarrow{\varepsilon}_L \mu_o \vec{E} - i\omega \mu_o \overleftrightarrow{\sigma} \cdot \vec{E}. \qquad \text{(A1.4)}$$

The electric permittivity tensor will be given by Eq. (A1.5) for this case also. However, the conductivity tensor will be, in the crystal axes coordinate system and without a d.c. magnetic field,

$$\overleftrightarrow{\sigma} = \begin{pmatrix} \sigma_1 & 0 & 0 \\ 0 & \sigma_2 & 0 \\ 0 & 0 & \sigma_3 \end{pmatrix} \tag{A2.1}$$

For an electric field vector $\vec{E}_o$ aligned along crystal axis i, $\vec{D}$ the electric displacement vector will be parallel to $\vec{E}_o$ from the relation $\vec{D} = \overleftrightarrow{\varepsilon}_L \vec{E}$. For an anisotropic optical medium $\vec{D}$ is not generally parallel to $\vec{E}$. However, an exception to this rule occurs when $\vec{E}$ is along a crystal axis. For a traveling wave form for $\vec{H}_1$ with a spacial dependence $e^{-\vec{\Gamma}\cdot\vec{r}}$ similar to $\vec{E}$ in Eq. (A1.3), Eq. (A1.2) can be written as

$$-\vec{\Gamma} \times \vec{H}_1 = i\omega \overleftrightarrow{\varepsilon}_L \vec{E}_o + \overleftrightarrow{\sigma} \vec{E}_o. \tag{A2.2}$$

Taking the dot product of $\vec{\Gamma}$ and Eq. (A2.2) yields

$$\vec{\Gamma} \cdot (i\omega \overleftrightarrow{\varepsilon}_L \vec{E}_o + \overleftrightarrow{\sigma} \vec{E}_o) = 0. \tag{A2.3}$$

For $\vec{E}_o$ along axis i and of magnitude E_i, Eq. (A2.3) becomes

$$\Gamma_i (i\omega\varepsilon_i + \sigma_i)E_i = 0. \tag{A2.4}$$

Since neither E_i or the real or imaginary parts of $(i\omega\varepsilon_i + \sigma_i)$ are equal to zero, the real and imaginary parts of Γ_i must both be zero. Then $\vec{\Gamma}$ is perpendicular to $\vec{E}_o$.

For the case of the electric field aligned along an axis $\vec{\Gamma} \cdot \vec{E} = 0$ and Eq. (A1.4) yields

$$(\Gamma^2 + \omega^2\varepsilon_i\mu_0 - i\omega\mu_o\sigma_i)E_i = 0. \tag{A2.5}$$

For a non-trivial solution, the coefficient of E_i in Eq. (A2.5) must be zero. This yields an expression for Γ^2

$$\Gamma^2 = - \omega\varepsilon_i \mu_o + i\omega \mu_o\sigma_i. \tag{A2.6}$$

Equation (A2.6) is the solution for the magnitude of $\vec{\Gamma}$. The direction of $\vec{\Gamma}$ remains unspecified except that it must be perpendicular to the crystal axis i. Thus for each crystal axis, radiation with its electric vector polarized parallel to the crystal axis can propagate in any direction perpendicular to that axis. The propagation properties will be determined only by the axis along which the electric vector is polarized.

The propagation vector $\vec{\Gamma}_{pi}$ for propagation with the electric field aligned along axis i can be written as

$$\vec{\Gamma}_{pi} = i\vec{\Gamma}'_{pi} + \vec{\Gamma}''_{pi} \tag{A2.7}$$

where $\vec{\Gamma}'_{pi}$ and $\vec{\Gamma}''_{pi}$ are the imaginary and real parts of $\vec{\Gamma}_{pi}$, respectively. As the wave progresses along a direction in space parallel to $\vec{\Gamma}''_{pi}$ the electric field will be attenuated by $e^{-\Gamma''_{pi}}$ per unit length. The poynting vector or power in the wave which varies as E^2 will be attenuated by $e^{-2\Gamma''_{pi}}$ per unit length. Thus the absorption coefficient defined as the attenuation in power per unit length is given by

$$\alpha_i = 2\Gamma''_{pi}. \tag{A2.8}$$

From Maxwell's equations, Eqs. (A1.1) and (A1.2), $\vec{\Gamma}_{pi}$ and $\vec{\Gamma}''_{pi}$ are both perpendicular to $\vec{E}$ and $\vec{H}_1$ and thus are parallel to one another. Then Γ^2 can be evaluated as

$$\Gamma^2 = -\Gamma'^2_{pi} + 2i\,\Gamma'_{pi}\,\Gamma''_{pi} + \Gamma''^2_{pi}. \tag{A2.9}$$

The refractive index n_i is defined by

$$\Gamma'_{pi} = \frac{\omega}{c} n_i \tag{A2.10}$$

where c is the speed of light in free space. By comparison of Eqs. (A2.6) and (A2.9) and using (A2.10), Γ''_{pi} can be expressed as

$$\Gamma''_{pi} = \frac{\text{Re } \sigma_i}{2cn_i\varepsilon_o} \tag{A2.11}$$

where ε_o is the electric permittivity of free space and Re σ_i is the real part of σ_i. Then from Eq. (A2.8), α_i can be written as

$$\alpha_i = \frac{\text{Re } \sigma_i}{cn_i\,\varepsilon_o}\,. \tag{A2.12}$$

From conventional transport theory for a p-type semiconductor with an ellipsoidal constant energy surface having principal axes along the crystal axes one obtains

$$\sigma_i = \frac{pe^2}{m_i^*}\left\langle \frac{1}{\frac{1}{\tau_i} + i\omega} \right\rangle \tag{A2.13}$$

In Eq. (A2.13), p is the hole concentration, e the electronic charge, m_i^* the effective mass in the i^{th} direction, and τ_i the relaxation time for the i^{th} direction. The brackets are defined for non-degenerate material as

$$< F(\mathcal{E}) > = \frac{\int_o^\infty F(\mathcal{E}) \mathcal{E}^{3/2} e^{-\mathcal{E}/k_B T} d\mathcal{E}}{\int_o^\infty \mathcal{E}^{3/2} e^{-\mathcal{E}/k_B T} d\mathcal{E}} \qquad \text{(A2.14)}$$

where $\mathcal{E}$ is the energy. The real part of σ_i can be extracted from Eq. (A2.13) as

$$\text{Re } \sigma_i = \frac{pe^2}{m_i^*} \left\langle \frac{\frac{1}{\tau_i}}{\frac{1}{\tau_i^2} + \omega^2} \right\rangle . \qquad \text{(A2.15)}$$

From the data of Section 4.4, $< \tau >$ will be about 10^{-13} sec., while in the near infrared $1/\omega$ will be 10^{-14} or 10^{-15}. For near infrared frequencies, $\omega^2 >> 1/\tau_i^2$ so that Eq. (A2.15) then may be approximated as

$$\text{Re } \sigma_i = \frac{pe^2}{m_i^* \omega^2} \left\langle \frac{1}{\tau_i} \right\rangle \qquad \text{(A2.16)}$$

Using Eq. (A2.16) for the real part of σ_i, the absorption coefficient α_i is from Eq. (A2.12)

$$\alpha_i = \frac{pe^2}{cn_i \varepsilon_o \omega^2 m_i^*} \left\langle \frac{1}{\tau_i} \right\rangle \qquad \text{(A2.17)}$$

or in terms of the wavelength λ of the radiation in free space

$$\alpha_i = \frac{pe^2 \lambda^2}{4\pi^2 c^3 n_i \varepsilon_o m_i^*} \left\langle \frac{1}{\tau_i} \right\rangle . \qquad \text{(A2.18)}$$

Equation (A2.18) is the form of the free carrier absorption α_i as it is used in this work. The most characteristic trait of free carrier absorption is the linear dependence of α_i on both p, the carrier concentration, and λ^2, the wavelength squared.

APPENDIX 3: Disorder Scattering in Alloys

A substitutional alloy such as $Cd_xZn_{1-x}Sb$ investigated here consists of an Sb sublattice and a disordered Cd-Zn sublattice. The following structure is assumed for the alloy system. The Sb sublattice is essentially no different from the Sb sublattice of ZnSb or CdSb. In the Cd-Zn sublattice the Cd and Zn atoms are randomly placed on sites which are regular in space. At regular points in space there are atoms. The kind of atom is what occurs randomly.

In treating such an alloy, one could consider the entire crystal as a random structure without periodicity. Then the problem would not be amenable to conventional band theory. Instead, the properties would have to be determined statistically. Nordheim[1] has suggested a "virtual crystal" approximation in which the alloy is considered to be perfectly periodic with a potential which depends on composition. The potential is taken as a suitable average over the individual potentials. Then the bands and material properties can be calculated for such a lattice. This "virtual crystal" represents the first approximation to the alloy. The disorder which is present can then be treated as a perturbation on the lattice.

Calculations made by Bassani and Brust[2] on Ge-Si alloys using the "virtual crystal" model have been quite successful in

explaining the experimental data on that alloy system. Parmenter has dealt with the alloy problem in general in several papers.[3,4,5] He predicts that upon alloying a material in low concentrations the effective masses will decrease and, if anisotropic, tend towards isotropy. Parmenter's conclusions are presently unsubstantiated either experimentally or theoretically.

The scattering of electrons due to the crystal disorder is under consideration here. In conventional, non-alloyed materials, point defects and ionized impurities can be treated as scattering centers and lead to various dependences of the relaxation time on energy. In one sense, the alloy crystal could be treated as point defects in a host crystal. This seems an overestimation of the effects of alloying. The disruption of the lattice is small since the alloy atoms have the same valency and position in the crystal as the host atoms once had. Confusion would arise near the mid-range of composition as to which crystal was the host and which atoms were the impurities.

A more satisfying approach is to consider the "virtual crystal" as a host crystal and to consider the affects of alloy disorder as a perturbation. This is the manner in which Ziman[6] has handled the problem. Consider two binary compounds, AC and BC, which form a substitutional alloy $A_xB_{1-x}C$. Let V_A, V_B, and V_C represent the atomic potentials of atom A, B, and C,

respectively. The "virtual crystal" will have a potential V_C at atomic sites on the C sublattice and a potential

$$\bar{V} = x\, V_A + (1 - x)\, V_B \tag{A3.1}$$

at an atomic site on the AB sublattice.

In the "virtual crystal" the electrons will not be scattered by the average potentials V_C and $\bar{V}$. However, in the actual crystal the electrons will be scattered by deviations of the actual potential from the average potential. Thus electrons will be scattered by both A and B atoms in the crystal. For an A atom site the deviation of the potential from the average will be

$$V_A - \bar{V} = (1 - x)(V_A - V_B) = (1 - x)\, V_{AB}. \tag{A3.2}$$

where $(V_A - V_B) = V_{AB}$. For a B atom site the deviation of the potential from the average will be

$$V_B - \bar{V} = -\, x(V_A - V_B) = -\, x\, V_{AB}. \tag{A3.3}$$

The probability that an electron will be scattered from an initial state i to a final state f is from Ziman[7]

$$P_i^f = \frac{2\pi}{\hbar} \left| < i \left| H' \right| f > \right|^2 D_f(E_i) \tag{A3.4}$$

In Eq. (A3.4), H' is the scattering potential, $< i \left| H' \right| f >$ is the matrix element of the scattering potential between initial and final states, and $D_f(E_i)$ is the density of final states

with energy equal to the initial state energy. The scattering process is assumed elastic.

First consider the term $|\langle i | H' | f \rangle|^2$. For an A site the scattering will be proportional to

$$\left| \int \psi_k^* (V_A - \bar{V}) \psi_k, \, dr \right|^2 = (1 - x)^2 \left| \int \psi_k^* V_{AB} \psi_k, \, dr \right|^2$$

$$= (1 - x)^2 \left| \langle V_{AB} \rangle \right|^2. \qquad \text{(A3.5)}$$

In Eq. (A3.5) ψ_k and ψ_k, are the wave functions of the initial and final states respectively. Also $\langle V_{AB} \rangle$ is the matrix element of the potential V_{AB} between the initial and final states. For a B site the scattering will be proportional to

$$\left| \int \psi_k^* (V_B - \bar{V}) \psi_k, \, dr \right|^2 = x^2 \left| \langle V_{AB} \rangle \right|^2. \qquad \text{(A3.6)}$$

Each A site will contribute a term proportional to Eq. (A3.5). The concentration of A sites is given by Nx, where N is the number of sites on the AB sublattice in the crystal. Thus the total contribution from the A atoms will be proportional to Nx times Eq. (A3.5) or

$$Nx \, (1 - x)^2 \left| \langle V_{AB} \rangle \right|^2. \qquad \text{(A3.7)}$$

Similarly the total contribution from the B atoms will be proportional to

$$Nx^2 \, (1 - x) \left| \langle V_{AB} \rangle \right|^2. \qquad \text{(A3.8)}$$

Thus the total scattering will be proportional to the sum of the A and B contributions or the sum of Eqs. (A3.7) and (A3.8) given by

$$\left[x^2(1-x) + x(1-x)^2\right] N \left| < V_{AB} > \right|^2 = x(1-x)\ N \left| < V_{AB} > \right|^2. \quad \text{(A3.9)}$$

Returning to Eq. (A3.4), $D_f(E_i)$ the density of final states at the electron energy E_i will be $N(E_i)$ the density of states of the energy band under consideration. Then the rate of occurence or total probability of collision will be

$$\nu(E) = \frac{2\pi x(1 - x)N}{\hbar} \left| < V_{AB} > \right|^2 N(E). \quad \text{(A3.10)}$$

The relaxation time will be the reciprocal of the collision rate or

$$\tau(E) = \frac{1}{\nu(E)} = \frac{\hbar}{2\pi x(1-x)\ N \left| < V_{AB} > \right|^2 N(E)} \quad \text{(A3.11)}$$

The perturbing potential V_{AB} will not be very large due to the A and B atoms having the same valency. The matrix element $< V_{AB} >$ between initial and final states may be taken as independent of energy for the ranges of energy which are encountered in a band extremum. Then the energy dependence of τ results totally from the term $1/N(E)$ which varies as $E^{-1/2}$ for a parabolic band. Thus the analysis shows that for disorder scattering in alloys τ, the relaxation time, varies as $E^{-1/2}$.

This discussion has presented the only available model for

alloy scattering. Its prime justification for use is that there is no other available or proposed treatment of the problem.

REFERENCES

1. L. Nordheim, Ann. Phys., 9, 607 (1931).

2. F. Bassani and D. Brust, Phys. Rev., 131, 1524 (1963).

3. R. Parmenter, Phys. Rev., 97, 587 (1955).

4. R. Parmenter, Phys. Rev., 99, 1759 (1955).

5. R. Parmenter, Phys. Rev., 104, 22 (1956).

6. J. Ziman, "Electrons and Phonons", p. 246, Oxford Univ. Press, Oxford (1960).

7. J. Ziman, Ibid., p. 128.